Computer modelling and simulation of radiofrequency ablation of bone tumors

Rivas Loya, Ricardo

IMPORTANT NOTE: You are advised to consult the publisher's version (publisher's PDF) if you wish to cite from it. Please check the document version below.

Document Version
Publisher's PDF, also known as Version of record

Publication date:
2022

Computer modelling and simulation
of radiofrequency ablation of bone tumors

Ricardo Rivas Loya

university of groningen

Computer modelling and simulation of radiofrequency ablation of bone tumors

PhD thesis

to obtain the degree of PhD at the
University of Groningen
on the authority of the
Rector Magnificus Prof. C. Wijmenga
and in accordance with
the decision by the College of Deans.

This thesis will be defended in public on

Monday 29 August 2022 at 9.00 hours

by

Ricardo Rivas Loya

born on 26 June 1991
in Chihuahua, Mexico

Supervisors
 Dr. P.M.A. van Ooijen
 Prof. P.C. Jutte
 Dr. T.C. Kwee

Assessment Committee
 Prof. J.N. Doornberg
 Prof. S. Misra
 Prof. M. Maas

Contents

Chapter 1
General Introduction

Radiofrequency ablation (RFA) is a minimally invasive technique for the treatment of solid tumors that can be used for both curative and palliative treatment. Although surgical resection remains the standard of care for most solid tumors, it could lead to higher morbidity and mortality, particularly in patients that have coexistent comorbidities [1]. Thus, local treatment alternatives like RFA, which maximize effectiveness and minimize morbidity, have come forth as an alternative for patients who are not surgical candidates and also as an adjunct to surgery [1]. It has been clinically accepted for the treatment of many tumor types and tissues including primary and secondary malignancies of the liver, kidney, lung, and bone [2].

RFA, temperature, and time

The principle by which RFA destroys tumor tissue is by increasing temperature until irreversible damage occurs [2]. To generate heat, RFA uses a current in the radiofrequency range (460-480 kHz), which by alternating its polarity causes the ions within the target tissue to agitate and generate frictional heat [1]. There is a direct link between the temperature and time needed to destroy cells through thermal damage. At temperatures up to 41 °C, little long-term damage is caused to the target cells, even if maintained for hours [3]. At 46 °C irreversible cell damage begins to occur, and exposures of up to 10 mins will cause necrosis of a significant population of cells [3]. Between 46-52 °C, microvascular thrombosis, ischemia, and hypoxia occur, and the time to kill the target cells is reduced drastically [3]. At temperatures of 60 °C, the cell membrane is destroyed almost instantly, and irreversible damage occurs [3]. At temperatures between 40-48 °C, hyperthermia treatments usually sustain the temperature at the target site for > 1 hrs. to sensitize the tissues to other modalities such as chemotherapy, whereas treatments with temperatures between 60-90 °C are considered as thermal ablation [4]. If tissues are exposed to temperatures above 100°C, water starts to evaporate from the tissues, affecting the energy deposition of RFA because of the sudden increase in the tissue's impedance caused by desiccation, and thus temperatures higher than 100 °C should be avoided for RFA. Furthermore, the heat distribution is not uniform during RFA, with temperatures near the electrodes being highest and decreasing as a function of the distance from the electrode. Additionally, a margin of between 0.5-1 cm of ablated healthy tissue is necessary to eliminate the risk of residual tumor [5]. Because of all these reasons, it is important to have an adequate control of the temperature and duration of the procedure to guarantee the right amount of damage to completely destroy the target tumor.
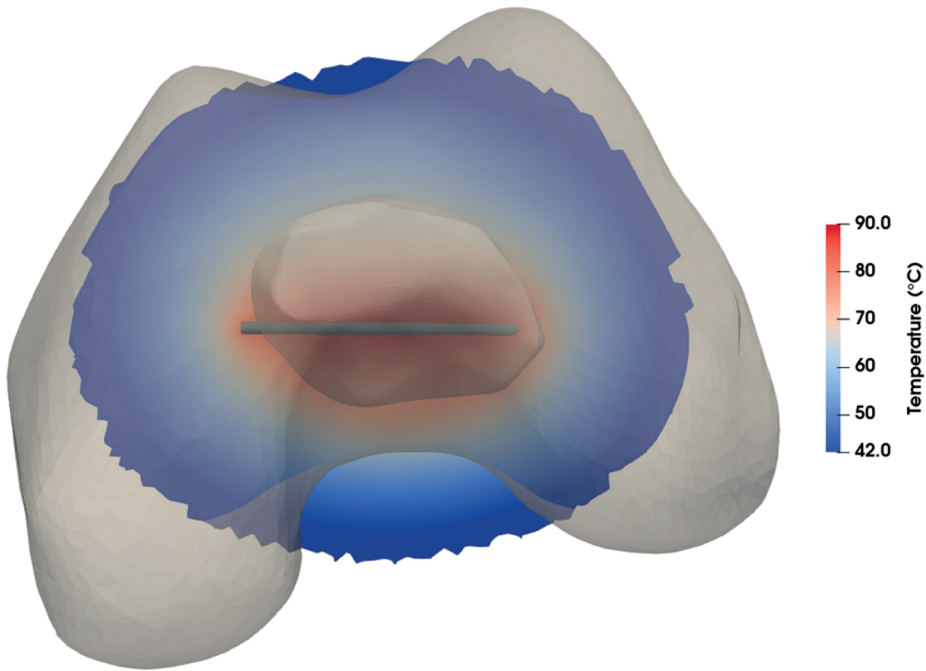
Figure 1 Example of a computer simulation showing the temperature distribution during RFA of a bone tumor in the range of therapeutic hyperthermic temperatures. The electrode can be seen inserted in a bone tumor in the distal femur.

There are various types of RFA devices and modes of energy deposition depending on how the current is regulated and the shape of the electrode. The most common electrode shape are the monopolar needle-like electrodes, with a single active electrode at the end of the probe. These are characterized by their ease of insertion, particularly for solid tumors, and a smaller and more cylindrically shaped ablation zone compared to the multiprobe electrodes [6]. Multiprobe expandable electrodes, with their umbrella-like shape and multiple active electrodes, are used mostly for large soft tissue ablations and produce a spherical ablation zone [6]. There are also internally cooled electrodes, in which a saline solution circulates inside the electrode to prevent overheating of the nearest tissues; and bipolar electrodes, in which two active electrodes are placed close to each other to achieve continuous coagulation between them [6].

For the regulation of energy, some devices use a constant amount of power, but nowadays most devices control the amount of power delivered as a function of the temperature at the tip of the electrode or as a function of the tissue's impedance [6]. For the temperature control, a thermocouple is placed at the tip of the electrode, and depending on the maximum temperature desired (for example, 90 °C), the device would increase or decrease the power output as necessary to reach and maintain this temperature for a certain amount of time defined by the interventionalist [6]. Impedance-controlled ablations deliver energy until a rapid

increase on the impedance occurs, which happens when there is tissue desiccation, and an ablation is deemed successful if the device impedes out [6]. For this thesis, the focus will be on temperature-controlled RFA, which is the modality used at the University Medical Center Groningen for the treatment of the bone tumors discussed further into the thesis, and because it is most commonly used for the treatment of osteoid osteomas (OO) [7].

RFA for the treatment of bone tumors

Because of the many advantages that RFA offers in contrast to some of the most common techniques to treat bone tumors, such as surgical resection, there has been a growing interest for its use in the treatment of bone tumors, particularly for the treatment of a small benign tumor called OO, for which RFA is nowadays suggested as the treatment of choice [7]. Findings suggest it may also be possible to use RFA to treat other (larger) bone tumors such as atypical cartilaginous tumors [8], osteoblastoma [9], and chondroblastoma [10]. Additionally, it has also been suggested for the treatment of recurrent bone and soft-tissue sarcomas in non-surgical candidates [11] and can be used for the treatment of bone metastases such as the ones from hepatocellular carcinoma [12]. However, although RFA is becoming more popular for the treatment of bone tumors, there is little information regarding the resulting size of the ablation zones in bone, and it is not clear if assumptions made for the treatment of other types of tumors in other locations (such as liver) are transferable to the treatment of bone tumors (especially larger ones) with RFA. Therefore, more studies are needed to understand RFA better to guarantee safe and effective ablation zones.

In a study by Lee et al. [13] of RFA in dog femurs, it was demonstrated that MRI was able to accurately determine the extent of the ablation zone by comparing the imaging and histological results. However, although it is possible to determine the extent of the ablation zone by MRI, other studies in RFA of bone have not had a quantitative follow up regarding the size of the ablation zone, focusing instead on whether the tumor was destroyed, recurrence rates, and/ or functional outcomes. Although RFA seems promising for the treatment of bone tumors, the protocols have not been standardized yet, and therefore it is not clear what the optimal configuration may be to guarantee optimal tumor treatment.

Even in the case of OO, for which RFA is the standard treatment of choice, a literature survey reveals that interventionalists use different protocols, even for similar types of lesions, with variations in target temperature or the duration of the ablation. A temperature-controlled mode of 90°C for 6 minutes, as suggested by Rosenthal et al., is the current standard for treating OO with RFA. [7]. However, ablation times of between 6-15 minutes have been reported in multiple studies [14] [15] [16] [17] [18] [19] [20] [21]. Variation can also be observed in the

temperature used, ranging from 60-90°C [17] [18] [19] [22] [23]. Generally, shorter ablation times and/or lower control temperatures are used when a smaller ablation zone is desired, and longer ablation times and/or higher control temperatures are used when a larger ablation zone is needed. However, none of the studies did a quantitative analysis of the extension of the ablation zones, and thus the magnitude of these changes is not clear. For example, does an RFA with a control temperature of 80°C for 6 minutes result in a smaller or larger ablation zone than an RFA with a control temperature of 90°C for 4 minutes? Interventionalists often have to consider these options in an attempt to deliver the best treatment for each individual case, but the answers are not obvious.

Because the Nidus of an OO can be easily identified on a CT scan, and the OO are located in bones, CT guidance has been the standard since the first studies on RFA of OO by Rosenthal et al. [24]. It also allows to clearly visualize the position of the electrode inside the patient and to place it in the nidus with good accuracy [25]. For this, a small hole is performed with a drill in the skin and bone of the patient and then the electrode is manually introduced. The electrode is then slowly introduced in an iterative process in which a CT scan is made every time the electrode is repositioned until the desired position is reached. In the case of ACTs, CT guidance has also been the preferred method, but given the low density of ACTs, the tumor boundaries are not always clearly visible, which could affect the accuracy of the electrode's position.

In this thesis the main focus will be on the use of RFA for the treatment of ACTs and to lesser extent on OO.

ACT, also known as chondrosarcoma grade I [26], is a cartilage-forming bone tumor affecting mostly the long bones and pelvis that permeates marrow spaces replacing marrow fat and bone trabeculae [27]. Because the tumor may evolve to a higher, more aggressive and dangerous, grade, complete tumor removal with intralesional curettage followed by local adjuvant treatment has been considered the standard treatment of choice [28]. However, these and other similar surgical approaches present potential risk of morbidity and complications, such as postoperative fractures, infections, and local recurrence [29] [30]. Given the mild nature of ACT, the possible problems from the current standard of care may outweigh the benefits, and thus minimally invasive techniques like RFA may be a better alternative.

The interest in treating ACT with RFA arose when a supposedly benign lesion of otherwise unclear nature was treated by RFA, which turned out to be an ACT on subsequent pathological examination [31]. The treatment was successful, and given the many advantages of minimally invasive surgery, RFA could be a great alternative for the treatment of ACTs, but still research is needed to guarantee safe and effective planning.

OO are one of the most common types of bone tumors [7], that while benign, they may cause substantial morbidity, particularly due to the remarkable pain they can cause [24]. These lesions are round or oval, and measure up to 1.5 cm in diameter [24]. Lesions occurring within joints or in trabecular bone may produce little or no sclerotic response, whereas the ones occurring in cortical bone are usually surrounded by a dense sclerotic layer [24]. The standard treatment used to be surgical excision, but RFA is now the standard of care [32] for its treatment thanks to its minimal invasiveness in contrast to surgery.
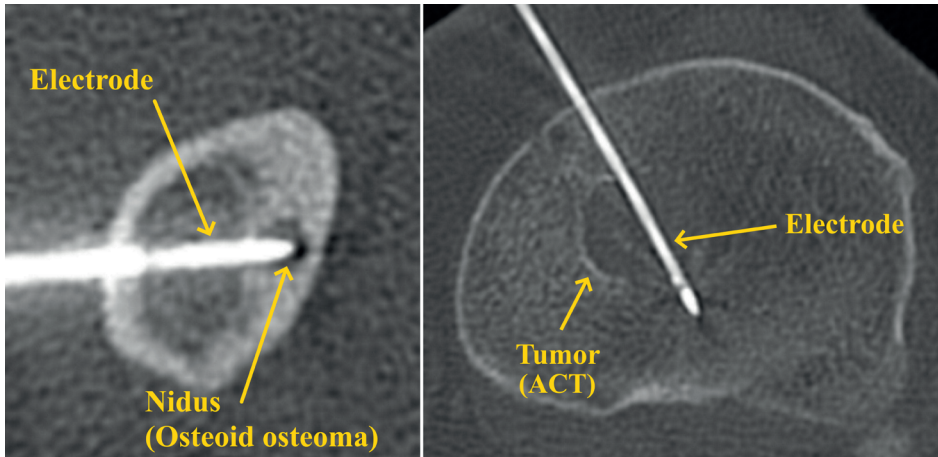
Figure 2 CT Images of two intra-operative images of an RFA procedure. Left, RFA of a small OO. Right, RFA of an ACT. In both cases, the tumors appear as lower density areas (with a darker color) compared to the surrounding bone whereas the electrodes appear as linear high-density structures traversing the tumors.

Computational modelling of RFA and the finite element method

Testing the effect that the procedural parameters may have in the size of the ablation zone in actual patients may be dangerous, either leading to undertreatment, and thus leaving residual tumor, or to overtreatment and causing unnecessary damage to healthy structures. As a solution to this problem, computational simulations have arisen in which models simplify the clinical scenario and the physics underlying the generation and propagation of heat. This allows for a systematic study of the different parameters and configurations of the procedure without having to put the patients at risk of under- or overtreatment. The most popular technique for modelling of RFA has been the Finite Element Method [33], in which the physics that rule ablation, corresponding to a set of partial differential equations, can be solved using numerical methods in a given discretized domain (e.g., an abstraction of the patient's anatomy).

In RFA, heat is generated by the interaction between the applied electric current and the tissues surrounding it in a process called Joule heating, where the electric energy is converted into thermal energy. To calculate the heat source generated by RFA, the tissues can be considered as total resistive because in the radiofrequency range biological tissues have no meaningful capacitive losses [34], and a quasi-static approach can then be considered. With this, the electric field can be calculated using Laplace equation, and the heat source can be calculated as a function of the electric field and the conductivity of each tissue.

Then, the Heat Equation can be used to know how the heat is transported, but for biological tissues the Heat Equation has been modified to account for phenomena such as heat loss due to blood perfusion, resulting in Penne's Bioheat Equation [35].

The heat transfer equation takes into account the density, (), specific heat, (), and thermal conductivity, (), as well as the Temperature (K), time (s), the heat generated by RFA, (), and the heat loss due to blood perfusion, (W /).

These partial differential equations have no analytical solution and numerical methods such as the Finite Element Method have to be utilized to approximate a solution. To solve the equations, a domain and boundary conditions have to be properly defined to approximate the solution to the prescribed problem with numerical methods. The geometry of the object(s) of interest, or the domain, has to be discretized into subdomains, called finite elements, resulting in a system of simpler algebraic equations to approximate the solution locally by fitting trial functions into the partial differential equations and minimizing the error between the solution and an associated error function [36]. Thus, the problem is divided into an assembly of subdomains, consisting of a set of equations to the original problem; these equations are then recombined into a global system of equations with known solutions that can be calculated from the initial values from the original problem [36]. These initial values are set by the boundary conditions, where the problem is defined along a certain boundary of the domain. The discretization of the domain is implemented by the generation of a mesh, consisting of multiple nodes and facets which serve to define the finite elements.

An example of applying the FEM for RFA would be to represent the anatomy of the patient in a discretized form with a mesh, where the mesh is divided into subdomains corresponding to the different tissues and the electrode itself. Each of these subdomains is given certain parameters, like their corresponding density or electrical conductivity, as defined by the tissue we are modeling. Then, we define the places where we "know" the exact solution to our equations. For example, we can assume that the value of the tissue's temperature will be the same as the core body temperature (approximately 37 °C) far away from the electrode. We also know that the grounding pad will be located somewhere far away from the electrode at the outer boundaries

of the domain, defining the value of the electric potential = 0 in that region. Similarly, for the electrode, the voltage will be controlled by the algorithm of our implementation and it will be a known value. With these assumptions, initial values can be given to the model, and the equations can then be approximated and RFA simulated.

It is also important to note that the size of the mesh elements is of great importance, as they define the spatial resolution, and places with high gradients could be subject to high interpolation errors if the elements are too large. In the other hand, places with low gradients do not require high resolution, and using larger elements is encouraged to reduce the computational load. Since the problems do not have an exact solution, it is important to analyze the problem and by trial-and-error guarantee that the solution to the problem does not depend on the discretization of the domains. Usually, a mesh convergence analysis is required, where the elements are reduced in size until the results of a certain metric (like the temperature at certain point of interest) does not change in a significant manner. I Since the equations have no analytical solution, the results totally depend on how the models are defined, where not only the boundary conditions matter, but also the discretization of the mesh.
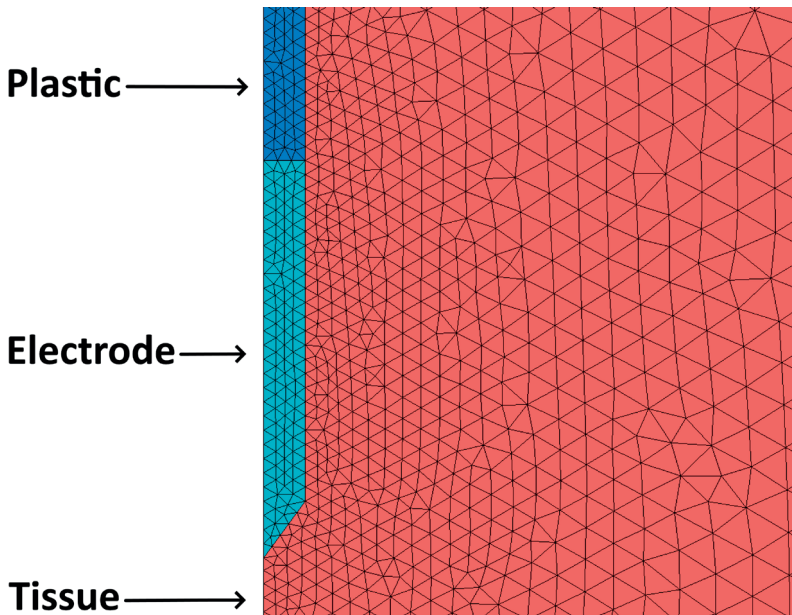
Figure 3 Example of a simplified problem with a 2D mesh with triangular elements representing an electrode inside some tissue. Smaller triangles are used in the electrode, where the heat is generated and the highest gradients are therefore expected, and smaller triangles will help to approximate the solution better because of the higher resolution obtained. At the boundary at the right, larger triangles are used as lower gradients are expected, and larger elements can therefore approximate the solution adequately.

Objectives of this thesis

The optimal configuration of RFA settings for the treatment of bone tumors still remains a mystery, but they are crucially important to guarantee total tumor destruction while sparing as much healthy tissue as possible. With tools such as the Finite Element Method and computer models allowing us to explore the effects of changing the main parameters defining the size of the ablation zone (such as time and temperature) without risking a patient's health: the focus of this thesis will be to explore the effects of the multiple parameters affecting the size of an ablation zone and to try to create computer models able to replicate what is seen in clinical practice in order to create reliable models to predict and plan RFA of bone tumors, which is required for safe and effective tumor ablations.

In Chapter 2, a retrospective study on RFA of ACTs in the long bones was done to try to determine the size of the resulting ablation zones using clinical data. The study showed that RFA of ACT was effective, with the resulting ablation zones being larger than the tumors, and also showed that the ablation zones were much larger than expected, especially when compared to ablations on other common sites such as the liver. The results from this study also served as the first step towards developing the computational models by serving as the clinical standard in which to base the computational models.

Chapter 4 is a study in which the optimal values of some parameters of the computational models were calculated to replicate the clinical cases observed in Chapter 2. The parameters studied were the tissue properties of the main tissues affecting the resulting ablation zone, which are the properties of the ACT and the surrounding trabecular bone. The main factors affecting the ablation zone were studied and an optimal configuration was defined in which it was possible to replicate the clinical cases studied.

In Chapter 5 we used the clinical data from Chapter 2 and the resulting optimized values of Chapter 4 to create complex 3D patient-specific models to calculate the resulting ablation zones. The model was developed with retrospective data, but it could be used for prospective planning, allowing interventionalist to tweak multiple parameters such as the control temperature, time, and position of the electrode in order to guarantee optimal treatment of patients.

In Chapter 3, the thesis will explore using computer models what the quantitative effects to changes in the target temperature and duration of the ablation procedure are on the size of the resulting ablation zone of RFA of OO. Given the multiple possible configurations of target temperature and ablation time, this chapter will shed light on the interplay between these two parameters and how they affect the ablation zone.

In the final chapter, the main conclusions and implications of this thesis are discussed, putting in context our findings and perspectives for the future.

References

[1]   D. Shah, S. Green, A. Elliot, J. McGahan and V. Khatri, "Current oncologic applications of radiofrequency ablation therapies," World J Gastrointest Oncol, vol. 5, no. 4, pp. 71-80, 2013.

[2]   M. Ahmed, C. Brace, F. Lee and S. Goldberg, "Principles of and Advances in Percutaneous Ablation," Radiology, vol. 258, no. 2, pp. 351-369, 2011.

[3]   C. Brace, "Thermal tumor ablation in clinical use," IEEE Pulse, vol. 2, no. 5, pp. 28-38, 2011.

[4]   P. Wust, B. Hildebrandt, G. Sreenivasa, B. Rau, J. Gellermann, H. Riess, R. Felix and P. Schlag, "Hyperthermia in combined treatment of cancer," Lancet Oncol., vol. 3, no. 8, pp. 487-497, 2002.

[5]   S. Goldberg, G. Gazelle and P. Mueller, "Thermal ablation therapy for focal malignancy: a unified approach to underlying principles, techniques, and diagnostic imaging guidance," Am. J. Radiol, vol. 174, pp. 323-331, 2000.

[6]   R. Lencioni, D. Cioni, J. Lera, E. Rocchi, C. Della Piña and L. Croocetti, "Radiofrequency Ablation: Principles and Techniques," in Focal Liver Lesions, Berlin, Heidelberg., Springer, 2005, pp. 307-315.

[7]   D. Motamedi, T. J. Learch, D. N. Ishimitsu, Motamedi¸Kambiz, M. D. Katz, E. W. Brien and L. Menendez, "Thermal Ablation of Osteoid Osteoma: Overview and Stepby-Step Guide," RadioGraphics , vol. 29, no. 7, pp. 2127-2141, 2009.

[8]   E. F. Dierselhuis, P. J. M. van den Eerden, H. J. Hoekstra, S. K. Bulstra, A. J. H. Suurmeijer and P. C. Jutte, "Radiofrequency ablation in the treatment of cartilaginous lesions in the long bones: results of a pilot study," The Bone & Joint Journal, Vols. 96-B, no. 11, pp. 1540-1545, 2014.

[9]   C. Rehnitz, S. D. Sprengel, B. Lehner, K. Ludwig, G. Omlor, C. Merle, H.-U. Kauczor, V. Ewerbeck and M.-A. Weber, "CT-guided radiofrequency ablation of osteoid osteoma and osteoblastoma: Clinical success and long-term follow up in 77 patients," European Journal of Radiology, vol. 81, no. 11, pp. 3426-3434, 2012.

[10]   C. Xie, L. Jeys and S. L. James, "Radiofrequency ablation of chondroblastoma: long-term clinical and imaging outcomes," European Radiology , vol. 25, no. 4, pp. 1127-1134, 2015.

[11]   K. Yamakado, A. Matsumine, T. Nakamura, A. Nakatsuka, H. Takaki, T. Matsubara, K. Asanuma, A. Sudo, Y. Sugimura and H. Sakuma, "Radiofrequency ablation for the treatment of recurrent bone and soft-tissue sarcomas in non-surgical candidates," International Journal of Clinical Oncology, vol. 19, no. 5, pp. 955-962, 2014.

[12]   "Radiofrequency Ablation for the Treatment of Bone Metastases From Hepatocellular Carcinoma," AJR Am J Roentgenol, vol. 194, no. 2, pp. 536-541, 2010.

[13]   J. Lee, S. Choi, H. Park, M. Lee, C. Han, J. Choi, J. Choi, S. Hong, J. Han and B. Choi, "Radiofrequency thermal ablation in canine femur: evaluation of coagulation necrosis reproducibility and MRI-histopathologic correlation," AJR Am J Roentgenol, vol. 185, no. 3, pp. 661-7, 2005.

[14]   M. Weber, S. Sprengel, G. W. Omlor, B. Lehner, B. Wiedenhöfer, H. Kauczor and C. Rehnitz, "Clinical long-term outcome, technical success, and cost analysis of radiofrequency ablation for the treatment of osteoblastomas and spinal osteoid osteomas in comparison to open surgical resection," Skeletal Radiol, vol. 44, no. 7, pp. 981-993, 2015.

[15]   R. Rehnitz, S. Sprengel, B. Lehner, K. Ludwig, G. Omlor, C. Merle, H. Kauczor, V. Ewerbeck and M. Weber, "CT-guided radiofrequency ablation of osteoid osteoma and osteoblastoma: clinical success and long-term follow up in 77 patients," Eur J Radiol, vol. 81, no. 11, pp. 3426-34, 2012.

[16]   D. Rosenthal, F. Hornicek, M. Torriani, M. Gebhardt and H. Mankin, "Osteoid osteoma: percutaneous treatment with radiofrequency energy," Radiology, vol. 229, no. 1, pp. 171-175, 2003.

[17]   R. Hoffmann, T. Jakobs, C. Kubisch, C. Trumm, C. Weber, H. Duerr, T. Helmberger and M. Reiser, "Radiofrequency ablation in the treatment of osteoid osteoma-5-year experience," Eur J Radiol, vol. 73, no. 2, pp. 374-379, 2010.

[18]   K. Sung, J. Seo, J. Shim and Y. Lee, "Computed-tomography-guided percutaneous radiofrequency thermoablation for the treatment of osteoid osteoma-2 to 5 years follow-up," int Orthop, vol. 33, no. 1, pp. 215-1218, 2009.

[19]   S. Mylona, S. Patsoura, P. Galani, G. Karapostolakis, A. Pomoni and L. Thanos, "Osteoid osteomas in common and in technically challenging locations treated with computed tomography-guided percutaneous radiofrequency ablation," Skeletal Radiol., vol. 39, no. 5, pp. 443-449, 2010.

[20]   A. Paladini, P. Lucatelli, F. Cappelli, G. Pizzi, V. Anelli, E. Amodeo, D. Beomonte Zobel, L. Paladini, R. Biagini, D. Attala, C. Zoccali and G. Vallati, "Osteoid osteoma treated with radiofrequency ablation in non-operating room anesthesia. A different way of approaching ablative therapy on osteoid osteoma," Eur Rev Med Pharmacol Sci, vol. 22, no. 17, pp. 5438-5446, 2018.

[21]   E. Rimondi, A. Mavrogenis, G. Rossi, R. Ciminari, C. Malaguti, C. Tranfaglia, D. Vanel and P. Ruggieri, "Radiofrequency ablation for non-spinal osteoid osteomas in 557 patients," Eur Radiol, vol. 22, pp. 171-188, 2012.

[22]   U. Albisinni, A. Bazzocchi, G. Bettelli, G. Facchini, E. Castiello, M. Cavaciocchi, G. Battista and R. Rotini, "Treatment of osteoid osteoma of the elbow by radiofrequency thermal ablation," J Shoulder Elbow Surg., vol. 23, no. 1, pp. e1-7, 2014.

[23]   B. Gebauer, F. Collettini, C. Bruger, K. Schaser, I. Melcher, P. Tunn and F. Streitparth, "Radiofrequency Ablation of Osteoid Osteomas: Analgesia and Patient Satisfaction in Long-term Follow-up," Rofo, vol. 185, no. 10, pp. 959-966, 2013.

[24]   D. Rosenthal, A. Alexander, A. Rosenberg and D. Springfield, "Ablation of Osteoid Osteomas with a Percutaneously Place Electrode: A New Procedure," Radiology, vol. 183, no. 1, pp. 29-33, 1992.

[25]   H. Nijland, J. Gerbers, S. Bulstra, J. Overbosch, M. Stevens and P. Jutte, "Evaluation of accuracy and precision of CT-guidance in Radiofrequency Ablation for osteoid osteoma in 86 patients," PLoS ONE, vol. 12, no. 4, 2017.

[26]   L. A. Doyle, "Sarcoma classification: An update based on the 2013 World Health Organization Classification of Tumors of Soft Tissue and Bone," Cancer, vol. 120, no. 12, pp. 1763-1774, 2014.

[27]   R. A. Marco, S. Gitelis, G. T. Brebach and J. H. Healey, "Cartilage tumors: evaluation and treatment," J Am Acad Orthop Surg, vol. 8, no. 5, pp. 292-304, 2000.

[28]   H. Gelderblom, P. C. Hogendoorn, S. D. Dijkstra, C. S. van Rijswijk, A. D. Krol, A. H. Taminiau and J. V. Bovee, "The Clinical Approach Towards Chondrosarcoma," Oncologist, vol. 13, no. 3, pp. 320-329, 2008.

[29]   M. Meftah, P. Schult and R. Henshaw, "Long-term results of intralesional curettage and cryosurgery for treatment of low-grade chondrosarcoma," J Bone Joint Surg Am, vol. 95, no. 15, pp. 1358-1364, 2013.

[30]   I. van der Geest, M. de Valk, J. de Rooy, M. Pruszczynski, R. Veth and H. Schreuder, "Oncological and functional results of cryosurgical therapy of enchondromas and chondrosarcomas grade 1," J Surg Oncol, vol. 98, no. 6, pp. 421-426, 2008.

[31]   E. Dierselhuis, P. Jutte, P. van der Eerden, A. Suurmeijer and S. Bulstra, "Hip fracture after radiofrequency ablation therapy for bone tumors: two case reports," Skeletal Radiol., vol. 39, no. 11, pp. 1139-1143, 2010.

[32]   . R. S. Fernando, C. G. María del Mar, M. M. Jose Luis , R. G. Manuel and T. F. Juan Miguel , "Treatment of bone tumours by radiofrequency thermal ablation," Curr Rev Musculoskelet Med, vol. 2, no. 1, pp. 43-50, 2009.

[33]   E. J. Berjano, "Theoretical modeling for radiofrequency ablation: state-of-the-art and challenges for the future," Biomed Eng Online, vol. 5, no. 24, 2006.

[34]   J. Doss, "Claculations of electric fields in conductive media," Med phys, vol. 9, no. 4, pp. 566-73, 1982.

[35]   H. Pennes, "Analysis of tissue and arterial blood temperatures in the resting human forearm," Applied physiology, vol. 1, no. 2, pp. 93-122, 1948.

[36]   "About FEM," University of Birmingham, [Online]. Available: https://intranet.birmingham.ac.uk/collaboration/hpc-research/abaqus-sig/about/index.aspx. [Accessed 9 August 2021].

[37]   T. A. Damron, W. G. Ward and A. Stewart, "Osteosarcoma, chondrosarcoma, and Ewing's sarcoma: National cancer data base report," Clin Orthop Relat Res, no. 459, pp. 40-47, 2007.

[38]   J. Ferguson and S. Turner, "Bone Cancer: Diagnosis and Treatment Principles," Am Fam Physician, vol. 98, no. 4, pp. 205-213, 2018.

Chapter 2

Radiofrequency ablation of atypical cartilaginous tumors in long bones: a retrospective study

Ricardo Rivas[a*], Jelle Overbosch[b], Thomas Kwee[b], Joep Kraeima[c], Rudi A. J. O. Dierckx[d], Paul C. Jutte[e], Peter M. van Ooijen[a]

[a] University of Groningen, University Medical Center Groningen, Department of Radiotherapy, Groningen, The Netherlands
[b] University of Groningen, University Medical Center Groningen, Department of Radiology, Groningen, The Netherlands
[c] University of Groningen, University Medical Center Groningen, Department of Oral and Maxillofacial Surgery, Groningen, The Netherlands
[d] University of Groningen, University Medical Center Groningen, Department of Nuclear Medicine and Molecular Imaging, Groningen, The Netherlands
[e] University of Groningen, University Medical Center Groningen, Department of Orthopedics, Groningen, The Netherlands

Radiofrequency ablation of atypical cartilaginous tumors in long bones: a retrospective study

Purpose: To determine the size of the ablation zone after radiofrequency ablation (RFA) of atypical cartilaginous bone tumors (ACT) using temperature-controlled 20 and 30 mm RFA straight non-cooled electrodes.

Materials and methods: Sixteen patients with ACT in their long bones, who had undergone a single-session single-application CT-guided temperature-controlled RFA, were included retrospectively in the study. Tumors with a diameter of 10-25 mm were treated with 20 mm electrodes (n=10), and tumors of 25-35 mm, with 30 mm electrodes (n=6). The ablated zone was measured after three months on MRI images.

Results: All the tumors were within the ablated zone on the 3-month follow-up MRI scan. The mean ablation time with the electrode, at a target temperature of 90°C, was 7.6 minutes (range 6-10). The median of the largest ablation diameters, on applying the 20 and 30 mm electrodes, were 42 mm (IQR 8.5, range 30-51 mm) and 44.5 mm (IQR 4.5, range 42-63 mm), respectively.

Conclusions: All the retrospectively viewed tumors in the long bones of ACT patients treated with RFA were completely ablated. The ablation zone diameters in the bones were larger than expected, when compared to other tissues, such as the liver.

Introduction

Atypical cartilaginous tumors (ACT), previously known as chondrosarcoma grade one [1], are one of the most frequently encountered tumors in orthopedic oncology [2]. These are characterized by the development of cartilaginous neoplastic tissue, mostly in the long bones and pelvis, that permeates marrow spaces and completely replaces the marrow fat and bone trabeculae [3]. Due to its unpredictable nature, and the possibility of local tumor progression, treatment encompasses complete tumor removal with intralesional curettage followed by local adjuvant treatment as the standard technique of choice [4]. However, the latter technique can lead to complications, such as postoperative fractures, infections and local recurrence [5,6].

Radiofrequency Ablation (RFA) is a minimally invasive procedure that has become the treatment of choice for osteoid osteomas (OO), and is also suitable for the treatment of other bone tumors [7]. Contrary to intralesional curettage, RFA is particularly appealing due to its high success and low complication rates [8-9], and because of the need of little to no patient hospitalization, making it a good option to explore as an alternative to the standard surgical care. Although rare, some known complications of RFA on bone tumors include the potential damage to adjacent soft tissue, particularly in the presence of cortical thinning [10], and the risk of fractures [11].

A pilot study by our research group already proved that cartilaginous tumor cells can, potentially, be eliminated with RFA [12]. It also demonstrated that gadolinium-enhanced magnetic resonance (MR) imaging three months post procedure could be a reliable post-operative follow-up monitoring technique for the detection of residual tumors, similar to the findings by Lee et al. for OO [13]. Although the safety of RFA has been attested, accurate and reproducible planning remains challenging because of the lack of available information on the size of RFA ablation zones in bone tumors and on whether it is comparable to RFA zones in soft tissues (e.g., liver).

Consequently, intervention radiologists and oncology surgeons have had to rely on their experience in the treatment of other types of tumors and on procedural recommendations supplied by the RFA manufacturers. The clinical experience is often based on the treatment of small (< 2 cm) tumors such as OO or on the ablation of other tissues such as the liver, whereas the manufacturers' information is often based on ex-vivo ablations of non-perfused healthy animal livers treated at room temperature. No standard has been set yet, as it is known that differences in tissue composition and in procedure time result in significantly different outcomes [14]. Additionally, some of the few studies of RFA on larger bone tumors, such as osteoblastomas [15-17] and chondroblastomas [18-21], have only focused on clinical outcomes, and not on

the measurements of the ablation zones. Thus, the combination of the aforementioned factors makes it difficult to plan and predict the size of a RFA zone for the treatment of bone tumors.

Therefore, the aim of this study was to evaluate and report on the MRI and CT findings after carrying out a RFA on ACT in patients who were evaluated as possible candidates for RFA instead of intralesional curettage, to report the diameters of the tumors and the corresponding resulting diameters of their ablation zones, and to test whether or not RFA can produce large enough ablation zones to completely ablate the target tumor.

Materials and Methods

Study design

Patients aged ≥18 with indicative signs of ACT, who had opted for surgical treatment (in contrast to watchful waiting), were selected based on a multidisciplinary assessment consisting of location, size, and aspects of the tumor on an MRI. At the time of the evaluation, the options were discussed with the patient: curettage with local adjuvants or RFA. This retrospective study is based on the patients who chose to be treated with RFA.

To study the size of the resulting ablation zones, we examined intra-operative Computed Tomography (CT) as well as pre and post-operative gadolinium-enhanced MR images of patients who underwent RFA to treat ACT from January 2015 to December 2017 at the University Medical Center Groningen (UMCG). Biopsies were taken at the time of the procedure prior to the RF ablation to confirm the characteristic imaging diagnosis of ACT. Only patients whose diagnosis of ACT had been histopathologically confirmed were selected for this retrospective study. Furthermore, only patients treated with a single-session single-application ablation were selected for this retrospective study in order to reduce the variability in ablation zone size produced by the needle placement in the cases requiring multiple overlapping ablations on the same tumor .

The patients were informed about the potential use of their anonymized data for scientific research with a written form at the time of the intervention; any patients who objected to sharing their data were excluded from the study. Since the procedure was part of the usual care, no additional written or verbal consent was necessary, which is in accordance with the regulations of the Medical Ethical Review Board of the University Medical Center Groningen.

The tumors were measured on a pre-operative gadolinium-enhanced MRI scan. The following electrode lengths were used for the ablation: tumor diameters in the 10-25 mm range were treated with a 20 mm exposed tip electrode, while tumors in the 25-35 mm range were treated

using a 30 mm exposed tip electrode. Tumors > 35 mm were ablated with multiple overlapping ablations and were not included in this study. This decision was made based on our previous experience with total bone tumor ablations . However, the overall size of the tumor and its location also played an important role when choosing the electrode length and whether overlapping ablations were needed.

RFA procedure

All the RFA procedures were day-care treatments and were performed under CT guidance (Somatom Definition AS, Siemens Medical Systems, Erlangen, Germany) and general or spinal anesthesia by two experienced radiologists.

An 11G bone needle was used to drill a hole in the bone, both for tissue sampling and to position the RFA electrode (17G, Covidien CoolTip, Medtronic, USA). The procedure was temperature-controlled, non-cooled, with a target temperature of 90° Celsius at the tip of the electrode, and an ablation time of between 6 and 10 minutes. The time was estimated based on our prior experience of treating ACT and other bone tumors, particularly OO. Generally, if the temperature rose without a problem to 90° Celsius, the ablation time was 6 minutes; if there were problems reaching the target temperature (e.g., electrical impedance increasing fast and the system shutting off before reaching it) the electrode was repositioned slightly and the temperature was increased gradually by hand to reach 90° Celsius, which required up to 10 mins of ablation. Additionally, in order to estimate the effects of time and temperature on the size of the ablation zones, we measured the duration of the ablation with the electrode at a temperature of ≥ 60° and the duration after it reached the target temperature of 90°.

Given the small size of the lesions, surgical stabilization was not necessary for these cases.

Evaluation RFA

A follow up MRI was performed 3 months after the procedure to assess the ablation zone using a 1.5 T MRI scanner (Siemens, Erlangen, Germany) with a surface coil. Both fat-suppressed Short Tau Inversion Recovery (STIR) T2-weighted sequences (TR/TE/TI: 8270/160/19 ms, slice thickness 4 mm) and T1-weighted images (TR/TE: 500/19 ms, slice thickness 4 mm), before and after the administration of an intravenous gadolinium-based contrast agent (0.1 mmol gadoterate meglumine (Dotarem®; Guerbet) per kg of body weight), were acquired in two planes (transversal and either coronal or sagittal) as part of the routine MRI protocol in the UMCG.

MRI analysis and measurements

The tumors were measured on the pre-operative MR images following the previously described directions. After ablation, the resulting ablation zones were measured on the follow-up

gadolinium-enhanced T1-weighted MR images. The assessor was unaware of the size of the RFA needle used. Two diameters were defined and measured, one along the line of the electrode and one perpendicular to it. The diameter perpendicular to the electrode was assessed in both perpendicular planes and the shortest of the two was chosen. Pre- and postoperative MR images were used in order to compare the tumor and ablation diameters.

Based on the manufacturer's information, the length of the electrode is one of the main factors defining the extent of the ablations. Longer electrodes produce a larger ablation zone, with a longer ablation diameter along the electrode and a shorter ablation diameter perpendicular to it. Therefore, the resulting ablation diameters were classified and analyzed according to the electrode length used.

Statistics

A Pearson's correlation coefficient was calculated to test for the effect of the duration of treatment and the differences in ablation range. The means and standard deviations (SD) of the normally distributed data, as well as the medians and interquartile ranges (IQR) of the non-normally distributed data, are also presented. P values <0.05 were considered significant. All statistical analyses were performed using Python with the 2.7 version of SciPy [22].

Results

A total of N=16 patients matched the inclusion criteria namely, those treated with a single electrode position ablation (Figure 1). The mean age of the patients was 48.8 years (±15.3, range 24-72). The treated anatomical locations were: femur (n=12), tibia (n=2), and humerus (n=2) whereby two tumors resided in the diaphysis (one in the femur, one in the humerus) and 14 in the metaphysis. Table 1 presents the entire patients' parameters and outcomes, while Table 2 gives a summary.

Table 1. Patients, parameters, and outcomes.

Patient	Age	Bone	Location	Electrode length (mm)	Time at 90° C (mins)	Time > 60° C (mins)	Tumor, perpendicular diameter	Tumor, longitudinal diameter	Ablation, perpendicular diameter	Ablation, longitudinal diameter
1	24	Femur	Diaphysis	20.00	6	8	18	38	19	42
2	39	Femur	Metaphysis	20.00	10	12	16	18	24	42
3	54	Humerus	Diaphysis	20.00	8	8	12	18	14	33
4	64	Humerus	Metaphysis	30.00	6	12	21	29	32	42
5	26	Femur	Metaphysis	30.00	10	8	19	25	27	43
6	49	Tibia	Metaphysis	20.00	6	8	17	20	43	44
7	48	Femur	Metaphysis	30.00	8	10	23	32	41	63
8	69	Femur	Metaphysis	30.00	6	10	15	26	28	48
9	56	Tibia	Metaphysis	20.00	9	10	14	23	40	43
10	52	Femur	Metaphysis	20.00	9	9	23	25	43	51
11	72	Femur	Metaphysis	30.00	8	10	22	26	37	46
12	44	Femur	Metaphysis	20.00	7	9	10	12	17	33
13	29	Femur	Metaphysis	30.00	6	8	16	23	33	43
14	43	Femur	Metaphysis	20.00	6	8	17	20	39	43
15	41	Femur	Metaphysis	20.00	9	10	13	16	24	30
16	72	Femur	Metaphysis	20.00	7	8	19	25	25	39
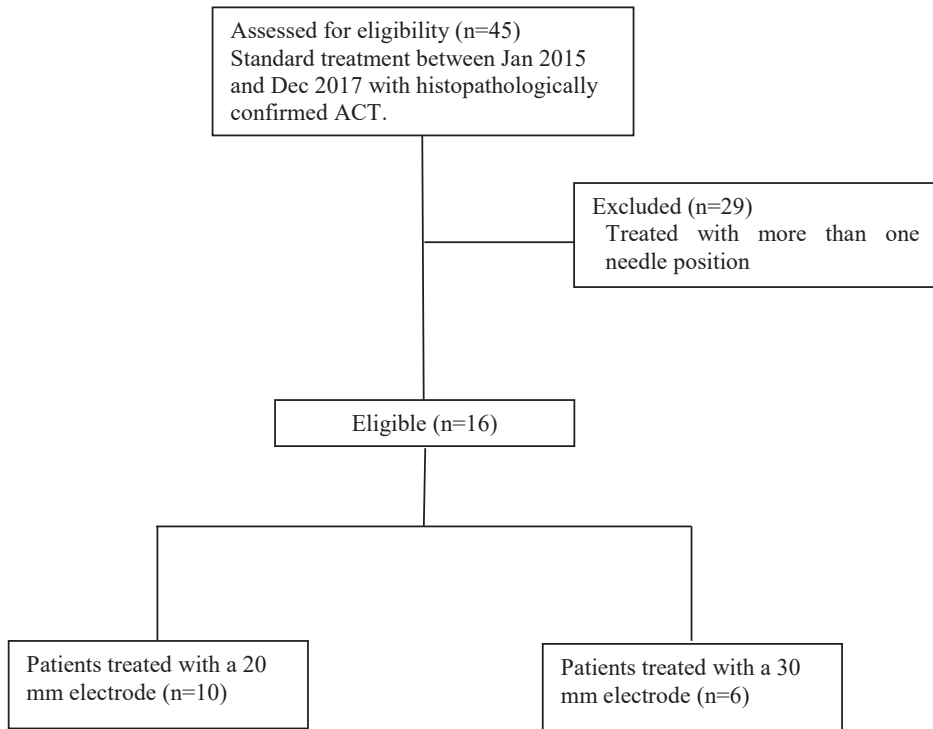
Figure 1. CONSORT diagram showing the inclusion and exclusion criteria and the resulting eligible patients, who were separated into two groups based on the length of the electrode used to treat them.

Table 2. Summary of the patients and ablations parameters.

Patients	16
Age	48.8 (±15.3) years
Bone (femur/tibia/humerus)	12/2/2
Location (diaphysis/metaphysis)	2/14
Patients per needle length (20/30)	10/6
Time > 60°C	9.25(±1.3 , range 8-12) minutes
Time at 90°C	7.56 (±1.5, range 6-10) minutes

The median ablation zone diameters of the 20 mm electrode were 42 (IQR 8.5) and 24.5 (IQR 19.5) mm for the longitudinal and perpendicular axes, respectively. Regarding the 30 mm electrode, the median ablation zone diameters were 44.5 (IQR 4.5) and 32.5 (IQR 7) mm for the longitudinal and perpendicular axes, respectively. The mean and median tumor and ablation zone diameters of all the data grouped according to electrode length, with their respective SD or IQR, for the perpendicular and longitudinal diameters, are summarized in Table 3. Figure 2 gives two examples of the ablation zone measurements.

Chapter 2
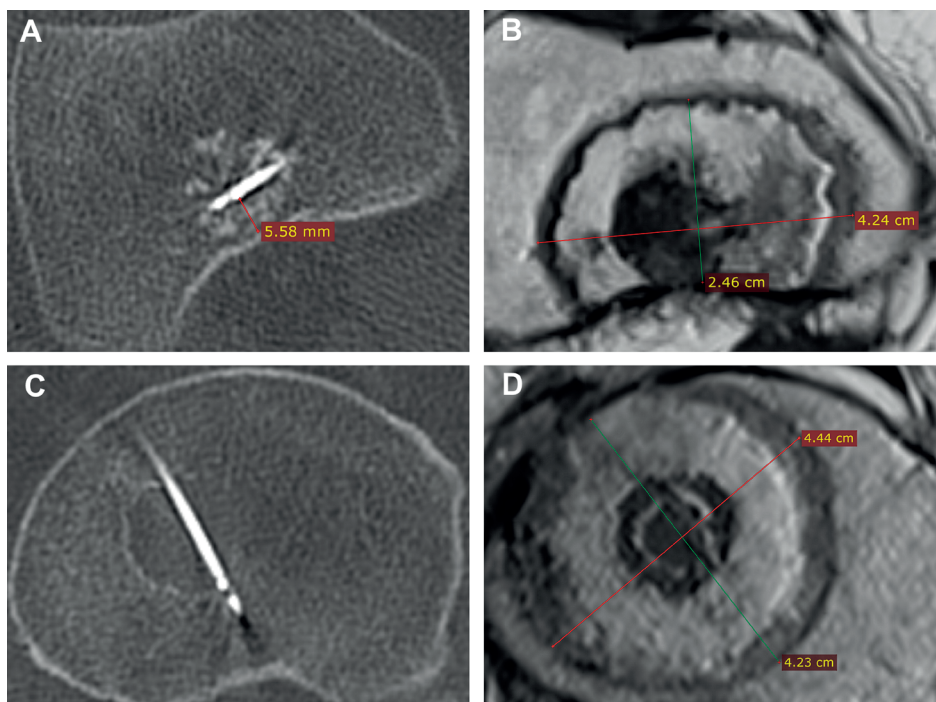
Figure 2. A, B: intraoperative CT and postoperative gadolinium-enhanced MR of a tumor ablated close to the cortical wall in a femur metaphysis. C, D: intraoperative CT and postoperative gadolinium-enhanced MR images of a centrally located tumor ablated in a femur metaphysis.

Table 3. Longitudinal and perpendicular diameters of the tumors and ablations. All measurements are in millimeters. Values with a * are normally distributed and represent thus the mean and standard deviation (SD), whereas the rest are non-normally distributed and represent the median and interquartile ranges (IQR), as indicated.

		All patients (n=16)			20 mm electrode (n=10)			30 mm electrode (n=6)		
		Mean/ median	SD/ IQR	Range	Mean/ median	SD/ IQR	Range	Mean/ median	SD/ IQR	Range
Resulting ablations	**longitudinal axis**	43	5	30-63	42	8.5	30-51	44.5	4.5	42-63
	perpendicular axis	28	15	14-43	24.5	19.5	14-43	32.5	7	27-41
Treated tumors	**longitudinal axis**	23.5*	6.3*	12-38	20	6.5	12-38	26	3	23-32
	perpendicular axis	17.1*	3.8*	10-23	16.5	4.5	10-23	20	5	15-23

The mean ablation time with the tip of the electrode at 90°C was 7.6 ± 1.5 minutes, (range 6-10 minutes) whereas with a temperature of ≥ 60°C it was 9.25 ± 1.3 minutes (range 8-12 minutes). No significant correlations were found between the differences in the ablation diameters and their duration, neither for the time at 90°C nor for the time with a temperature of ≥

60°C. The P-values for the longitudinal and perpendicular ablation diameters against time at 90°C were p = 0.94 and p = 0.96 for the 20 mm electrode, and p = 0.76 and p = 1 for the 30 mm electrode. The p values for the perpendicular and longitudinal ablation diameters against time at ≥ 60°C were: p = 0.94 and p = 0.93 for the 20 mm electrode, and p = 0.82 and p = 0.63 for the 30 mm electrode.

The median, IQR, and the range of the difference in length between the resulting ablation and tumor diameters were as follows: the 20 mm electrode (n=10) had a perpendicular diameter of 9.5 mm (IQR 15.2, range 1-26), and a longitudinal diameter of 20.5 mm (IQR 9.5, range 4-26); the 30 mm electrode (n=6) had a perpendicular diameter of 14 mm (IQR 5, range 8-18), and a longitudinal diameter of 20 mm (IQR 8.5, range 13-31). These results are summarized in Table 4 and illustrated in Figure 3.

Table 4. Median, IQR, and range of the difference between the resulting ablation diameters and tumor diameters. All values are in millimeters.

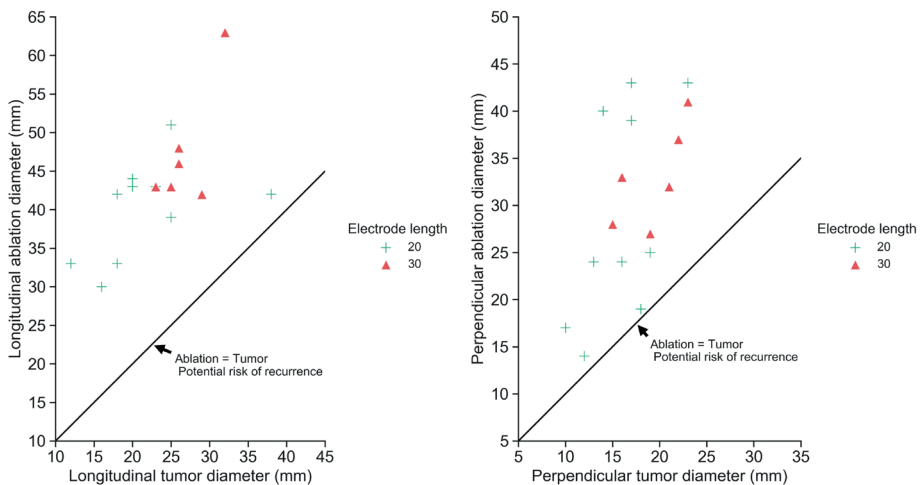|	Ablation diameters minus tumor diameters			
	20 mm electrode (n=10)		30 mm electrode (n=6)	
	Perpendicular	Longitudinal	Perpendicular	Longitudinal
Median	9.5	20.5	14	20
IQR	15.2	9.5	5.0	8.5
Range	1-26	4-26	8-18	13-31

Figure 3. Tumor diameters versus resulting ablation diameters of all 16 patients. Left: longitudinal ablation and tumor diameters. Right: Perpendicular ablation and tumor diameters. The solid diagonal lines in the graphs represent the point where the size of the ablation and the tumor could be the same, indicating the potential risk of recurrence.

All the ablations were technically successful (i.e., the ablated zone was ≥2 mm clear of the tumor on the 3-month follow up MRI, as planned).

Discussion

RFA is an attractive minimally invasive treatment alternative to surgery. The present study addressed an important knowledge gap on the extent of thermal damage by RFA on bone tumors. Applying RFA on ACT in the long bones, using a temperature-controlled algorithm with 20 and 30 mm straight non-cooled electrodes, resulted in ablations with median longitudinal diameters of 42 and 44.5 mm, respectively, which were large enough to completely cover the tumors being treated and more, as planned.

Although literature exists on the resulting ablation zones following RFA in tissues like the liver [23, 24], RFA studies of bone tumors other than OO have mostly focused on the clinical outcomes while giving little insight into the extent of the thermal damage. This information is critical for reliable and accurate planning to ensure safe and effective RF ablation of bone tumors. The tumor should be completely ablated while damaging as little healthy surrounding tissue as possible. Therefore, further studies of the extent of RFA ablation zones in bones should be done to explore the possibilities of using this, apparently less risky, technique for the treatment of bone tumors.

Interestingly, since bone has lower thermal and electrical conductivities than soft tissues, such as the liver [25], one could intuitively expect the resulting ablation zones to be smaller than those in soft tissue. However, this was not found in our study. The high water content of cartilaginous tumors together with the lack of heat sinks could be a plausible explanation for the large ablation zones. We have to consider that the main ablated tissue, the tumor, was cartilage instead of bone, and its high water content might result in more favorable conduction of current and heat. Furthermore, the electrical conductive property of cartilage seems to indicate that it is slightly higher than liver tissue (and much higher than bone), but it has similar thermal properties as the liver [25]. Moreover, bone ablations do not suffer from heat sinks caused by nearby large blood vessels, which hinder the ablations. Some studies suggest that tumor tissue has a higher degree of electrical conductivity than healthy tissue [26-28], which could further explain the large ablation zones obtained, since tissues with higher conductivities demonstrate more energy deposition [29].

Another important remark about our study is that applying RFA to an ACT produced ablations with a much shorter perpendicular axis than longitudinal axis (Table 3). Although it is true that the longitudinal axis is supposed to be longer, the difference is probably less than it

seems according to our numerical results. This discrepancy may be explained by the anatomical characteristics of the tumors and their surroundings, the planning of the procedures, and our aim to report the smallest ablation diameter in the perpendicular axes. Clear examples of this are patients numbers one and three (Table 1), whose ablation diameters were particularly shorter in the perpendicularly measured axis. This may have been because the ablations were confined to the small bone cavities (the diaphysis), where the cortical bone could have prevented the ablations from developing further, and therefore resulted in ablations that were as large as possibly allowed by the bone surrounding them. This effect, in turn, resulted in the reported perpendicular ablation diameters, which were as large as the bone in which they were confined i.e., short, yet effective, ablation diameters.

Similarly, this effect was observed when the tumors were located next to, but not completely surrounded by, cortical bone, as shown in Figures 2 A and B, where an electrode was placed immediately next to the cortical bone. The resulting ablation zone seemed to be limited in the direction towards the cortical wall but not in the other directions. However, since we aimed to report the shortest diameter, we chose the diameter that was limited by the cortex. The apparent insulating properties of cortical bone are in accordance with other studies, such as the one by Pinto et al. [30]. In contrast, the ablations seemed to extend more when they were not limited by the cortex, as in the case of the centrically located tumors in the femur metaphysis, as exemplified in Figures 2 C and D. These two phenomena can be seen in the wide variations in the extent of the perpendicular ablations, as shown in Figure 1, depending on whether they were limited by bone or not.

A limitation of this study is that we could not show the effects of the differences in ablation time on the resulting ablation diameters, as shown by the weak correlation coefficients. This could be because all the ablations were performed in a similar time frame of 6-10 minutes, after having reached the target temperature of 90°C. Since ablations tend to grow rapidly in the first few minutes of the procedure and then reach a plateau, whereupon an increase in time results in small differences, we think that any additional changes after 6 minutes, due to thermal damage, are negligible. This does not mean, however, that this phenomenon occurs after exactly 6 minutes. More data with shorter and longer ablation times are needed to test this, but such experiments also come with the risk of unsuccessful ablations. Additionally, other factors may be affecting the size of the ablations, such as the histological characteristics of each individual tumor, the position of the electrode, etc.

Another limitation was the impossibility of finding a clear relationship between the results of the ablations and the location of the tumors, as there were many possible confounders and few data points per category (e.g., electrode used, bone type, bone location, etc.). This stresses the main limitation of the study, in that it was a single center study with only 16 patients. In

addition, the ranges of the selected electrode lengths were not clear cut because we observed some overlap around the 25 mm zone. This could have been the result of differences in opinion in the assessment of the tumor, other than diameter, and thus as to which electrode to use for the intervention. We also observed one case of a considerably large tumor that was ablated with a 20 mm electrode (patient 1); the reasoning behind the decision to use this electrode is unknown to us. Any repositioning of the antenna was not reported, but it could explain why that electrode was chosen for a tumor of that size.

Likewise, patient 7's ablation diameter was particularly large along the electrode, but we are not sure what caused this. Furthermore, although an MRI made 3 months after the procedure can be used reliably to show the results of a RFA applied to an OO, perhaps this is not the case for an ACT. The resulting ablated zones might have been underestimated because healing may have already occurred and the ablated zones had shrunk.

Finally, even though the results show that applying RFA to an ACT can produce large ablation zones, it is important not to overestimate the effects of a RFA and the procedures should be planned with care, particularly in complicated cases where overlapping ablations may be necessary. Complete tumor removal is, of course, preferable to having residual tumor tissue, and bone seems to be able to protect the surrounding structures from thermal damage, even if the ablations are larger than expected. However, other studies of RFA on chondroblastomas have shown the risk of damaging articular cartilage [8] and the growth plate [18]. Thus, it seems that bone may not be protective in all cases, which could be related to the thickness of the cortical bone or the perfusion of the surrounding tissues. These factors may also be the result of an underestimation of the extent of the ablations, as highlighted in this study. Therefore, extra caution should be taken when performing ablations close to structures at risk such as the cartilage surface of joints or nerve roots. Additionally, it is important to remember that our results were obtained without using the cool-tip mode, which, if used, could potentially result in even larger ablation zones.

The results of our study should help to understand the effects of RFA on bone tumors and highlight the importance of presenting not only the clinical outcomes of these procedures, but also the resulting ablation zones. A better understanding of RFA effects on bone is still needed for accurate and safe planning of the procedures.

Conclusion

Radiofrequency ablation of atypical cartilaginous tumors in bone with a temperature-controlled mode and straight non-cooled electrodes resulted in large enough ablations to treat the target tumors. The ablations here were larger than those seen in soft tissue.

Acknowledgements

Disclosure statement

The authors report no conflicts of interest.

References

1. Doyle L. Sarcoma classification: An update based on the 2013 World Health Organization Classification of Tumors of Soft Tissue and Bone. Cancer. 2014;120(12):1763-1774.

2. Damron T, Ward W, Stewart A. Osteosarcoma, chondrosarcoma, and Ewing's sarcoma: National cancer data base report. Clin Orthop Relat Res. 2007 (459):40-47.

3. Marco R, Gitelis S, Brebach G, et al. Cartilage tumors: evaluation and treatment. J Am Acad Orthop Surg. 2000;8(5):292-304.

4. Gelderblom H, Hogendoorn P, Dijkstra S, et al. The Clinical Approach Towards Chondrosarcoma. Oncologist. 2008;13(3):320-329.

5. Meftah M, Schult P, Henshaw R. Long-term results of intralesional curettage and cryosurgery for treatment of low-grade chondrosarcoma. J Bone Joint Surg Am. 2013;95(15):1358-1364.

6. van der Geest I, de Valk M, de Rooy J, et al. Oncological and functional results of cryosurgical therapy of enchondromas and chondrosarcomas grade 1. J Surg Oncol. 2008;98(6):421-426.

7. Ruiz Santiago F, Castellano García M, Martínez Montes J, et al. Treatment of bone tumours by radiofrequency thermal ablation. Curr Rev Musculoskelet Med. 2009;2(1):43-50.

8. Cantwell C, Obyrne J, Eustace S. Current trends in treatment of osteoid osteoma with an emphasis on radiofrequency ablation. Eur Radiol. 2004;14(4):607-617.

9. Rimondi E, Mavrogenis A, Rossi G, et al. Radiofrequency ablation for non-spinal osteoid osteomas in 557 patients. Eur Radiol. 2012;22(1):181-188.

10. Tins B, Cassar-Pullicino V, McCall I, et al. Radiofrequency ablation of chondroblastoma using a multi-tined expandable electrode system: initial results. Eur Radiol. 2006;16(4):804-810.

11. Dierselhuis E, van den Eerden P, Hoekstra H, et al. Radiofrequency ablation in the treatment of cartilaginous lesions in the long bones: results of a pilot study. Bone Joint J. 2014;96-B(11):1540-1545.

12. Dierselhuis E, Jutte P, van den Eerden P, et al. Hip fracture after radiofrequency ablation therapy for bone tumors: two case reports. Skeletal Radiol. 2010;39(11):1139-1143.

13. Lee M, Ahn J, Chung H, et al. Osteoid osteoma treated with percutaneous radiofrequency ablation: MR imaging follow-up. Eur J Radiol. 2007;64(2):309-314.

14. Mertyna P, Hines-Peralta A, Liu Z, et al. Radiofrequency Ablation: Variability in Heat Sensitivity in Tumors and Tissues. J Vasc Interv Radiol. 2007;18(5):647-654.

15. Christoph R, Sprengel SD, Lehner B, et al. CT-guided radiofrequency ablation of osteoid osteoma and osteoblastoma: Clinical success and long-term follow up in 77 patients. Eur J Radiol. 2012;81(11):3426-3434.

16. Wang B, Han S, Jiang L, et al. Percutaneous radiofrequency ablation for spinal osteoid osteoma and osteoblastoma. Eur Spine J. 2017;26(7):1884-1892.

17. Arrigoni F, Barile A, Zugaro L, et al. CT-guided radiofrequency ablation of spinal osteoblastoma: treatment and long-term follow- up. Int J Hyperthermia. 2018;34(3):1-7.

18. Xie C, Jeys L, James S. Radiofrequency ablation of chondroblastoma: long-term clinical and imaging outcomes. Eur Radiol. 2015;25(4):1127-1134.

19. Christie-Large M, Evans N, Davies A, et al. Radiofrequency ablation of chondroblastoma: Procedure technique, clinical and MR imaging follow up of four cases. Skeletal Radiol. 2008;37(11):1011-1017.

20. Petsas T, Megas P, Papathanassiou Z. Radiofrequency ablation of two femoral head chondroblastomas. Eur J Radiol. 2007;1(63-67):63.

21. Lalam R, Cribb G, Tins B, et al. Image guided radiofrequency thermo-ablation therapy of chondroblastomas: Should it replace surgery? Skeletal Radiol. 2014;43(4):513-522.

22. Jones E, Oliphant E, Peterson P, et al. SciPy: Open Source Scientific Tools for Python.

23   Heerink W, Solouki A, Vliegenthart R, et al. The relationship between applied energy and ablation zone volume in patients with hepatocellular carcinoma and colorectal liver metastasis. Eur Radiol. 2018;28(8):3228-3236.

24.   Cassinotto C, Denys A, Gay F, et al. Radiofrequency Ablation of Liver Tumors: No Difference in the Ablation Zone Volume Between Cirrhotic and Healthy Liver. Cardiovasc Intervent Radiol. 2018;41(6):905-911.

25.   Hasgall P, Di Gennaro F, Baumgartne R, et al. IT'IS Database for thermal and electromagnetic parameters of biological tissues, Version 4.02018 [cited. www.itis.ethz.ch/database]

26.   Cheng Y, Fu M. Dielectric properties for non-invasive detection of normal, benign, and malignant breast tissues using microwave theories. Thoracic Cancer. 2018;9(4):459-465.

27.   Sha L, Ward E, Stroy B. A Review of Dielectric Properties of Normal and Malignant Breast Tissue. Procc IEEE SoutheastCon. 2002:457-462.

28.   Laufer S, Ivorra A, Reuter V, et al. Electrical impedance characterization of normal and cancerous human hepatic tissue. Physiol Meas. 2010;31(7):995-1009.

29.   Brace C. Radiofrequency and microwave ablation of the liver, lung, kidney and bone: What are the differences. Curr Probl Diagn Radiol. 2009;38(3):135-143.

30.   Pinto C, Taminiau A, Vanderschueren G, et al. Technical Considerations in CT-Guided Radiofrequency Thermal Ablation of Osteoid Osteoma: Tricks of the Trade. AJR Am J Roentgenol. 2002;179(6):1633-1642.

Chapter 3

Effects of control temperature, ablation time, and background tissue in radiofrequency ablation of osteoid osteoma: a computer modeling study

Ricardo Rivas [a*], Rudy B. Hijlkema [b], Ludo J. Cornelissen [a], Thomas C. Kwee[c], Paul C. Jutte[d], Peter M. A. van Ooijen [a]

[a] University of Groningen, University Medical Center Groningen, Department of Radiotherapy, Groningen, The Netherlands
[b] University of Groningen, Faculty of Mathematics and Natural Sciences, University of Groningen, Groningen, The Netherlands
[c] University of Groningen, University Medical Center Groningen, Department of Radiology, Groningen, The Netherlands
[d] University of Groningen, University Medical Center Groningen, Department of Orthopedics, Groningen, The Netherlands

Effects of control temperature, ablation time, and background tissue in radiofrequency ablation of osteoid osteoma: a computer modeling study

Abstract

Purpose

To study the effects of the control temperature, ablation time, and the background tissue surrounding the tumor on the size of the ablation zone on radiofrequency ablation (RFA) of osteoid osteoma (OO).

Materials and methods

Finite element models of non-cooled temperature-controlled RFA of typical OOs were developed to determine the resulting ablation radius at control temperatures of 70, 80, and 90°C. Three different geometries were used, mimicking common cases of OO. The ablation radius was obtained by using the Arrhenius equation to determine cell viability.

Results

Ablation radii were larger for higher temperatures and also increased with time. All geometries and control temperatures tested had ablation radii larger than the tumor. The ablation radius developed rapidly in the first few minutes for all geometries and control temperatures tested, developing slowly towards the end of the ablation. Resistive heating and the temperature distribution showed differences depending on background tissue properties, resulting in differences in the ablation radius on each geometry.

Conclusions

The ablation radius has a clear dependency not only on the properties of the tumor but also on the background tissue. Lower background tissue's electrical conductivity and blood perfusion rates seem to result in larger ablation zones. The differences observed between the different geometries suggest the need for patient-specific planning, as the anatomical variations could cause significantly different outcomes where models like the one here presented could help to guarantee safe and successful tumor ablations.

Keywords: radiofrequency ablation; osteoid osteoma; computer models; finite element method

Introduction

Radiofrequency ablation (RFA) is a minimally invasive technique that has become the treatment of choice for osteoid osteomas (OO), one of the most common types of bone tumors [1]. Since Rosenthal et al.'s initial findings [2], different settings have been tested to guarantee optimal treatment. Currently, the standard RFA for OO is a temperature-controlled mode of 90°C for 6 minutes [1], which originates from the first Rosenthal et al.'s experiments. Originally, they had decided on an ablation time of 3 minutes with a control temperature of 90°C, but the duration was later increased to 6 minutes after a (successful) attempt to reduce the number of tumor recurrences in [3] [2]. By increasing the ablation time, the amount of RF energy delivered to the tissue is increased, causing larger ablation zones.

Even though the ablation time is usually between 4 and 6 minutes, various studies have used longer times, ranging generally from 6 to 10 minutes [4] [5] [6] [7] [8] [9] [10]. In the case of electrodes of a smaller diameter, which produce smaller ablation volumes [11], ablation times of up to 14-15 minutes of active heating have been used [12] in an attempt to compensate for their reduced ablation volumes. However, the differences in ablation size between the standard approach of approximately 6 minutes and what others have proposed has not been quantified, and only the clinical outcomes were presented. Although the series are mostly successful, it is not clear what the ideal ablation time is, and what the quantitative effects of changing it are. Given that the main aim of the treatment is a reduction in pain, questionaries to assess the severity of the patient's pain are the main metric utilized before and after treating OO with RFA. Thus, post-operative imaging studies are not usually performed, making it hard to quantify the effects of changes in protocol on the ablation zone.

Goldberg et al. studied RFA on ex-vivo liver and muscle tissues and showed that the resulting ablation radius did not change after 6 minutes [11] had passed, which coincides with the initial suggestions by Rosenthal et al. However, the conclusions of this and other similar studies of RFA on liver or other soft tissues may not apply to bony tissues, hence the need for a systematic study of the effects of ablation time on OO.

Other clinical studies also opted to vary the control temperature, with most of them ranging from 60-90°C [7] [8] [9] [13] [14]. Generally, lower temperatures are used to prevent damaging nearby structures at risk like nerves (as this is expected to lead to a reduced ablation zone), and sometimes it may also be difficult to actually attain the target of 90°C and thus lower temperatures are used. However, again, the lack of post-operative imaging makes it hard to understand the effects on the thermal damage caused by the changes in the used control temperature.

To the best of our knowledge, no systematic study has been done on the consequences of varying the control temperature and ablation time of RFA on OO. These parameters have a direct impact on the extension of the ablation zone and therefore on the clinical outcome but testing on patients carries the risk of unsuccessful ablations, which could be detrimental to the patient's health. Therefore, we implemented computer models using the finite element method (following the previous work on OO by Irastorza et al. [15]) to study the effect of control temperature and ablation time on ablation size. We tested this on 3 typical anatomical configurations of OO and looked at how the different tissues surrounding the tumor affected the extension of the ablation.

Materials and Methods

Finite element models of non-cooled temperature-controlled RFA of typical OOs were developed, following mostly the work by Berjano [16] and Irastorza et al. [15], to determine their dynamic temperature distribution and cell death at various control temperatures and durations. Based on the studies mentioned in the introduction, the models were studied with control temperatures of 70, 80, and 90°C, and for as long as 15 minutes of active heating.

Description of the geometry

There were two main objectives when creating the geometries: 1) to approximate common cases of OO and 2) to explore the effects of different anatomical configurations of RFA on OO. Examples of common cases can be seen in Figure . With these cases in mind, we decided to test three different scenarios: The first, a juxtacortical nidus (the tumor) surrounded by a layer of sclerosis which in turn is surrounded by trabecular and cortical bone (Figure 4A). The second, similar to the first, but without the sclerotic layer and with the nidus surrounded by trabecular bone (Figure 4B). The third, an intracortical nidus with no trabecular bone or sclerotic layer directly around it (Figure 4C). The third case could also serve as an example of how the ablation radius changes in the longitudinal direction of bone. All the geometries had a final layer of muscle surrounding the cortical bone. The nidus, a sphere with a 1 cm diameter, was treated with an electrode with an active tip of 0.75 cm in length and gauge 17, in accordance with common practice by interventionists. To simplify the complex anatomy, a rectangular cortical bone shape was chosen with dimensions similar to those of a typical tibia. All the geometries were defined as 2D axisymmetric, with the axis of symmetry along the electrode. Given that most of the cell death occurs close to the electrode, we found these geometrical approximations to be sufficient for the tests; increasing the distance further or changing the shape of the cortical box or the surrounding muscle did not change the outcome significantly. Mesh convergence tests were performed on the three models to guarantee mesh independence in our results, and special attention was paid to the size of the elements next to the electrode where the highest

gradients were located. The cell death radius (explained in the next section) was used as the convergence criterion. Convergence was assumed to have occurred when a change of less than 1% in the cell death radius was obtained. Triangular elements with a characteristic length as small as .1 mm were tested.
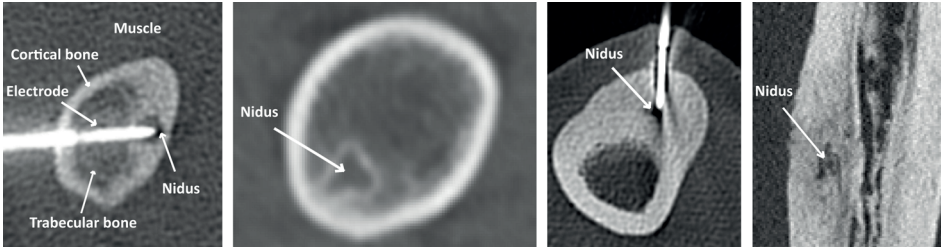
Figure 1. Three examples of common cases of OO. The hypodense focus corresponds to the location of the nidus. The first image shows a nidus with a thin layer of sclerosis surrounded by both cortical and trabecular bone in a femur. The second image shows a nidus with little sclerosis and surrounded mostly by trabecular bone. The third image shows an intracortical nidus completely covered by cortical bone in a tibia. The right-most image shows another intracortical OO but now from a different view. The first and third images show an example of how the electrode (the hyperdense-bright object) is usually placed in the nidus. The first image is labeled to work as a reference, and in the following ones the tumor was indicated for clarity.
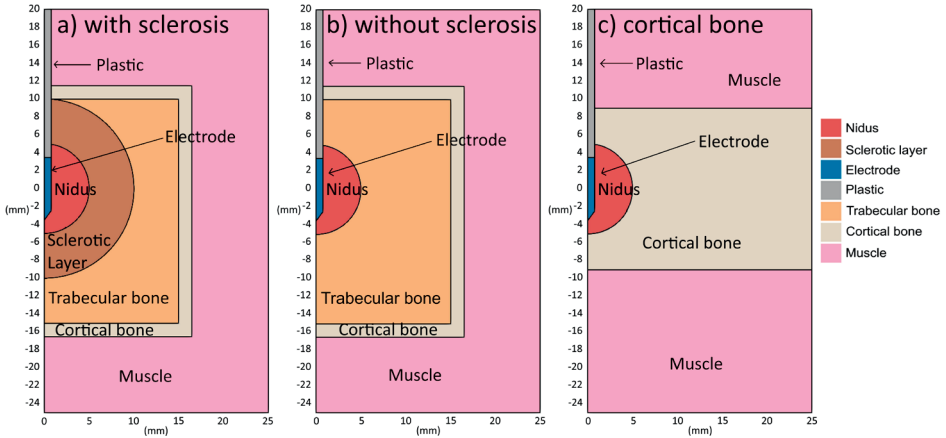
Figure 2. Geometries mimicking typical cases of OO, roughly matching the cases from Figure . a) is a case of an OO surrounded by a layer of sclerosis. b) is a case of an OO in the middle of trabecular bone close to a cortical wall. c) is a case of an OO completely surrounded by cortical bone, and that could also represent the extent of thermal ablation along the longitudinal axis of bone. All three cases are further surrounded by a layer of muscle.

Equations governing radiofrequency ablation

In RFA, heat is generated due to Joule heating which then propagates through the body. The simulations thus consisted of solving a coupled electric-thermal problem, in which the thermal problem was governed by Pennes' bioheat equation [17] modified to account for phase change due to tissue vaporization [18]:

$$\frac{\partial h}{\partial t} = \nabla \cdot (k_i(\mathbf{T})\nabla \mathbf{T}) + \mathbf{Q_{RF}} - \mathbf{Q_p} \tag{1}$$

Where h is the enthalpy, and k_i is the thermal conductivity (W/m · K). These properties are temperature dependent, as described by the piece-wise functions below. T is the temperature (K), t time (s) and Q_{RF} the heat source (W/m^3). Q_p is the blood perfusion heat loss (W /m^3) and is defined as:

$$Q_p = \omega_i(\Omega)\rho_b c_b[T - T_b] \tag{2}$$

Where ρ_b is the density of blood (kg / m^3), c_b the specific heat of blood (J/kg · K), T_b the temperature of blood (K). ω_i is the tissue-dependent perfusion coefficient (s^{-1}) as a function of the cell viability Ω. The perfusion of each cell is kept constant and becomes zero when it dies, as specified by the cell death model.

A quasi-static approach was used for the electrical problem as it is known that tissues in the area of interest can be seen as totally resistive to the RF ablation frequencies ($\approx$ 500 kHz) [19]. Then, the heat source Q_{RF} is given by:

$$Q_{RF} = \sigma_i|\mathbf{E}|^2 \tag{3}$$

Where E is the electric field intensity (V/m) and σ_i is the electrical conductivity (S/m) of each tissue. The electric problem is then stated by the Laplace equation:

$$\nabla \cdot \sigma_i(T)\nabla V = 0 \tag{4}$$

where V is the root mean squared value of the applied voltage (V).

The following boundary conditions were set: a Neumann boundary condition of zero thermal flux at the symmetry axis and a Dirichlet boundary condition of constant temperature of 37°C at the outer boundaries for the thermal problem. Also, a Dirichlet boundary condition of zero voltage at the outer boundaries to mimic the grounding pad, a Neumann boundary condition of zero flux at the symmetry axis, and a Dirichlet boundary condition with a value equal to the applied r.m.s. voltage at the electrode surface were employed for the electric problem.

To mimic the clinical setting, the voltage was regulated such that a pre-defined temperature at the tip of the electrode was reached, and subsequently maintained, which can be modeled by using a PI-controller, i.e.

$$V_{r.m.s.} = K_p\big(T_{target} - T(t)\big) + K_i \int_0^\tau (T_{target} - T(t)) \, dt \tag{5}$$

Where $V_{r.m.s.}$ is the r.m.s. voltage (V) set at the electrode boundary, T_{target} the desired control temperature, $T(t)$ the temperature at the tip at time t, K_p the error proportionality constant, and K_i the integral proportionality constant. The initial voltage was set to zero. Then the K_p and K_i values had to be found with similar behaviors as in the ex- Bitsch et al. experiments [20]. Although this is model dependent, a good agreement was found by setting K_p at 1.15 V/K and K_i at 0.06 V/K/s [21].

For most of the model, the Trujillo and Berjano [22] model propositions for biological tissues, temperature-dependent parameters of electrical conductivity, thermal conductivity, and apparent heat capacity were used as reference.

Regarding electrical conductivity, a linear increase of 1.5% per degree Celsius until the point of vaporization was used. Then, vaporization is characterized as a sudden drop in the electrical conductivity, with a linear decrease up to a factor of 10000, as described in equation 6.

$$\sigma_i(T) = \begin{cases} \sigma_i + \Delta\sigma_i(T - 37\,°C), & T \leq 100\,°C \\ \sigma_{100°C} + (\sigma_{vap} - \sigma_{100°C})\dfrac{(T - 100\,°C)}{5}, & 100°C < T \leq 105\,°C \\ \sigma_{vap}, & T > 105\,°C \end{cases} \quad (6)$$

where σ_i is the baseline electrical conductivity (S/m) of each tissue at 37 °C, $\Delta\sigma$ is the 1.5% temperature dependent rate of change in electrical conductivity per degree Celsius, and σ_{vap} is the modeled electrical conductivity of vaporized tissue where $\sigma_{vap} = 10x10^{-3}$ (S/m) [22].

The thermal conductivity was considered as having a linear increase until the point of vaporization where a maximum value was set for any temperature beyond 100 °C:

$$k_i(T) = \begin{cases} k_i + \Delta k_i(T - 37\,°C), & T \leq 100\,°C \\ k_i + \Delta k_i(100\,°C - 37\,°C), & T > 100\,°C \end{cases} \quad (7)$$

where k_i is the baseline thermal conductivity of each tissue at 37 °C and Δk_i corresponds to a 0.003 change in thermal conductivity per degree Celsius [15] [23].

When water starts to evaporate there is a sudden change in the heat capacity during the phase-change. Although tissue vaporization is not expected because the PI controller will regulate the output current to maintain a maximum target temperature of 90 °C, tissue vaporization was modeled using the enthalpy method [18] [22]:

$$h = \begin{cases} \rho_i c_i(T - 37°C), & 37\,°C \leq T \leq 99\,°C \\ h(99) + h_{fg}C_i \dfrac{(T-99°C)}{(100°C-99°C)}, & 99°C < T \leq 100\,°C \\ h(100) + \rho_{vap}c_{vap}(T - 100°C), & T > 100\,°C \end{cases} \quad (8)$$

where $\rho_i c_i$ represent the baseline density $(\frac{kg}{m^3})$ and specific heat $(\frac{J}{kgK})$ of each tissue, $\rho_{\text{vap}}(370 \frac{kg}{m^3})$ and c_{vap} $(2156 \frac{J}{kgK})$ are the density and specific heat of vaporized tissue [22], h_{fg} is the latent heat of vaporization $(2.25\text{x}10^6 \frac{J}{kg})$ and C_i is the water fraction of each tissue.

FEniCS [24], an open-source platform for solving partial differential equations, was used to develop a solver for our models. The implementation was based on the works by Hall [25], who developed a model to solve various minimally invasive tumor ablation therapies (e.g., RFA, Microwave ablation, etc.) using FEniCS.

Tissue properties

Most of the tissue properties were obtained from [26], except for the sclerotic layer and nidus (where we followed Irastorza's assumptions), or as indicated otherwise in Table 1. We also followed Irastorza's assumed blood perfusion values for all tissues. The properties of plastic and metal were taken from [27]. In most cases, where a range of values was available, the average value was chosen. The only exceptions where in the specific heat and thermal conductivity of the reactive zone, for which we used cortical bone values to simulate the effects of a high degree of sclerosis but still with some blood perfusion.

Table 1. Material's properties. All properties were obtained from [26] for tissues at 500 kHz, except where marked. The references correspond to a [27], b [15], c [28], d [29], e [30] * correspond to the values of cortical bone from [26]. The water fraction of connective tissue was assumed for the nidus and the water fraction of cortical bone was assumed for the sclerotic layer.

Material/ tissue	Density (kg/m3)	Electrical conductivity (S/m)	Specific heat (J/kg · K)	Thermal conductivity (W/m/K)	Blood perfusion coefficient $(x10^{-4}s^{-1})$	Water fraction
Electrode	6450[a]	1.00E+08[a]	840[a]	18[a]	0	0
Plastic	70[a]	1.00E-05[a]	1045[a]	0.026[a]	0	0
Nidus	1046[b]	0.22[b]	2726[b]	0.56[b]	48[b]	.60[d]
Sclerotic layer	1908[b]	0.0535[b]	1313[*]	0.32[*]	2.95[b]	.23[c]
Trabecular bone	1178	0.0867	2274	0.31	5.90[b]	.27[c]
Cortical bone	1908	0.022	1313	0.32	0.00[b]	.23[c]
Muscle	1090	0.446	3421	0.49	6.70b	.76[e]

Cell death model

To assess the tissue damage caused by the heating process we used the Arrhenius damage model [31]. The cell viability of a given tissue is given by Ω, which calculates the thermal damage to each cell over time:

$$\Omega(t) = \int_0^t Ae^{-\frac{\Delta E}{RT(\tau)}} \, d\tau, \tag{9}$$

where R is the universal gas constant, A (a frequency factor), and ΔE (the activation energy for the irreversible damage reaction) the cell-line dependent parameters. Since the treatment is on bone tumors, and Tillotson et al. found that cortical and trabecular bone have roughly the same susceptibility to heat [32], osteocytes seemed like the best option from the cell-line parameters found in literature, with values of $8.99 \, x \, 10^{133} s^{-1}$ and $\Delta E = 838 \, \text{kJ/mol}$. [33]

Cell death (Ω) is given as a probability of cell viability, where exposure to higher temperatures for longer periods increases the likelihood of a given cell dying. A value of $\Omega = 4.6$ was chosen as the threshold, corresponding to a 99% probability of cell death. Once a cell reached said threshold, it was considered dead and the perfusion was stopped. To calculate the outcome for our studies, a radius from the center of the electrode in directions perpendicular and parallel (upwards) to the electrode was used to calculate the resulting cell death radius in both directions. Additionally, we allowed the simulations to cool down for five minutes (chosen arbitrarily based on preliminary results) after the active electrode was turned-off to capture the thermal damage more accurately over time while the heat was still dissipating, as shown in [33].

Validation of the model

Our model is based on the computer model by Irastorza et al. [21], who modeled radiofrequency ablation of OO and compared their results to the ex-vivo experiments by Bitsch et al. [21]. To validate our model, the Irastorza et al. model was replicated as best as possible and the results from our model were compared against their results and against the ex-vivo experiment by Bitsch et al. The values from their studies were obtained with WebPlotDigitizer [34] and compared against the results from our simulations.

Bitsch et al. created three OO models using bovine long bone specimens, categorized depending on the thickness of the cortical bone lamella separating the nidus from the periosteum. A hole was drilled and filled with 0.8% agarose gel to model the nidus. In the soft tissue surrounding bone, three thermocouples were placed at distances of 0, 5, and 10 mm from the periosteum. The specimens were heated to an internal temperature of 35 °C, and RFA was performed for 400 seconds with a control temperature of 95 °C. The temperatures measured by the thermocouples were reported in graphs. The ex-vivo setting was then replicated by Irastorza et al. using the temperature profiles obtained from the temperature probes to validate and optimize their OO model. Of the three Bitsch et al. models, the one with a 3 mm lamella thickness was chosen arbitrarily here, but our model was compared against all their configurations. For a more detailed explanation of the ex-vivo experiments and the assumptions to replicate them, please refer to Bitsch et al. [20] and Irastorza et al. [21], respectively.

Results

Validation

The results were within 1°C degree of difference to the ones obtained by Irastorza et al. for most of the ablation time with a maximum absolute error of 2.2 °C, encountering the largest differences for the probe closes to the tumor and almost identical results for the other two. Against the Bitsch et al. results, a maximum absolute error of 4.3 °C of difference was found.
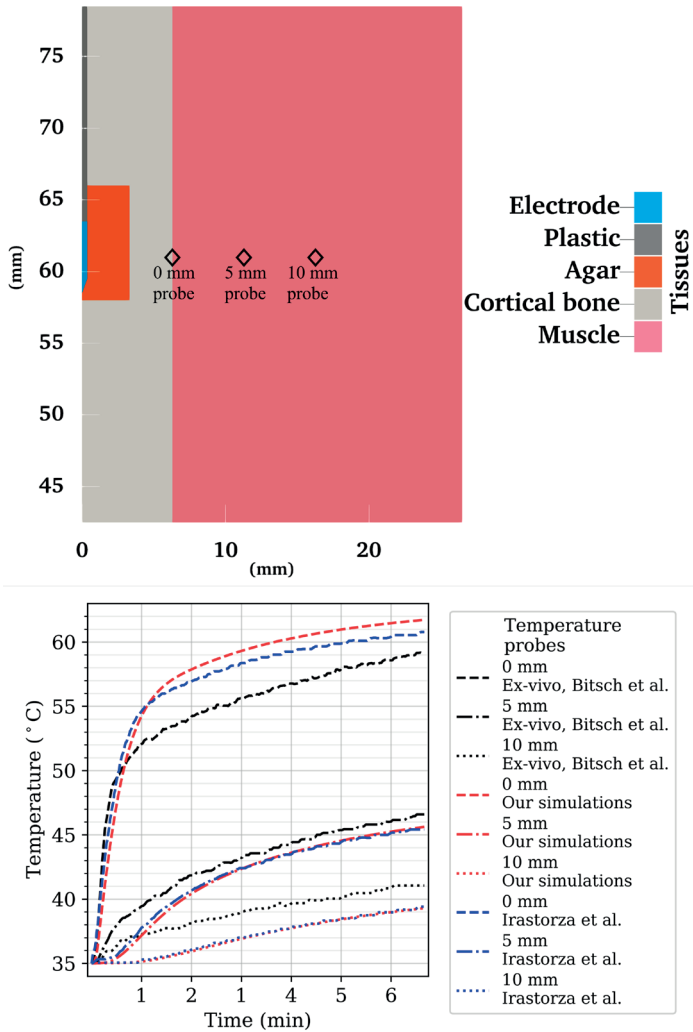
Figure 3. Top: Geometry used to replicate one of the Bitsch et al. ex-vivo experiments, where temperature probes were positioned at 0-, 5-, and 10-mm distance from the lamella, here shown as the black rhombuses in the geometry. Bottom: Temperature in time for the 3 probes. In black, Bitsch. et al ex-vivo experiments; in red, our simulations; in blue, Irastorza et al.'s simulations.
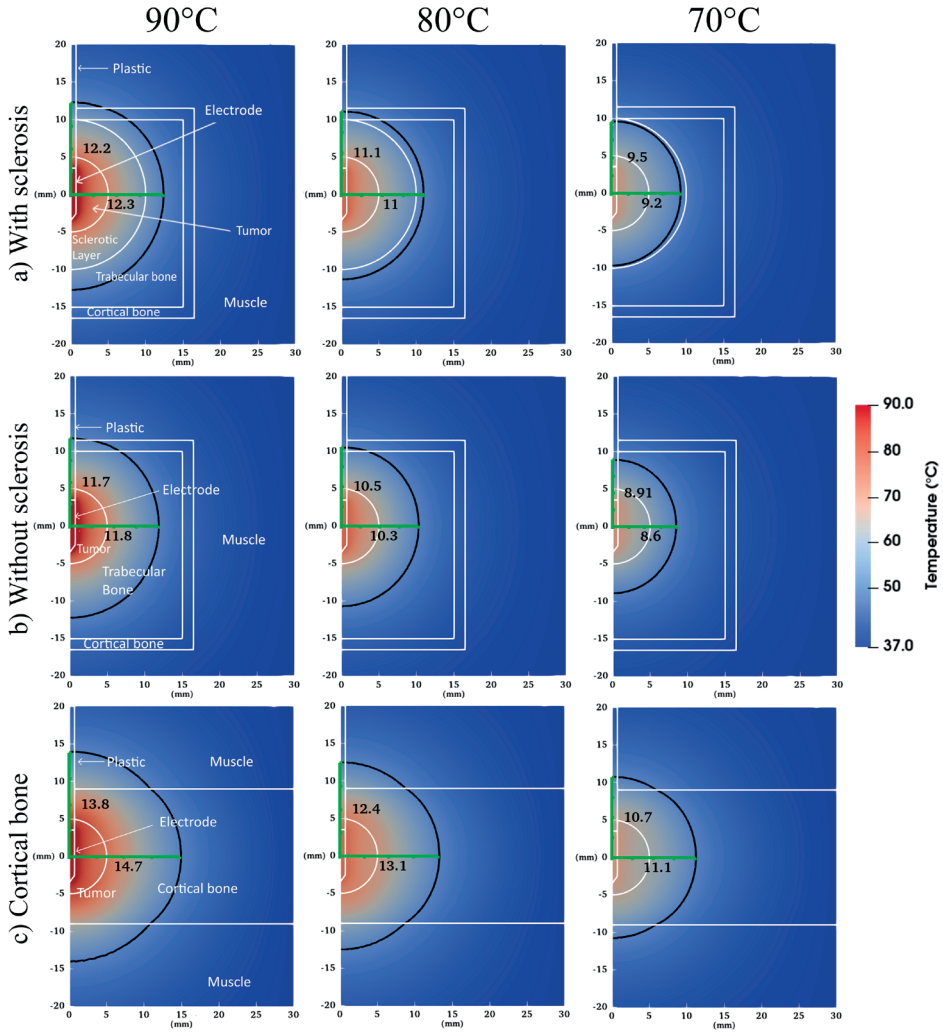
Figure 4. Simulated temperature distribution for the three different geometries and three control temperatures after 15 minutes of ablation. White lines represent the geometry of the model and the black line represents the resulting cell death isoline. The green line indicates the distance from the center of the electrode to the isoline, i.e., the radius used as the outcome variable.

Effects of time and control temperature

Figure 6 shows the temperature distributions of the three tested simulation models at the end of active heating (at 15 min), for all control temperatures. Cell death and measurements are also shown, obtained after 15 min of ablation + 5 min of cooldown. None of the tested models and configurations tested reached maximum temperatures of ≥ 100 °C, and there was no tissue vaporization.

Figure 7 shows all the radii obtained for all the geometries tested with different control temperature configurations and durations. The dash-dot line corresponds to the radius of the nidus, to enable visual comparison of the obtained radius in each configuration against the target tissue to be ablated (the nidus). The number in each label indicates the control temperature used. The X and Y indicate the directions in which the temperature isotherm was obtained: X, perpendicular to the electrode; Y, parallel to the electrode. Both measurements start at the center of the electrode, and the Y direction was measured from the center to the top.
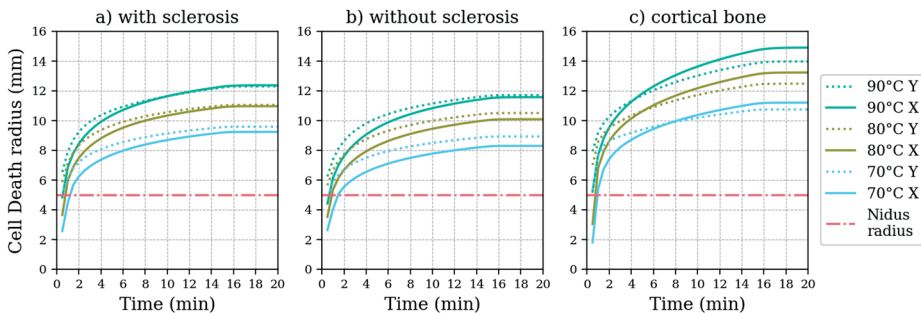
Figure 5. Radii of the cell death isoline obtained for the geometries tested under all the configurations. The number in the labels indicates the control temperature and the X or Y indicate whether it was measured in direction perpendicular (X) or parallel (Y) to the electrode. The straight dash-dot line indicates the radius of the nidus. The first few initial values were omitted for clarity.

The ablation radii were larger at higher temperatures, and also increased with time, as expected. The ablation radii of all the tested geometries and control temperatures were larger than the tumor at the end of the ablation. The ablation radius developed rapidly in the first few minutes and then slowed down by the end of the ablation. The ablation radius was smallest for geometry b), followed by geometry a), and largest in geometry c), when compared at the same control temperature. The radius was almost identical in both directions for the first two cases, whereas in geometry c), the ablation radius increased considerably more in the direction perpendicular to the electrode after a couple of minutes for all the tested control temperatures.

To test the sensitivity of the models further to changes in the tissue parameters, we performed simulations with four combinations of maximum and minimum electrical conductivity (0.5 S/m and 0.08 S/m, respectively) and blood perfusion ($70 \times 10^{-4} s^{-1}$ and $26 \times 10^{-4} s^{-1}$) values in the nidus. These parameters were chosen because they are the most influential factors defining the size of the ablation radius [35]. The values were taken from Irastorza et al.'s study [15]. For all target temperatures and anatomical configurations, the ablations were performed for 15 minutes of active heating plus five minutes of cooldown at the end. Only the material parameters of the tumor were changed because the three geometries tested already presented great variations in the tissues surrounding the tumor. The results in Figure **8** show that the ablation

radius changes depended mostly on the effects of electrical conductivity, with the perfusion having little to no effect. Compared to the ablation radius with the baseline parameters, a change in the ablation zone radius of approximately +15% for the cases with a higher nidus electrical conductivity and -15% for the cases with the lower electrical conductivity was seen for all configurations. Additionally, since the parallel and perpendicular radii showed the same kind of relative relationship between them as the average cases already explored, we omitted the parallel radius from the graphs for clarity purposes.
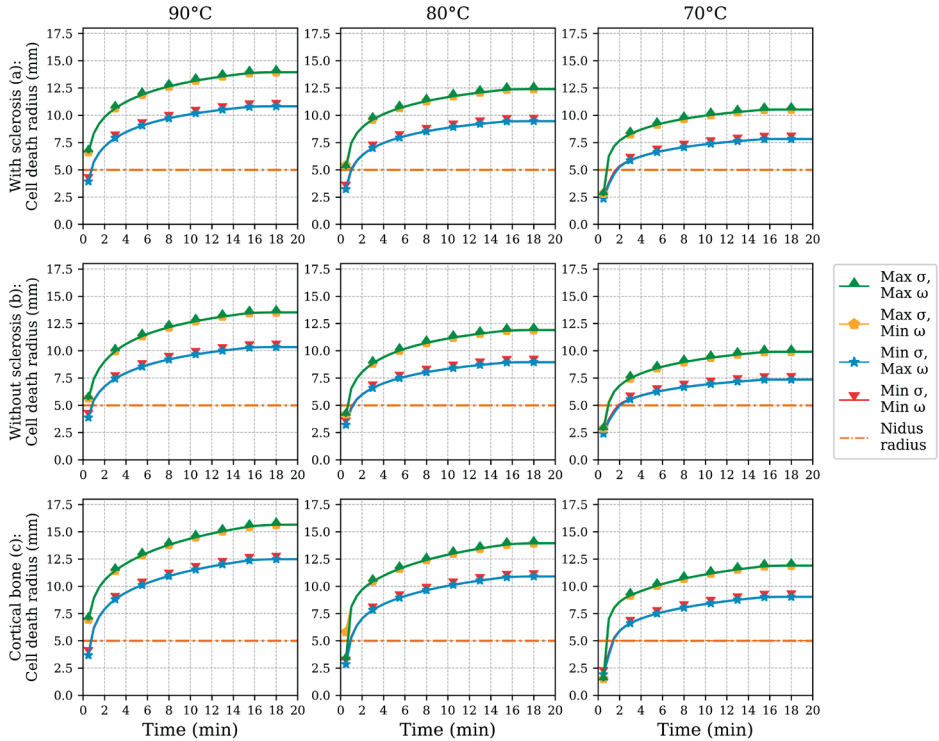
Figure 6. Analysis on the effects of the tumor's electrical conductivity (σ) and blood perfusion (ω) on the resulting maximum ablation. Combinations of maximum and minimum values of σ and ω were tested in all three geometries, as described in the labels. The straight dash-dot line indicates the radius of the nidus. The initial first few initial values were omitted for clarity.

Finally, to understand the reason for the differences in the ablation radii in the different models better, we obtained a line graph of the resistive heating and the temperature from the center of the electrode and perpendicular to it. Only cases with a control temperature of 90°C are presented as examples but the trends presented in Figure **9** were true for all the control temperature configurations.
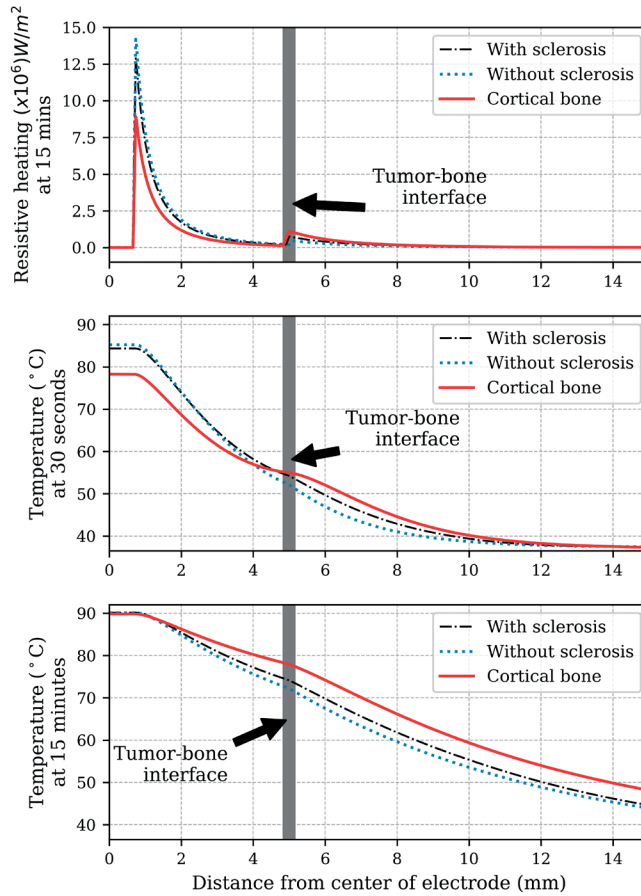
Figure 7. Line graphs of the resistive heating and temperature of the three models tested, from the center of the electrode and perpendicular to it, with a control temperature of 90 °C. The tissue interface between the tumor and bone is located at 5 mm. Two representative points in time were chosen for the temperature profiles, one close to the beginning of the procedure (30 seconds) and one at the end (15 minutes) to highlight the contrast in the distribution of heat at the beginning and at the end of the ablation. The distribution of the resistive heating did not change significantly over time, so only one line graph is shown, obtained at 15 minutes.

The distribution of the resistive heating demonstrates clear differences in the distribution of the induced heat that depend did not only depend on the target tissue (nidus) but on the surrounding tissue as well. This is particularly clear in the peak at the electrode-tumor interface (at .75 mm) and at the tumor-bone interface (at 5 mm). The amount of induced heat varied with time as a function of the voltage applied but its distribution remained more or less the same all the time. Hence, only one graph of the 15 minutes measurement is shown.

The temperature profile also shows the effects of the differences on the distribution of induced heat. At the beginning of the ablation, the case with the tumor surrounded by cortical bone

seems to induce less heat around the tumor, but creates an additional peak of heat at the tumor-bone interface, which, with time, increases the maximum temperatures reached deeper in the tissue. It is also interesting to note that all the cases seem to have similar heat transfer rates after the tumor (at 5 mm), as shown in the slope of the temperature profile.

Discussion

Radiofrequency ablation is a technique that has been consolidated as a standard clinical practice for the treatment of OO due to its effectiveness and low complication rates. However, neither the effects of the ablation time, nor the control temperature, nor the effects of the background tissue surrounding the tumor on the resulting ablation zone are well understood. Some studies have used ablation times as short as four minutes [36] whereas in others the time has been as long as 15 minutes [12] to treat similar types of lesions. Also, deliberate variations in control temperature, with the aim of generating smaller ablation zones, have been reported, usually for small tumors or tumors near structures at risk [14]. Nonetheless, quantitative analysis of the effects of these parameters has not been done, and their impact on the resulting ablation zone is not clear. Additionally, it is well known that the characteristics of both the target tissue (the nidus in this case) and the tissue surrounding it have a big impact on the resulting ablation zone. To explore the effects of all these parameters in a systematic way, we developed finite element models to simulate RFA of OO under multiple configurations of control temperature, ablation time, and anatomical location of the tumor.

In some of the first RFA studies with OO, Rosenthal et al. concluded that little to no change was achieved in the extent of the ablation zone after approximately three minutes but that nevertheless, in clinical practice, the patients seemed to experience less recurrences when the duration of the RFA was increased to six minutes [36] Other studies even claimed to notice a difference in the clinical outcomes by increasing the ablation time to up to 15 minutes [12]. Our results showed that an ablation tends to develop rapidly, achieving most of the ablation radius during the first few minutes, and then actually grows slowly so that it develops considerably during the whole 15 minutes of active heating and perhaps even longer. This was true for all the simulated OO geometries and for every control temperature, and especially true for geometry c) where the ablation radius was the largest and it grew the most with time.

A possible explanation for the different radii obtained with each model may be due to the effects of blood perfusion. Schutt and Haemmerich [37]s showed that cirrhotic livers (with lower perfusion rates) had larger ablations zones than normal healthy livers because of what has been called the "oven effect". Highly perfused tissues usually act as heat sinks, increasing the rate in which heat is drawn away, whereas non-perfused tissues surrounding the tumor could be

seen as a sort of oven, as with cirrhotic livers, allowing more heat to concentrate in the tumor and its surroundings. Cortical bone also has little to no blood perfusion. A nidus surrounded by cortical bone could therefore be compared to cirrhotic livers, with cortical bone causing the oven effect. This could also explain why the tumor surrounded by trabecular bone had the smallest ablation radius of all, as the trabecular bone was modeled with the highest perfusion of all the three models whereas in the case of geometry b), it was immediately next to the tumor, acting as a heat sink. Regarding geometry a), the electrical conductivity and perfusion modeled for the sclerotic layer was somewhere between that seen in cortical bone and trabecular bone, and the results that were somewhere between the other two models. Additionally, geometry c)'s ablation radius grew larger in the direction perpendicular to the electrode than in the parallel direction. As the ablation radius grew in size, it reached the muscle boundary in the parallel direction, and its high perfusion could have acted as a heat sink. The nidus's blood perfusion did not seem to have a significant effect on the outcome of the ablation radius. In fact, the ablation radius quickly became bigger than the nidus, which caused the nidus's blood perfusion to stop when its cells died.

However, we think that a more plausible explanation for the overall results may be due to the differences in the electrical conductivity of the tumors and their surrounding tissue. It is known that the electrical conductivity of the target tumor is crucial in defining the volume of the ablated tissue, with higher electrical conductivities allowing for more energy deposition and thus larger ablation volumes. Yet, Solazzo et al. [38] showed that the electrical conductivity of the background tissue also has a strong influence on how the energy is deposited and therefore on the thermal distribution. They varied the electrical conductivity of the target tissue and its surroundings with a phantom and a computer model and demonstrated that when the background tissue had the same electrical conductivity as the target tissue, the electrical and thermal distribution decreased smoothly from the electrode towards the outer boundaries of the model. However, when the electrical conductivity of the background tissue was lower, they observed a secondary electric field peak at the tissue interface, which was associated with a "wider" temperature distribution (i.e., higher temperatures going deeper). When the electrical parameters were reversed, whereby the target tissue had low electrical conductivity and the surrounding tissue had increased electrical conductivity, the opposite effect occurred. In this case, there was no heat generation at the tissue interface, causing a "compressed" temperature distribution, since high temperatures were only found close to the electrode. These results are analogous to what we found where the cortical bone seemed to produce larger ablation radii because of an additional resistive heating peak at the nidus-bone interface. This effect is more noticeable when we compare geometries b) and c), because trabecular bone has considerably lower electrical conductivity than cortical bone, and as such the model with trabecular bone had a smaller resistive heating peak and a smaller ablation radius.

Irastorza et al. mentioned a similar trend in their computer models of OO, where they studied the presence of the layer of sclerosis using various degrees of vascularization and bone density. In their study, the ablation radius increased with decreasing electrical conductivity of the reactive zone, and an additional peak in the temperature distribution, which is similar to what Solazzo et al found [15] [38]. This confirms the importance of the background tissue on the resulting ablation zone, and shows how surrounding tissue with lower conductivity can lead to an increased ablation zone. This also illustrates that while bone is a good thermal and electrical insulator, bony background tissue will alter the heat induction profile, particularly when there is a high mismatch between the target tissue and the background tissue, as shown by Solazzo et al. [38]. The consequences of this effect may seem counter-intuitive at first, given that bone is a good insulator, but experiments have demonstrated that, particularly in the case of background cortical bone, it could potentially lead to larger ablations in comparison to other background tissues.

The effects of this mismatch in electrical conductivity were stronger when the electrical conductivity of the nidus was increased further, resulting in even larger ablation radii than the ones produced with the original settings. These variations in tumor properties, however, also showed that the blood perfusion of the tumor had little impact on the heat distribution in comparison to the electrical conductivity. This lack of dependency on the blood perfusion seemed to be because of how quick the ablation zone encompassed the nidus, stopping the nidus's blood perfusion in the first seconds to a minute of the procedure. This insight could be particularly important in cases where RFA is used to treat a malignant bone tumor because tumor tissues, especially malignant ones, seem to demonstrate much higher electrical conductivity compared to healthy tissue.

Our experiments show that ablation outcomes are highly tissue dependent, and not only on the properties of the target, but also on its surrounding tissues, which suggests the need for accurate patient specific imaging and treatment planning. This could be particularly important for tumors close to structures at risk, and considerations should be made based upon both the tumor properties and its surrounding tissue. Computational modeling for patient specific planning could play an important role to guarantee the success of the procedures.

A limitation of this study is the lack of validation of the model against clinical or in-vivo models; it could only be validated against ex-vivo OO experiments. However, since the model correlated accurately to the ex-vivo experiments, one can assume that the model demonstrates the effects and importance of the tested parameters with clinically useful levels of agreement.

Chapter 3

Conclusion

The ablation radius of RFA on OO is clearly dependent on the target temperature and ablation time, where higher temperatures and longer ablation times produce higher ablation radii. The ablation radii grow rapidly during the first few minutes and continue to grow, although slowly, until the electrode is turned off after 15 minutes. The size of the ablation radius clearly depends on the background tissue surrounding the tumor, where tissues with lower electrical conductivity led to an increased ablation radius, and this effect increases when the electrical conductivity of the tumor is increased as well. The blood perfusion of the tumor does not seem to have an important effect on the resulting ablation radius. This suggests the need for patient specific imaging and planning of the procedures, where computational models like the one presented here could help to give more accurate and personalized patient treatment.

References

[1] D. Motamedi, T. J. Learch, D. N. Ishimitsu, Motamedi¸Kambiz, M. D. Katz, E. W. Brien and L. Menendez, "Thermal Ablation of Osteoid Osteoma: Overview and Stepby-Step Guide," RadioGraphics , vol. 29, no. 7, pp. 2127-2141, 2009.

[2] D. Rosenthal, F. Hornicek, M. Wolfe, L. Jennings, M. Gebhardt and H. Mankin, "Percutaneous Radio-frequency Coagulation of Osteoid Osteoma Compared with Operative Treatment," J Bone Joint Surg Am, Vols. 80-A, no. 6, pp. 815-821, 1998.

[3] D. Rosenthal, A. Alexander, A. Rosenberg and D. Springfield, "Ablation of Osteoid Osteomas with a percutaneously placed electrode: A new procedure," Radiology, vol. 183, no. 1, pp. 29-33, 1992.

[4] M. A. S. S. D. O. G. W. L. B. W. B. K. H. U. &. R. C. Weber, "Clinical long-term outcome, technical success, and cost analysis of radiofrequency ablation for the treatment of osteoblastomas and spinal osteoid osteomas in comparison to open surgical resection," Skeletal Radiol, vol. 44, no. 7, pp. 981-993, 2015.

[5] R. Rehnitz, S. Sprengel, B. Lehner, K. Ludwig, G. Omlor, C. Merle, H. Kauczor, V. Ewerbeck and M. Weber, "CT-guided radiofrequency ablation of osteoid osteoma and osteoblastoma: clinical success and long-term follow up in 77 patients," Eur J Radiol, vol. 81, no. 11, pp. 3426-34, 2012.

[6] D. Rosenthal, F. Hornicek, M. Torriani, M. Gebhardt and H. Mankin, "Osteoid osteoma: percutaneous treatment with radiofrequency energy," Radiology, vol. 229, no. 1, pp. 171-175, 2003.

[7] R. Hoffmann, T. Jakobs, C. Kubisch, C. Trumm, C. Weber, H. Duerr, T. Helmberger and M. Reiser, "Radiofrequency ablation in the treatment of osteoid osteoma-5-year experience," Eur J Radiol, vol. 73, no. 2, pp. 374-379, 2010.

[8] K. Sung, J. Seo, J. Shim and Y. Lee, "Computed-tomography-guided percutaneous radiofrequency thermoablation for the treatment of osteoid osteoma-2 to 5 years follow-up," int Orthop, vol. 33, no. 1, pp. 215-1218, 2009.

[9] S. Mylona, S. Patsoura, P. Galani, G. Karapostolakis, A. Pomoni and L. Thanos, "Osteoid osteomas in common and in technically challenging locations treated with computed tomography-guided percutane-ous radiofrequency ablation," Skeletal Radiol., vol. 39, no. 5, pp. 443-449, 2010.

[10] A. Paladini, P. Lucatelli, F. Cappelli, G. Pizzi, V. Anelli, E. Amodeo, D. Beomonte Zobel, L. Paladini, R. Biagini, D. Attala, C. Zoccali and G. Vallati, "Osteoid osteoma treated with radiofrequency ablation in non-operating room anesthesia. A different way of approaching ablative therapy on osteoid osteoma," Eur Rev Med Pharmacol Sci, vol. 22, no. 17, pp. 5438-5446, 2018.

[11] S. Goldberg, G. Gazelle, S. Dawson, W. Rittman, P. Mueller and D. Rosenthal, "Tissue Ablation with Radiofrequency: Effect of Probe Size, Gauge, Duration, and Temperature on Lesion Volume," Acad Radiol, vol. 2, pp. 399-404, 1995.

[12] E. Rimondi, A. Mavrogenis, G. Rossi, R. Ciminari, C. Malaguti, C. Tranfaglia, D. Vanel and P. Ruggieri, "Radiofrequency ablation for non-spinal osteoid osteomas in 557 patients," Eur Radiol, vol. 22, pp. 171-188, 2012.

[13] U. Albisinni, A. Bazzocchi, G. Bettelli, G. Facchini, E. Castiello, M. Cavaciocchi, G. Battista and R. Rotini, "Treatment of osteoid osteoma of the elbow by radiofrequency thermal ablation," J Shoulder Elbow Surg., vol. 23, no. 1, pp. e1-7, 2014.

[14] B. Gebauer, F. Collettini, C. Bruger, K. Schaser, I. Melcher, P. Tunn and F. Streitparth, "Radiofrequency Ablation of Osteoid Osteomas: Analgesia and Patient Satisfaction in Long-term Follow-up," Rofo, vol. 185, no. 10, pp. 959-966, 2013.

Chapter 3

[15]   R. Irastorza, M. Trujillo, J. Villagrán and E. Berjano, "Computer modelling of RF ablation in corti-cal osteoid osteoma: Assessment of the insulating effect of the reactive zone," International Journal of Hyperthermia, vol. 32, no. 3, pp. 221-230, 2016.

[16]   E. J. Berjano, "Theoretical modeling for radiofrequency ablation: state-of-the-art and challenges for the future," Biomed Eng Online, vol. 5, no. 24, 2006.

[17]   H. Pennes, "Analysis of tissue and arterial blood temperatures in the resting human forearm," Applied physiology, vol. 1, no. 2, pp. 93-122, 1948.

[18]   J. Abraham and E. Sparrow, "A thermal-ablation bioheat model including liquid-to-vapor phase change, pressure- and necrosis-dependent perfusion, and moisture-dependent properties," Int. J. Heat Mass Transf., vol. 50, no. 13-14, pp. 2537-2544, 2007.

[19]   J. Doss, "Claculations of electric fields in conductive media," Med phys, vol. 9, no. 4, pp. 566-73, 1982.

[20]   R. Bitsch, R. Rupp, L. Bernd and K. Ludwig, "Osteoid Osteoma in an ex Vivo Animal Model: Tempera-ture Changes in Surrounding Soft Tissue during CT-guided Radiofrequency Ablation," Rad, vol. 238, no. 1, pp. 107-112, 2006.

[21]   R. Irastorza, M. Trujillo, J. Villagrán and E. Berjano, "Radiofrequency Ablation of Osteoma Osteoide: A Finite Element Study," in VI Latin American Congress on Biomedical Engineering CLAIB 2014, Paraná, 2015.

[22]   M. Trujillo and E. Berjano, "Review of the mathematical functions used to model the temperature dependence of electrical and thermal conductivities of biological tissue in radiofrequency ablation," Int J Hyperthermia, vol. 29, no. 6, 2013.

[23]   D. Haemmerich and B. Wood, "Hepatic radiofrequency ablation at low frequencies," Int J Hyperther, vol. 22, pp. 563-574, 2006.

[24]   A. Logg, K.-A. Mardal, G. Wells and e. al., Automated Solution of Differential Equations by the Finite Element Method, Springer, 2012.

[25]   S. Hall, "MITA-model," 5 Feb 2016. [Online]. Available: https://github.com/sheldonkhall/MITA-model.

[26]   P. Hasgall, F. Gennaro, C. Baumgartner, E. Neufeld, B. Lloyd, M. Gosselin, D. Payne, A. Klingenböck and N. Kuster, "IT'IS Database for thermal and electromagnetic parameters of biological tissues," 15 May 2018. [Online]. Available: itis.swiss/database. [Accessed 09 09 2019].

[27]   S. Tungjitkusolmun, S. Staelin, D. Haemmerich, J. Tsai, H. Cao, J. Webster, F. Lee, D. Mahvi and V. Vorperian, "Three-dimensional finite-element analyses for radio-frequency hepatic tumor ablation," IEEE Trans Biomed Eng, vol. 49, pp. 3-9, 2002.

[28]   J. Gong, J. Arnold and S. Cohn, "Composition of Trabecular and Cortical Bone," Anat Rec, vol. 149, pp. 325-31, 1964.

[29]   H. Woodard and D. White, "The composition of body tissues," Br J Radiol, vol. 59, no. 708, pp. 1209-1219, 1986.

[30]   I. Lorenzo, M. Serra-Prat and J. Yébenes, "The Role of Water Homeostasis in Muscle Function: A Review," Nutrients, vol. 11, no. 8, p. 1857, 2019.

[31]   J. Pearce, "Comparative analysis of mathematical models of cell death and thermal damage processes," Int J Hyperther, vol. 29, no. 4, pp. 262-280, 2013.

[32]   C. Tillotson, A. Rosenberg and D. Rosenthal, "Controlled thermal injury of bone. Report of a percu-taneous technique using radiofrequency electrode and generator," Invest Radiol, vol. 24, no. 11, pp. 889-892, 1989.

[33]   R. Irastorza, M. Trujillo and E. Berjano, "How coagulation zone size is underestimated in computer modeling of RF ablation by ignoring the cooling phase just after RF power is switched off," Int J Numer Meth Biomed Engng, vol. 33, no. 11, p. e2869, 2017.

[34]   A. Rohatgi, WebPlotDigitizer, 4.4 ed., Pacifica, California, 2020.

[35]   S. Hall, E. Ooi and S. Payne, "Cell death, perfusion and electrical parameters are critical in models of hepatic radiofrequency ablation," Int J Hyperthermia, vol. 31, no. 5, pp. 538-50, 2015.

[36]   C. Pinto, A. Taminiau, G. Vanderschueren, P. Hogendoorn, J. Bloem and W. Obermann, "Technical Considerations in CT-Guided Radiofrequency Thermal Ablation of Osteoid Osteoma: Tricks of the Trade," AJR Am J Roentgenol, vol. 179, no. 6, pp. 1633-1642, 2002.

[37]   D. Schutt and D. Haemmerich, "Effects of variation in perfusion rates and of perfusion models in computational models of radio frequency tumor ablation," Med Phys, vol. 35, no. 8, pp. 3462-70, 2008.

[38]   S. Solazzo, Z. Lui, S. Lobo, M. Ahmed, A. Hines-Peralta, R. Lenkinski and S. Goldberg, "Radiofrequency Ablation: Importance of Background Tissue Electrical Conductivity—An Agar Phantom and Computer Modeling Study," Radiology, vol. 263, no. 2, pp. 495-502, 2005.

Chapter 3

Chapter 4

Modelling radiofrequency ablation of atypical cartilaginous tumors in long bones using finite element methods

Ricardo Rivas [a], Ludo J. Cornelissen [a], Thomas C. Kwee [b], Paul C. Jutte [c], Peter M. A. van Ooijen [a*]

[a] University of Groningen, University Medical Center Groningen, Department of Radiotherapy, Groningen, The Netherlands
[b] University of Groningen, University Medical Center Groningen, Department of Radiology, Groningen, The Netherlands
[c] University of Groningen, University Medical Center Groningen, Department of Orthopedics, Groningen, The Netherlands

Modelling radiofrequency ablation of atypical cartilaginous tumors in long bone using finite element methods

Abstract

Aim

To model radiofrequency ablation (RFA) of atypical cartilaginous tumors (ACT) in long bones using finite element modeling, and accurately predict ablation zone shape and extend.

Materials and methods

Imaging data from a clinical case of a patient with an ACT who was treated with RFA was used to model a typical case of RFA of ACT and to measure the extension of the post-procedural ablation zone. The finite element method was used to solve the equations governing the coupled thermal-electric problem defining RFA. To find the set of parameters that could best replicate the clinical data and to evaluate their influence on the outcome, a fractional factorial analysis with the Taguchi method was used. The results were analyzed with the main effects plot and ideal parameters were proposed and tested.

Results

The most important parameters defining the ablation zone size were the electrical conductivity of the target tumor and its surrounding tissue, the trabecular bone, followed by the blood perfusion of the trabecular bone. The proposed parameters and model produce ablation diameters of 38x43, being 5x1 mm shorter than the clinical case in the directions perpendicular and parallel to the electrode, respectively.

Conclusions

RFA of ATC can be reliably replicated with a computer model using the parameters found with our parametric analysis, which could potentially be used for more reliable patient-specific planning.

Introduction

Radiofrequency ablation (RFA) is a minimally invasive technique that has been widely used for the treatment of various types of tumors, such as tumors in liver [1], lungs [2], kidneys [3], or breast [4], and has been suggested as the treatment of choice for osteoid osteomas, a benign small bone lesion [5]. Although its application for bone tumors has been mostly limited to osteoid osteomas, advances have been made to treat other (larger) bone tumors such as atypical cartilaginous tumors [6], osteoblastoma [44], and chondroblastoma [8], while other studies have suggested the use of RFA for the treatment of recurrent bone and soft-tissue sarcomas in non-surgical candidates [9]. Although the technique of RFA seems to be safe and overall effective, with few complications and comorbidities [1] [2] [3] [4] [5], the extension of thermal damage remains poorly understood. As a result, interventionists' planning of RFA procedures in the bone currently relies on assumptions based on other types of tumors, tissues, and ablation procedures. Because it is known that differences in tissue composition and ablation time produce significantly different outcomes [10], these assumptions may not be adequate and lead to problems such as unsuccessful interventions or unintentional damage to other tissues.

Atypical cartilaginous tumors are among the most common types of bone tumors [11], located mostly in the long bones and pelvis, replacing marrow fat and trabecular bone with cartilaginous neoplastic tissue [12]. Because of the risk of local tumor progression, treatment consist of complete tumor removal, with intralesional curettage followed by local adjuvant treatment as the standard of care [13]. Because of its overall effectiveness and safety, RFA has great potential to replace invasive techniques in selected cases, as shown in a pilot study by our research group [6]. This study showed that the technique has the potential for better local tumor control while improving the functional outcome and allowing patients to return to their normal activities.

The main aim of RFA is complete tumor destruction while sparing as much healthy tissue as possible. As a solution, computer models to simulate the procedure and increase our understanding of how the thermal damage is induced and distributed over time have been developed, with the finite element method being one of the most popular methods to achieve this [14]. However, to the best of our knowledge, there have been no computer studies on RFA of tumors other than osteoid osteoma in the long bones. Given the current interest to expand the use of RFA to other types of bone tumors, such as atypical cartilaginous tumors and the lack of information regarding the expected outcomes in these cases, a computer model is crucial to improve our understanding of the procedure and be of use for accurate procedural planning thereby enhancing safety and efficacy. Effective local tumor control whilst minimizing damage for the patient is the holy grail in local tumor treatment. Therefore, the aim of this study is to develop a finite element model to accurately predict the ablation zone shape and extend of atypical cartilaginous tumors.

Chapter 4

Materials and methods

To model a typical procedure and find the best fitting parameters to replicate the resulting ablation zone, a representative standard case of an atypical cartilaginous tumor in the long bones that underwent RFA was chosen from a previous study [15]. After the procedure was optimized for this case, a second case (with a different anatomical configuration) was also tested to validate the accuracy of our model and parameters.

Model Geometry

A case of a centrally located tumor in the long bones was selected to use as a reference for the optimization. By using a centrally located tumor it was possible to assume an axis of symmetry along the electrode to simplify the model. The modeled tumor was assumed to be a perfect ellipsoid encased by trabecular bone, and then surrounded by a wall of cortical bone, followed by one more layer of muscle (Figure 2). The electrode was assumed to be inside the tumor just next to the interface with trabecular bone, with a little offset from the starting point of the tumor of 0.5 mm. The simulated electrode had the same length as the electrode used in the clinical cases selected, i.e., an electrode with a 2 cm active tip, with the rest of the electrode insulated by a thin layer of plastic. A mesh convergence analysis was done until a change of < 1% on the ablation zone diameters was found.
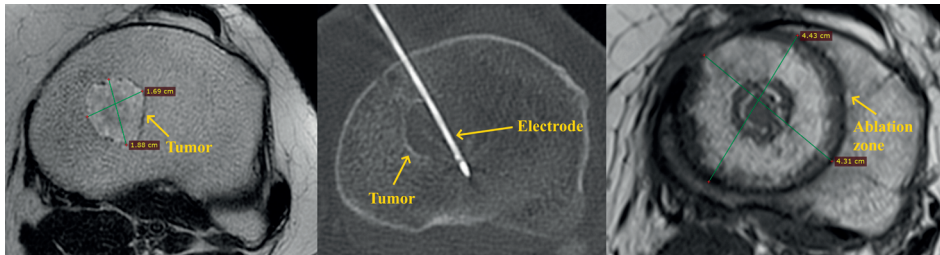
Figure 1 Pre-, intra-, and post-operative images of the representative clinical case used for the analysis. The tumor is poorly visible on the CT images given its low density, but it is easy to see on the MR images. Figure 1A shows the preoperative MR image of a cartilage tumor in a tibia metaphysis, where the tumor is visible within the trabecular bone. Figure 1B, intra-operative CT images of the same cartilage tumor, the RF electrode is seen entering from top left of the image. Figure 1C shows the post-procedural MR image with the resulting ablation zone after the RFA intervention. Here, the hypointense focus represents the ablated tumor, and the hypointense contours surrounding it represent the borders of the ablation zone. The corresponding resulting ablation diameters are indicated with caliper measurements.
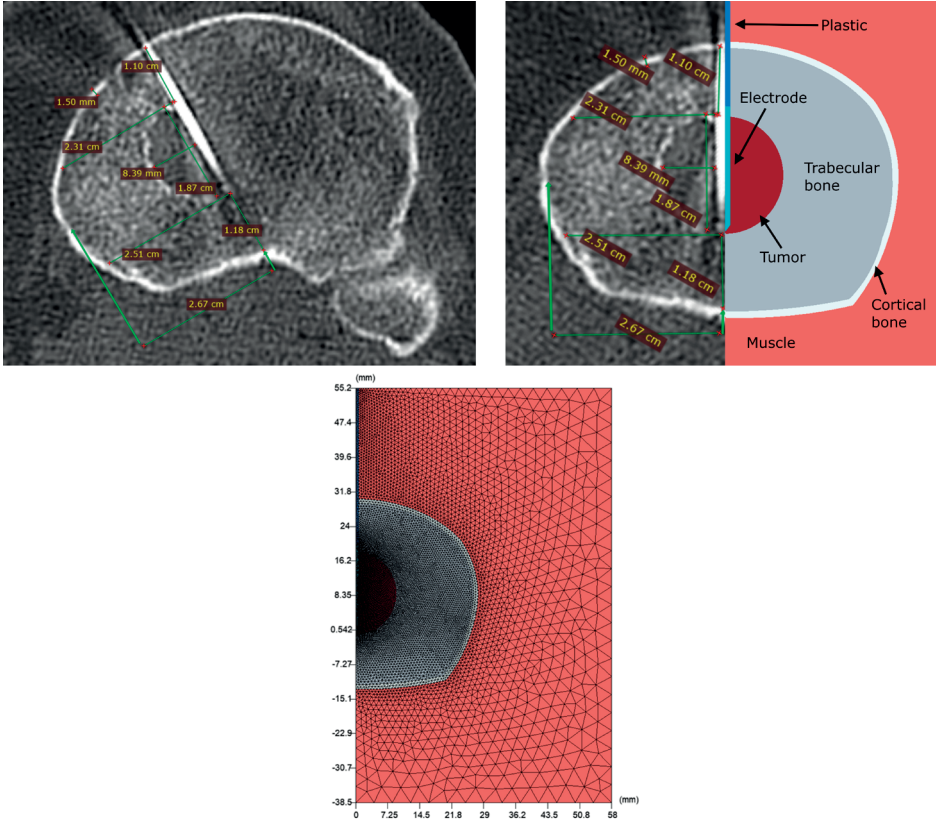
Figure 2 *The top images show the intraoperative CT image with measurements of the tumor (a round hypodense focus around the electrode) and its spacial relation to its surroundings and how the electrode was used as axis of symmetry for the resulting axisymmetric model. The contrast window was adjusted from the previous figure to more clearly highlight the cortical bone and tumor. The bottom image shows the meshing of the model, having smaller elements next to the electrode-tumor interface, where more resolution is needed because of the higher gradients of current and temperature at the electrode and because of its smaller size.*

Radiofrequency ablation procedure and clinical ablation zone

In the clinical case that was used for modelling, the ablation was performed using a non-cooled straight electrode with a self-regulating current to keep a pre-defined control temperature of 90°C, which is measured at the tip of the electrode to monitor and control the procedure. This temperature was maintained for approximately between 6 and 8 minutes at this control temperature. Our simulations lasted for 7 minutes, and a proportional-integral (PI) controller (as described in the following section) was used to control the output voltage based on the control temperature measured at the tip of the electrode, as in the clinical case.

The patient was evaluated two months after the procedure using MRI. A radiologist measured the resulting ablation diameter in two main axes, and these were then defined as our outcome of interest to be replicated. The perpendicular axes are similar in 2 dimensions, so with two axes a full 3D representation is guaranteed. The ablation zone in the simulations was obtained using a cell thermal damage model, the Arrhenius equation [16], which relates the amount of thermal damage through time to a given cell and calculates its viability, as described in the next section. The primary outcome of the simulation, in 2 dimensions, is then the diameter of the resulting ablation zone, i.e. the region in which cell viability is zero.

Equations governing radiofrequency ablation

The models consisted of solving a coupled electric-thermal problem, as defined by the Joule effect and Pennes' bioheat equation. For the generation of heat, an electrode supplies a voltage in the radiofrequency range ($\approx$ 500 kHz) which then heats up the nearby tissues. At this range, a quasi-static approach is used because the tissues can be considered as totally resistive, i.e., capacitive losses do not play a role in the heating [17]. The heat source, Q_{RF}, is thus given by:

$$Q_{RF} = \sigma_i |\mathbf{E}|^2 \tag{1}$$

Where σ_i is the electrical conductivity $\left(\frac{S}{m}\right)$ of each tissue and E is the electric field intensity $\left(\frac{V}{m}\right)$, where the electric problem is stated by the Laplace equation:

$$\nabla \cdot \sigma_i \nabla V = 0 \tag{2}$$

where V is the root mean squared value of the voltage (V) applied.

The voltage is regulated with a PI-controller where the aim is to reach and maintain a pre-defined temperature at the tip of the electrode for a certain amount of time, as in the clinical setting. The controlled can be modelled as:

$$V_{r.m.s.}(t) = K_p \left(T_{target} - T(t)\right) + K_i \int_0^\tau \left(T_{target} - T(t)\right) dt \tag{3}$$

where $V_{r.m.s.}$ is the r.m.s. voltage (V) set at the electrode boundary, and K_p and K_i are the error and integral proportionality constants of the PI-control, correspondingly. T_{target} is the target temperature and $T(t)$ the sampled temperature at the tip at time t. The PI-constants were chosen from the study by Irastorza et al. [18], who found a good agreement with these constants to an ex-vivo experiment of RFA in bone setting $K_p = 1.15 \left(\frac{V}{K}\right)$ and $K_i = 0.06 \left(\frac{V}{K \cdot s}\right)$.

The thermal problem is governed by Pennes' bioheat equation [19], with the apparent heat capacity method [20] to model tissue vaporization:

$$\rho c_{app}(T)\frac{\partial T}{\partial t} = \nabla \cdot (k_i(T)\nabla T) + Q_{RF} - Q_p \tag{4}$$

Where ρc_{app} is the apparent specific heat, as defined by the apparent heat capacity method [20], used to capture the sudden change in heat capacity during the phase-change from water to vapor, stated by the piecewise function in equation (14), where ρ corresponds to the density in $\left(\frac{Kg}{m^3}\right)$, and c to the specific heat in $\left(\frac{J}{kg \cdot K}\right)$. k_i is the thermal conductivity in $\left(\frac{W}{m \cdot K}\right)$ of each tissue, T is the temperature in (K), t is the time in (s) and Q_{RF} is the heat source in $\left(\frac{W}{m^3}\right)$. Q_P is the blood perfusion heat loss in $\left(\frac{W}{m^3}\right)$, defined in equation 6.

$$\rho c_{app}(T) = \begin{cases} \rho_i c_i, & T \leq 99\,°C \\ \dfrac{\left(\rho_i c_i + \rho_{vap} c_{vap}\right)}{2} + \rho_w L_w C, & 99°C < T \leq 100\,°C \\ \rho_{vap} c_{vap}, & T > 100\,°C \end{cases} \quad (5)$$

Where ρ_i in $\left(\frac{J}{kg}^3\right)$, and c_i in $\left(\frac{J}{kgK}\right)$, represent the baseline density and specific heat of each tissue, correspondingly. ρ_{vap} is the density of vapor and c_{vap} its specific heat. ρ_w is the density of water, L_w is the latent heat of vaporization of water in $\left(\frac{J}{kg}\right)$, and C is the water fraction.

The blood perfusion heat loss is given by:

$$Q_p = \omega_i(\Omega)\rho_b c_b[T - T_b] \quad (6)$$

where $\omega_i(\Omega)$ is the cell-death-dependent blood perfusion coefficient of each tissue, in (s^{-1}), which becomes zero when a given cell dies, as defined by the cell-death model. ρ_b is the density of blood in $\left(\frac{kg}{m^3}\right)$, c_b the specific heat of blood in $\left(\frac{J}{kg \cdot K}\right)$, T_b the temperature of blood in (K).

The electrical and thermal conductivity of biological tissues have a temperature-dependent behavior, which were modeled following Trujillo and Berjano [21], where a constant linear increase was considered until the point of vaporization.

To model the sudden drop in the electrical conductivity caused by tissue vaporization, the conductivity was modeled with a linear increase until the point of vaporization, as defined by:

$$\sigma(T) = \begin{cases} \sigma_0 + \Delta\sigma(T - 37\,°C), & T \leq 100\,°C \\ \sigma_{100°C} + \left(\sigma_{vap} - \sigma_{100°C}\right)\dfrac{(T - 100\,°C)}{5}, & 100°C < T \leq 105\,°C \\ \sigma_{vap}, & T > 105\,°C \end{cases} \quad (7)$$

The initial electrical conductivity at 37 °C of each tissue is given by σ_0 in $\left(\frac{S}{m}\right)$, with the linear rate of change in electrical conductivity per °C given by $\Delta\sigma = 0.015$. $\sigma_{100°C}$ is the tissues' conductivity at 100 °C, and σ_{vap} is the electrical conductivity of vaporized tissue $\sigma_{vap} = 1x10^{-4}\left(\frac{S}{m}\right)$.

A linear increase of 0.003 per was considered for the thermal conductivity until the point of vaporization, where a maximum value was set, as stated in:

$$k(T) = \begin{cases} k_0 + \Delta k(T - 37\ {}^\circ\text{C}), & T \leq 100\ {}^\circ\text{C} \\ k_0 + \Delta k(100\ {}^\circ\text{C} - 37\ {}^\circ\text{C}), & T > 100\ {}^\circ\text{C} \end{cases} \qquad (8)$$

where k_0 is the baseline thermal conductivity in $\left(\frac{W}{m \cdot K}\right)$ and Δk the rate of change in thermal conductivity per °C.

Boundary conditions

For the electric problem, a Dirichlet boundary condition at the electrode surface was set with a value equal to the applied r.m.s. voltage. A Dirichlet boundary condition of zero voltage was set at the outer boundaries to mimic the dispersive electrode. A Neumann boundary condition of zero flux was set at the symmetry axis. For the thermal problem, a Dirichlet boundary condition of a constant temperature of 37 °C to mimic the body temperature was set at the outer boundaries, and a Neumann boundary conduction of zero thermal flux was set at the symmetry axis.

An implementation on FEniCS [22], an open-source platform for finite element modelling, was used to model and solve the proposed model. The model was adapted from the work by Hall [23], who developed a platform to solve multiple minimally invasive tumor ablation therapy models using FEniCS.

Cell death model

The Arrhenius model [16] was used to assess the thermal damage in RFA, where the thermal damage to which a given cell is exposed is calculated over time using a first-order kinematics relationship, with higher temperatures and exposure times increasing the amount of damage, as defined by:

$$\Omega(\tau) = \int_0^\tau A e^{-\frac{\Delta E}{RT(t)}}\ dt, \qquad (9)$$

where A is a frequency factor, ΔE is the activation energy for the irreversible damage reaction, R is the universal gas constant, and T is temperature in (K). A and ΔE are cell-line dependent parameters which must be obtained experimentally. Values of $A = 8.99\ x\ 10^{133}\ s^{-1}$ and $\Delta E = 838 \frac{\text{kJ}}{\text{mol}}$, obtained from experiments on osteocytes [24], were chosen because the model is of bone tumors, and both cortical and trabecular bone have roughly the same susceptibility to heat [25].

Simulated ablation zone

The cell death model was used to calculate the thermal damage to cells, with a cell being considered dead once it reached a threshold of $\Omega = 4.6$, corresponding to a 99% chance of cell death [26]. The ablation radius was calculated across the modeled geometry starting at the electrode until the threshold was found. A cool-down phase after the active electrode was turned-off was allowed to more accurately capture the thermal damage over time, as shown by Irastorza et al. [27].

Tissue properties, tumor properties fitting, and the Taguchi orthogonal array

To study the effects of the tissue properties on the size of the ablation zone, and to capture the interpatient variability, minimum, average, and maximum values of each of the reported tissue properties were tested. Five variables with three levels for each of the tissues were thus defined. Focus of the tests were the properties of the tumor and the surrounding trabecular bone only, and the properties of cortical bone and muscle were kept at their average values. Additionally, since the actual tissue properties of the tumor have not been determined experimentally, but it is a cartilaginous tumor, the properties of cartilage were used as a baseline to then look for the best fitting parameters to replicate the clinical cases presented.

With these two main points in mind, the average, minimum, and maximum reported values of both cartilage and trabecular bone were tested. 10 variables (electrical conductivity, blood perfusion, density, heat capacity, and thermal conductivity, of both the tumor and the trabecular bone) with three levels (minimum, average, and maximum values) were thus defined. To avoid a full factorial analysis (requiring 3^{10} experiments), the Taguchi method, a fractional factorial method, was used. The Taguchi method uses an orthogonal array to reduce the number of parameter configurations by having the columns (parameters) mutually orthogonal, causing that, for any pair of columns, all combinations of factor levels occur, and to occur an equal number of times [28]. This allows to estimate main effects with just a few experimental runs when the right orthogonal array is utilized. With 10 variables and three levels, the Taguchi L27 orthogonal array, shown in Table 2, was used. All tissue properties were obtained from the IT'IS Foundation [29], except for the properties of the tumor, described in more detail below.

For the parameters of the tumor the following considerations were taken. Electrical conductivity has been shown to be one of the most important parameters as it directly drives the energy deposition, and both benign and malignant tumors have been found to have significantly higher electrical conductivities, sometimes more than twice as high than its healthy counterparts [30] [31] [32]. Thus, for the electrical conductivity of the tumor, the average value of cartilage at the radiofrequency range was chosen, with a value of 0.2 S/m, and the maximum value for the electrical conductivity was chosen to be twice as large as the one from healthy

cartilage. For completeness, we made its minimum value half of that of healthy tissue, but this was done arbitrarily.

In the case of the tumor's blood perfusion, only one study was found, reporting a perfusion of 5.83 s^{-1} [29]. Given that cartilage is considered a non-vascularized tissue, that tumors may induce angiogenesis and create blood vessels, we gave it two additional values: one of no perfusion at all ($0s^{-1}$), and one of 8.33 s^{-1}, just slightly higher than the reported value and the same as the maximum for cancellous bone. We encountered a similar problem defining the tumor density. The value of cartilage's density in literature was an average of 1099.50 (with two studies, reporting 1099 and 1100). Since both reported almost the same value, for completeness we added a minimum of 1050 and a maximum of 1150, which are small arbitrarily chosen deviations. For the specific heat capacity and thermal conductivity, the reported average, maximum, and minimum values for cartilage were used.

Table 2 L27 Orthogonal Array with all the different configurations of tissue properties tested. The M, A, and m correspond to the maximum, average, and minimum values of each parameter, respectively.

	Variables and levels									
Trial	**A**	**B**	**C**	**D**	**E**	**F**	**G**	**H**	**I**	**J**
1	M	M	M	M	M	M	M	M	M	M
2	M	M	M	M	A	A	A	A	A	A
3	M	M	M	M	m	m	m	m	m	m
4	M	A	A	A	M	M	M	A	A	A
5	M	A	A	A	A	A	A	m	m	m
6	M	A	A	A	m	m	m	M	M	M
7	M	m	m	m	M	M	M	m	m	m
8	M	m	m	m	A	A	A	M	M	M
9	M	m	m	m	m	m	m	A	A	A
10	A	M	A	m	M	A	m	M	A	m
11	A	M	A	m	A	m	M	A	m	M
12	A	M	A	m	m	M	A	m	M	A
13	A	A	m	M	M	A	m	A	m	M
14	A	A	m	M	A	m	M	m	M	A
15	A	A	m	M	m	M	A	M	A	m
16	A	m	M	A	M	A	m	m	M	A
17	A	m	M	A	A	m	M	M	A	m
18	A	m	M	A	m	M	A	A	m	M
19	m	M	m	A	M	m	A	M	m	A
20	m	M	m	A	A	M	m	A	M	m
21	m	M	m	A	m	A	M	m	A	M
22	m	A	M	m	M	m	A	A	M	m

Table 2 L27 Orthogonal Array with all the different configurations of tissue properties tested. The M, A, and m correspond to the maximum, average, and minimum values of each parameter, respectively. (continued)

Trial	Variables and levels									
	A	**B**	**C**	**D**	**E**	**F**	**G**	**H**	**I**	**J**
23	m	A	M	m	A	M	m	m	A	M
24	m	A	M	m	m	A	M	M	m	A
25	m	m	A	M	M	m	A	m	A	M
26	m	m	A	M	A	M	m	M	m	A
27	m	m	A	M	m	A	M	A	M	m

For all the other tissues, their average reported value was taken. In the case of the electrode, to simulate the thin layer of plastic insulating it beyond the active part, we defined the insulated part as having properties of the active electrode (nickel-titanium) but with the electrical conductivity of plastic. The properties of all tissues and materials are given in Table 5. All values were obtained from [29], except where indicated.

*Table 3 Table with the tissue properties of all tissues. All values were obtained from [29], except where indicated. The maximum (Max), minimum (Min), and average (Avg) values of the tumor and trabecular bone used for the sensitivity analysis are also indicated. a, corresponds to the values as described in [33], which are of a nickel-titanium electrode; b, correspond to the assumptions for the tumor values as described in the main text, and * corresponds to the electrical conductivity of plastic, also taken from [33].*

Material / tissue	Electrical conductivity (S/m)	Blood perfusion coefficient $(x10^{-3}s^{-1})$	Density (kg/m3)	Specific heat (J/kg · K)	Thermal conductivity (W/m/K)
Active electrode [a]	1.00E+08	0	6450[a]	840	18
Insulated part of the electrode [a]	1.00E-05 [a] *	0	6450	840	18
Tumor	Max: 0. [b] Avg: 02 Min: 0.1[b]	Max: 0.83 [b] Avg: 0.5 [b] Min:0.0 [b]	Max:1150 Avg: 1100 Min: 1050	Max: 3664 Avg: 3568 Min: 3500	Max: 0.518 Avg: 0.487 Min: 0.417
Trabecular bone	Max: 0.135 Avg: 0.0925 Min: 0.05	Max: 0.83 Avg: 0.5 Min: 0.167	Max: 1350 Avg: 1178.33 Min: 1080	Max: 2254 Avg: 2274 Min: 2060	Max: 0.36 Avg: 0.3125 Min: 0.29
Cortical bone	0.022	0.167	1908	1313	0.32
Muscle	0.446	.6167	1090	3421	0.49

Outcomes and optimization

The diameter of the ablation zone as indicated by the cell death threshold was measured in directions perpendicular to and parallel to the electrode and used as the outcome of interest. With the results from the L27 orthogonal array, a Main Effects plot was used to examine how each factor contributed to the ablation diameter and the results were presented using a centered mean to more easily compare the diameters in both directions. After identifying the

most influential properties and examining the results, an optimal configuration was chosen as to match as closely the clinical results.

Finally, to further test the chosen parameters, we tested them on a different case. The new case had a different geometry with a different size of tumor, bone, and with an active tip of 3 cm. All the considerations for the previous model were taken for this case, changing only the geometry and the ablation time. The ablation was simulated with an active heating time of 6 minutes, replicating what was reported in clinical practice, and a cooldown time was also allowed as described previously.

Results

The ablation radii of all the tested configurations are shown in Table 4.

Table 4 All the different configurations tested as based on the L27 orthogonal array with their respective resulting ablation diameters in the directions perpendicular and parallel to the electrode.

Test	Perpendicular Ablation diameter (mm)	Parallel ablation diameter (mm)
1	28.60	37.85
2	32.10	39.58
3	38.14	42.41
4	29.27	38.20
5	33.12	40.02
6	35.71	41.75
7	30.21	38.61
8	30.74	38.89
9	37.08	42.05
10	28.24	37.65
11	31.03	39.32
12	25.73	36.61
13	29.37	38.27
14	30.49	38.94
15	25.31	36.37
16	28.84	38.00
17	29.87	38.65
18	26.01	36.81
19	27.46	37.46
20	24.24	36.56
21	24.11	36.16
22	27.16	37.35

Table 4 All the different configurations tested as based on the L27 orthogonal array with their respective resulting ablation diameters in the directions perpendicular and parallel to the electrode. (continued)

Test	Perpendicular Ablation diameter (mm)	Parallel ablation diameter (mm)
23	24.64	36.81
24	23.86	36.09
25	27.88	37.76
26	24.40	36.68
27	23.78	36.02

For the perpendicular and parallel ablation diameters, the smallest ablation diameters were 23x35.6 mm for case number 27, and largest ablation diameters of 38x42.5mm for case number 3. The average ablation diameters were 28x38 mm, respectively.
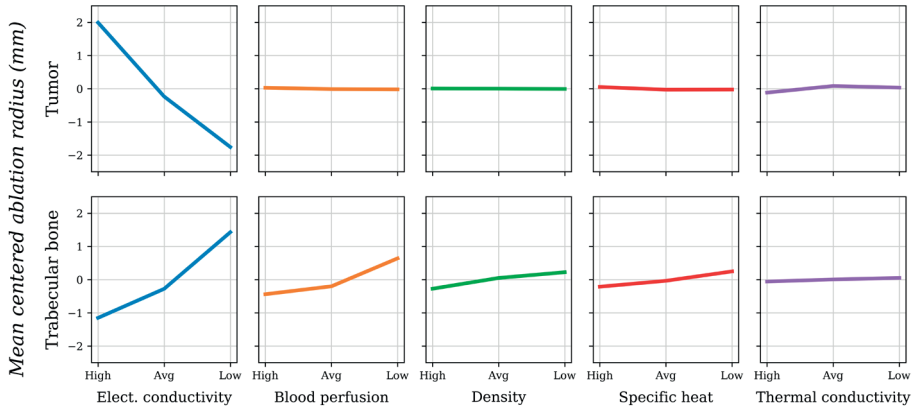

Figure 3 Main effects plot with a centered mean showing how each parameter and level influence the size of the ablation radius. Higher slopes indicate a higher difference on the results from one level to another. The analysis was performed in both radii, perpendicular and parallel to the electrode, with near identical results, and only the one in the perpendicular direction to the electrode is shown.

The main effects plot in Figure 3 shows the influence that each factor and level had on the ablation radius. The most influential factor was the electrical conductivity of both the tumor and the trabecular bone. The higher the electrical conductivity of the tumor, the larger the ablation radius. In contrast, a lower electrical conductivity from trabecular bone yields a larger ablation radius. Blood perfusion was the second most important parameter, but only in the case of trabecular bone, decreasing the ablation radius when its value was high, and increasing the ablation diameter when its value was low.

Looking at the results from the Taguchi experiments, the experiment that had the largest ablation diameters, of 38x42.5mm, was already close to the clinical case to replicate, with an

ablation diameter of 43x44 mm. Because of this, a first step towards optimizing the parameters to replicate the clinical case was then to choose the parameter-level configuration that could produce the largest ablation diameters by choosing the parameters that contributed the most to a large ablation zone, as larger diameters were still needed. The selection is shown in Table 5. Using the proposed set of tissue parameters, a resulting ablation zone of 38x43 mm was obtained, as shown in Figure 4. The chosen combination based on the main effects analysis

Table 5 Combination of parameters to maximize the ablation zone based on the main effects plot. The brackets indicate whether the parameter level was the maximum, average, or minimum value, from the range of values used.

	Elect. cond. $\left(\frac{S}{m}\right)$	Perf. $\left(\frac{1x10^{-3}}{s}\right)$	Density $\left(\frac{kg}{m^3}\right)$	Specific Heat $\left(\frac{J}{kg \cdot K}\right)$	Thrm. cond. $\left(\frac{W}{m \cdot K}\right)$
Tumor	0.4 [max]	0 [min]	1150 [max]	3664 [max]	0.487 [avg]
Trabecular bone	0.05 [min]	0.167 [min]	1080 [min]	2060 [min]	0.36 [max]

of parameters was just 0.5 mm larger than the case that yield the maximum results from the Taguchi array. It was also 5x1 mm shorter than the clinical case in the directions perpendicular and parallel to the electrode, respectively. Further tweaking the parameters to increase the perpendicular diameter always resulted in an increase in the parallel diameter, which meant an overestimation on the ablation zone size. An underestimation was deemed more acceptable and therefore the proposed tissue parameters were accepted as the optimal configuration.
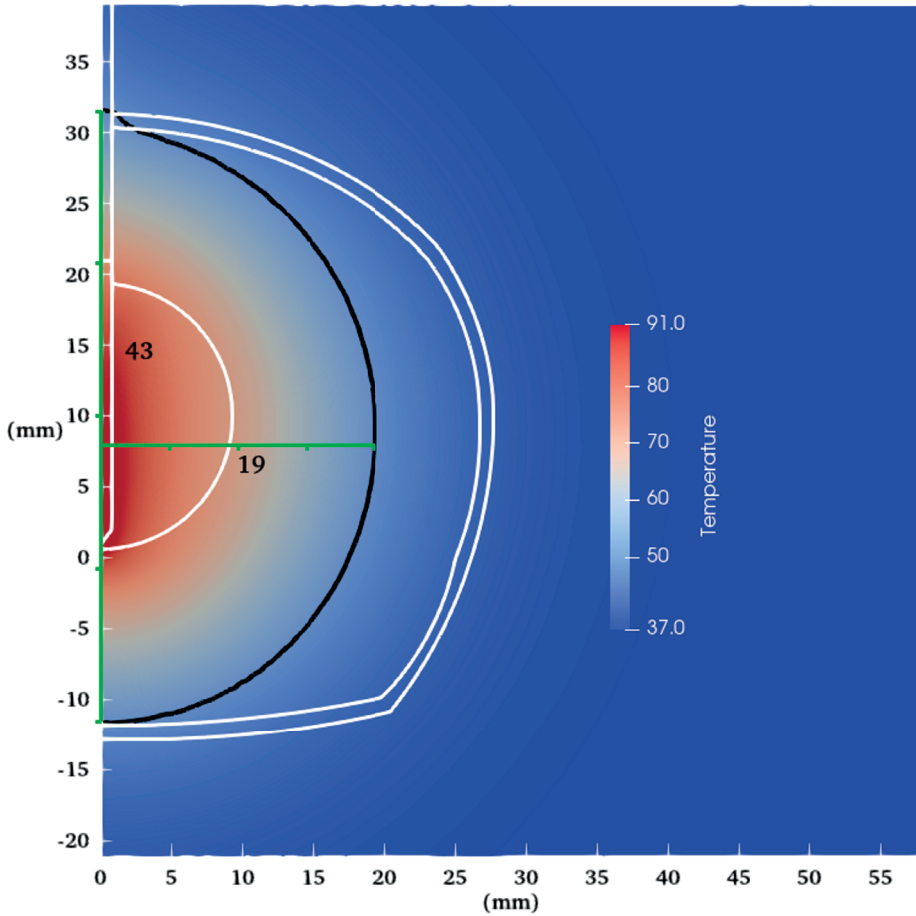
Figure 4 Resulting ablation zone with the proposed optimal. The ablation was simulated for a total of 7 minutes of active heating plus some additional minutes until the mesh cooled down, after which the cell death was calculated. The figure shows the temperature map just before the electrode is turned off and the contour of the cell death after cooldown.

In the second test of the best fitting parameters, using a model with a different geometry, the results of the simulations were an ablation zone of 33x49 mm, in contrast to the 31x48 mm ablation zone measured in clinical practice, shown in Figure 5.

Figure 5 Left: Intraoperative CT image showing the location of the electrode inside the patient. Center: Post-operative MRI showing the resulting ablation diameters. Right: Resulting ablation radius and diameter from the simulations; the geometry was adapted to replicate as best as possible the dimensions from the clinical cases. The simulation had a tim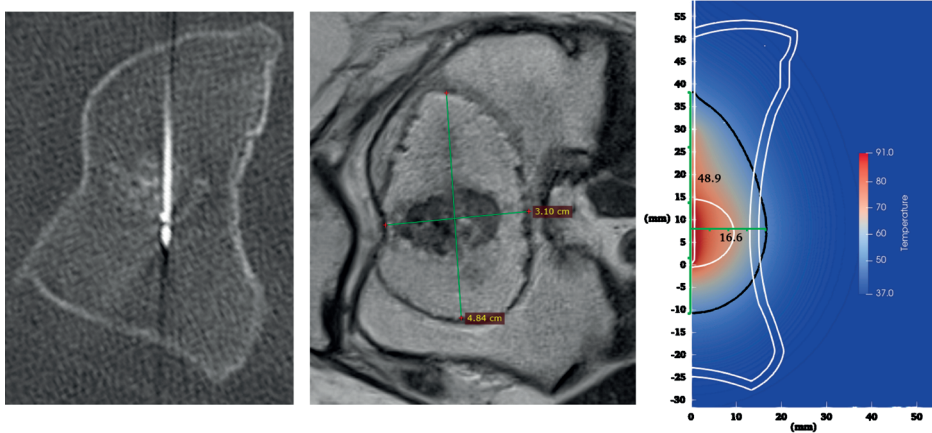e of active heating of 6 minutes, as in the clinical case, plus some additional minutes until the mesh cooled down, after which the cell death was calculated. The figure shows the temperature map just before the electrode is turned off and the contour of the cell death after cooldown.

Discussion

With the growing need for the use of minimally invasive procedures such as RFA in bone tumors (minimizing damage with maximal effect) but with the little information available regarding the extension of the ablation zones, interventionists are challenged with planning with limited knowledge. Incomplete local tumor control or unnecessary damage of healthy tissue (e.g., nerve damage, bone fracture) are common problems that could potentially be avoided if the resulting ablation zones could be planned more accurately. With the models and parameters presented here, a model of radiofrequency ablation of ACT able to replicate ablation results in clinical practice is possible. These findings represent an important step towards a better understanding of thermal damage in bone tumors and towards more complex patient specific models which are needed to help interventionists ensure safe and effective planning and procedures to guarantee successful treatment.

Several studies have already used models to simulate RFA in other tissues, such as liver, heart, cornea, etc., with most models based on the Finite Element Method [14]. Some models have modeled accurate geometrical representations of real human anatomy [34], showing that the resulting ablation zone differs considerably depending on the ablated tissue, and highlighting the importance of carefully choosing the right treatment time and applied voltage. So far, the only RFA model of bone tumors were on osteoid osteomas [35] [27], however this type of tumor is smaller than the ones here discussed, and is also characterized by having a thick

sclerotic layer or by usually being in cortical bone. In contrast, ACTs may be much larger, lack the sclerotic layer, and grow in trabecular bone. Thus, although both are models of bone tumors, there are important differences that justify the creation and validation of a model like the one here presented.

Because of the uncertainty on the parameters for the model, particularly the properties of the tumor, finding how each factor contributed to the outcome and finding a range of values for which the model worked was important. For that, the Taguchi orthogonal array was used to study the main effects of multiple parameters and levels with a minimal number of experiments, avoiding a full factorial design and analysis. With this, we tested how each of the factors contributed to the overall results and whether common assumptions of RFA in other tissues hold true for RFA of ACT. Blood perfusion of trabecular bone was an important factor determining the extension of the ablation zone. Low perfusion rates in the tissue surrounding the tumor allowed the heat to be dissipated at a slower rate, and thus causing more local damage and increasing the ablation zone, which in literature is known as the oven effect [36] [37]. Similarly, as observed in the main effects plot, if the tissue surrounding the tumor had a lower electrical conductivity than the target tissue, a strong peak of resistive heating is observed at the tissue-bone interface, which could potentially lead to higher temperatures further away from the electrode because of the additional heat generation further away from the electrode. This has been demonstrated in ablation of other tissues [38] [39], and in the ablation of osteoid osteomas [35], another type of bone tumor, and could explain why the ablation zones in bone tumors seem to grow larger than expected. Bone has a considerably lower electrical conductivity than soft tissues, which could cause this effect to be even greater for RFA of soft tissue-based tumors in bone, as was the case with the atypical cartilaginous tumors here studied. Furthermore, our simulations consisted of a tumor surrounded by trabecular bone, but this effect could be stronger in cases with a cortical wall next to the tumor, and it would be interesting to study its effects in a three-dimensional scenario when both cortical and trabecular bone are surrounding the tumor.

Although the reported value for the electrical conductivity of normal healthy cartilage is 0.2 S/m, our results seem to indicate that some of the parameters like the electrical conductivity of cartilaginous tumors may be much higher than that of healthy normal cartilage because the simulation that approximated the clinical cases best had an electrical conductivity of 0.4 S/m. However, this value was from a single study, and the value at the radiofrequency range was not measured but inferred based on a frequency response model. Additionally, there are various types of cartilage (i.e., hyaline, fibro and elastic) that may have different properties, and it is not clear how much these types would differ. On the other hand, this much higher electrical conductivity should not be a surprise, as it is known that tumors, both benign and malignant, have higher electrical conductivities than healthy tissue, even more than twice their healthy

counterparts [30] [31] [32] in some cases. A next step towards more accurate patient-specific modeling and planning would be to characterize the properties of the tumors to then use them in a model like ours. With the electrical conductivity being the parameter that causes the most change in the outcome and thus the most important to investigate.

One important shortcoming of this study is that the axisymmetric models described are not an exact representation of the clinical situation. If revolved around their axis, the models would represent a set of ellipsoidal box-like objects encasing one over the other. Nonetheless, the models seemed to be able to capture the phenomenon accurately enough. This may be because the heat generation and transfer occur mostly close to the electrode, and the dimensions of our model were able to capture these phenomena without changing its electrical and thermal distribution too much from the real cases. However, in cases with complex 3D structures, these models may not be able to accurately represent the extent of the ablation zone in all 3D distances and thus over- or under-estimate the results in certain directions. In these cases, a patient specific model or a more intricated 3D model may be a better solution. Using accurate patient specific 3D models has the drawback of being very computationally expensive and preprocessing the data for the models can be very time consuming. Furthermore, our model showed a good enough accuracy in models with both 2 and 3 cm active electrodes, which are the most frequently used for this kind of therapies. These models also had different geometrical shapes and ablation zone sizes, and in both cases the models resulted in accurate results that reflected the changes in the geometrical shapes of the models. Thus, a first approach with an axisymmetric model to have a first impression of what is possible and propose an adequate set of parameters is a great first step towards more complex representations and simulations, such as a patient-specific models using image segmentation from medical images to create the geometries.

Another shortcoming is that assumptions had to be made on the position of the electrode based on the CT. Although we had access to intraoperative CT images, the electrode may be further moved after the final CT scan was taken, and the available retrospective CT data may thus not show the actual final position of the electrode. We do not expect this deviation to be large, but it is not uncommon to make small adjustments to the position of the electrode if the machine is failing to reach the target temperature. Occasionally, the tissues may heat up to the point of vaporization in places far from the tip of the electrode, which regulates the energy deposition. This causes a sudden increase in the resistance and shuts down the machine. Interestingly, we observed a similar phenomenon in our simulations when we modeled the geometry with the tip of the electrode exactly at the tumor-bone interface. The problem was solved by positioning the electrode slightly deeper into the tumor. This is similar to what is seen in clinical practice, and points towards the importance of preoperative planning, which could be done with a model like this one.

This study showed that RFA of ATC could be reliably replicated with a computer model using the parameters found with our parametric analysis, which could potentially be used for more reliable patient specific planning.

References

[1] S. McDermott and D. A. Gervais, "Radiofrequency Ablation of Liver Tumors," Seminars in Interventional Radiology, vol. 30, no. 1, pp. 49-55, 2013.

[2] I. Bargellini, E. Bozzi, R. Cioni, B. Parentini and C. Bartolozzi, "Radiofrequency ablation of lung tumours," Insights into Imaging, vol. 2, pp. 567-576, 2011.

[3] M. J. Stone, A. M. Venkatesan, J. Locklin, P. Pinto, M. Linehan and B. J. Wood, "Radiofrequency Ablation of Renal Tumors," Techniques in Vascular and Interventional Radiology, vol. 10, no. 2, pp. 132-139, 2007.

[4] T. Ito, S. Oura, S. Nagamine, M. Takahashi, N. Yamamoto, N. Yamamichi, M. Earashi, H. Doihara, S. Imoto, S. Mitsuyama and K. Akazawa, "Radiofrequency Ablation of Breast Cancer: A Retrospective Study," Clinical Breast Cancer, vol. 18, no. 4, pp. 495-500, 2017.

[5] D. Motamedi, T. J. Learch, D. N. Ishimitsu, Motamedi¸Kambiz, M. D. Katz, E. W. Brien and L. Menendez, "Thermal Ablation of Osteoid Osteoma: Overview and Stepby-Step Guide," RadioGraphics , vol. 29, no. 7, pp. 2127-2141, 2009.

[6] E. F. Dierselhuis, P. J. M. van den Eerden, H. J. Hoekstra, S. K. Bulstra, A. J. H. Suurmeijer and P. C. Jutte, "Radiofrequency ablation in the treatment of cartilaginous lesions in the long bones: results of a pilot study," The Bone & Joint Journal, Vols. 96-B, no. 11, pp. 1540-1545, 2014.

[7] C. Rehnitz, S. D. Sprengel, B. Lehner, K. Ludwig, G. Omlor, C. Merle, H.-U. Kauczor, V. Ewerbeck and M.-A. Weber, "CT-guided radiofrequency ablation of osteoid osteoma and osteoblastoma: Clinical success and long-term follow up in 77 patients," European Journal of Radiology, vol. 81, no. 11, pp. 3426-3434, 2012.

[8] C. Xie, L. Jeys and S. L. James, "Radiofrequency ablation of chondroblastoma: long-term clinical and imaging outcomes," European Radiology , vol. 25, no. 4, pp. 1127-1134, 2015.

[9] K. Yamakado, A. Matsumine, T. Nakamura, A. Nakatsuka, H. Takaki, T. Matsubara, K. Asanuma, A. Sudo, Y. Sugimura and H. Sakuma, "Radiofrequency ablation for the treatment of recurrent bone and soft-tissue sarcomas in non-surgical candidates," International Journal of Clinical Oncology, vol. 19, no. 5, pp. 955-962, 2014.

[10] P. Mertyna, A. Hines-Peralta, Z. Liu, E. Halpern, W. Goldberg and S. Goldberg, "Radiofrequency Ablation: Variability in Heat Sensitivity in Tumors and Tissues," J Vasc Interv Radiol, vol. 18, no. 5, pp. 647-654, 2007.

[11] T. Damron, W. Ward and A. Stewart, "Osteosarcoma, chondrosarcoma, and Ewing's sarcoma: national cancer data base report," Clin Orthop Relat Res, vol. 459, pp. 40-47, 2007.

[12] R. Marco, S. Gitelis, G. Brebach and J. Healey, "Cartilage tumors: evaluation and treatment.," J Am Acad Orthop Surg, vol. 8, no. 5, pp. 292-304, 2000.

[13] H. Gelderblom, P. Hogendoorn, S. Dijkstra, C. van Rijswijk, A. Krol, A. Taminiau and J. Bovée, "The clinical approach towards chondrosarcoma," Oncologist, vol. 13, no. 3, pp. 320-329, 2008.

[14] E. Berjano, "Theoretical modeling for radiofrequency ablation: state-of-the-art and challenges for the future," Biomed Eng Online, vol. 5, no. 24, 2006.

[15] R. Rivas, J. Overbosch, T. Kwee, J. Kraeima, R. Dierckx, P. Jutte and P. van Ooijen, "Radiofrequency ablation of atypical cartilaginous tumors in long bones: a retrospective study," Int J Hyperthermia, vol. 36, no. 1, pp. 1189-1195, 2019.

[16] J. Pearce, "Comparative analysis of mathematical models of cell death and thermal damage processes," Int J Hyperther, vol. 29, no. 4, pp. 262-280, 2013.

[17] J. Doss, "Claculations of electric fields in conductive media," Med phys, vol. 9, no. 4, pp. 566-73, 1982.

[18]   R. Irastorza, M. Trujillo, J. Villagrán and E. Berjano, "Radiofrequency Ablation of Osteoma Osteoide: A Finite Element Study," IFMBE Proc, vol. 49, pp. 858-862, 2015.

[19]   H. Pennes, "Analysis of tissue and arterial blood temperatures in the resting human forearm," Applied physiology, vol. 1, no. 2, pp. 93-122, 1948.

[20]   H. Hu and A. Argyropoulos, "Mathematical modelling of solidification and melting: a review," Model Simul Mat Sci Eng, vol. 4, no. 4, p. 371, 1996.

[21]   M. Trujillo and E. Berjano, "Review of the mathematical functions used to model the temperature dependence of electrical and thermal conductivities of biological tissue in radiofrequency ablation," Int J Hyperthermia, vol. 29, no. 6, 2013.

[22]   A. Logg, K.-A. Mardal, G. Wells and e. al., Automated Solution of Differential Equations by the Finite Element Method, Springer, 2012.

[23]   S. Hall, "MITA-model," 5 Feb 2016. [Online]. Available: https://github.com/sheldonkhall/MITA-model.

[24]   K. Kurata, J. Matsushita, A. Furuno, J. Fujino and H. Takamatsu, "Assessment of Thermal Damage in Total Knee Arthroplasty Using anOsteocyte Injury Model," J ORTHOP RES, vol. 35, no. 12, pp. 2799-2807, 2017.

[25]   C. Tillotson, A. Rosenberg and D. Rosenthal, "Controlled thermal injury of bone. Report of a percutaneous technique using radiofrequency electrode and generator," Invest Radiol, vol. 24, no. 11, pp. 889-892, 1989.

[26]   I. Chang and U. Nguyen, "Thermal modeling of lesion growth with radiofrequency ablation devices," BioMed Eng OnLine, vol. 3, no. 27, 2004.

[27]   R. Irastorza, M. Trujillo and E. Berjano, "How coagulation zone size is underestimated in computer modeling of RF ablation by ignoring the cooling phase just after RF power is switched off," Int J Numer Meth Biomed Engng, vol. 33, no. 11, p. e2869, 2017.

[28]   R. Kacker, E. Lagergren and J. Filliben, "Taguchi's Orthogonal Arrays Are Classical Designs of Experiments," J Res Natl Inst Stand Technol, vol. 96, no. 5, pp. 577-591, 1991.

[29]   P. Hasgall, F. Gennaro, C. Baumgartner, E. Neufeld, B. Lloyd, M. Gosselin, D. Payne, A. Klingenböck and N. Kuster, "IT'IS Database for thermal and electromagnetic parameters of biological tissues," 15 May 2018. [Online]. Available: itis.swiss/database. [Accessed 09 09 2019].

[30]   S. Laufer, A. Ivorra, V. Reuter, B. Rubinsky and S. Solomon, "Electrical impedance characterization of normal and cancerous human hepatic tissue," Physiol. Meas., vol. 31, pp. 995-1009, 2010.

[31]   H. Fricke and S. Morse, "The electric capacity of tumours of the breast," J. Cancer Res, vol. 10, pp. 340-76, 1926.

[32]   E. Burdette, J. Seals, S. Auda, A. Ambhire and R. Magin, "Review of the Dielectric Properties of Animal and Human Tumors Determined from In Vivo Measurements," Crit Rev Biomed Eng, vol. 44, no. 4, pp. 293-318, 2016.

[33]   S. Tungjitkusolmun, S. Staelin, D. Haemmerich, J. Tsai, H. Cao, J. Webster, F. Lee, D. Mahvi and V. Vorperian, "Three-dimensional finite-element analyses for radio-frequency hepatic tumor ablation," IEEE Trans Biomed Eng, vol. 49, pp. 3-9, 2002.

[34]   G. Zorbas and T. Samaras, "Simulation of radiofrequency ablation in real human anatomy," Int J Hypertherm, vol. 30, no. 8, pp. 570-578, 2014.

[35]   R. Irastorza, M. Trujillo, J. Martel Villagrán and E. Berjano, "Computer modelling of RF ablation in cortical osteoid osteoma: assessment of the insulating effect of the reactive zone," Int J Hyperthermia, vol. 32, no. 3, pp. 221-30, 2016.

Chapter 4

[36]   T. Livraghi, S. Goldberg, F. Meloni, L. Solbiati and G. Gazelle, "Hepatocellular carcinoma: Comparison of efficacy between percutaneous ethanol instillation and radiofrequency," Radiology , vol. 210, pp. 655-661, 1999.

[37]   D. Schutt and D. Haemmerich, "Effects of variation in perfusion rates and of perfusion models in computational models of radio frequency tumor ablation," Med Phys, vol. 35, no. 8, pp. 3462-70, 2008.

[38]   S. Solazzo, Z. Lui, S. Lobo, M. Ahmed, A. Hines-Peralta, R. Lenkinski and S. Goldberg, "Radiofrequency Ablation: Importance of Background Tissue Electrical Conductivity—An Agar Phantom and Computer Modeling Study," Radiology, vol. 263, no. 2, pp. 495-502, 2005.

[39]   M. Eckmann, M. Martinez, S. Lindauer, A. Khan and S. Ramamurthy, "Radiofrequency Ablation Near the Bone-Muscle Interface Alters Soft Tissue Lesion Dimensions," Reg Anesth Pain Med, vol. 40, pp. 270-275, 2015.

Chapter 5

Computer 3D modelling of radiofrequency ablation of atypical cartilaginous tumors in long bones using finite element methods and real patient anatomy

Ricardo Rivas [a*], Paul C. Jutte [b], Thomas C. Kwee [c], Peter M. A. van Ooijen [a]

[a] University of Groningen, University Medical Center Groningen, Department of Radiotherapy, Groningen, The Netherlands
[d] University of Groningen, University Medical Center Groningen, Department of Orthopedics, Groningen, The Netherlands
[c] University of Groningen, University Medical Center Groningen, Department of Radiology, Groningen, The Netherlands

Computer 3D modelling of radiofrequency ablation of atypical cartilaginous tumours in long bones using finite element methods and real patient anatomy

Original article

Abstract

Background: Radiofrequency ablation (RFA) is a minimally invasive technique used for the treatment of neoplasms, with a growing interest in the treatment of bone tumours. However, the lack of data concerning the size of the resulting ablation zones in RFA of bone tumours makes prospective planning challenging, needed for safe and effective treatment.

Methods: Using retrospective computed tomography and magnetic resonance imaging data from patients treated with RFA of atypical cartilaginous tumours (ACTs), the bone, tumour, and final position of the RFA electrode were segmented from the medical images and used in finite element models to simulate RFA. Tissue parameters were optimized, and boundaries conditions were defined to mimic the clinical scenario. The resulting ablation diameters from post-operative images were then measured and compared to the ones from the simulations, and the error between them calculated.

Results: Seven cases had all the information required to create the finite element models. The resulting median error (in all three directions) was -1 mm, with interquartile ranges from -3 to 3 mm. The three-dimensional models showed that the thermal damage concentrates close to the cortical wall in the first minutes and then becomes more evenly distributed.

Conclusions: Computer simulations can predict the ablation diameters with acceptable accuracy and may thus be utilized for patient planning. This could allow interventional radiologists to accurately define the time, electrode length, and position required to treat ACTs with RFA and make adjustments as needed to guarantee total tumour destruction while sparing as much healthy tissue as possible.

Keywords (MESH terms)**:** Bone neoplasms, Bone and Bones, Catheter ablation (radiofrequency), Computer simulation, Finite element analysis

Key points
- Radiofrequency ablation is a technique with great potential to treat bone neoplasms.
- There is, however, little information regarding the expected outcomes, making planning challenging.
- Computer models using the finite element method could be used to simulate the interventions.
- Computer simulations could help planning safe and effective interventions.

Declarations
Ethics approval and consent to participate

Only patients that agreed and signed a written form at the time of the intervention about the potential use of their anonymized data for scientific research were included in the study. No additional written or verbal consent was necessary, which is in accordance with the regulations of the Medical Ethical Review Board of our institution.

Chapter 5

Background

Radiofrequency ablation (RFA) is a minimally invasive technique that has been commonly used for the treatment of neoplasms in liver, kidney, adrenal glands, bone, lung, and breast [1]. Its use for the treatment of bone tumours has been mostly focused on osteoid osteoma, but there has been an interest in the treatment of other types of bone tumours, particularly the ones in the benign spectrum, such as chondroblastoma [2] [3] [4] [5] [6] and osteoblastoma [7] [8] [9], but also atypical cartilaginous tumours (ACTs) [10] [11]. Due to its minimally invasiveness, in contrast to more aggressive treatments such as open surgery, it allows for shorter recovery times, targeted tumour destruction, and low complication rates [12].

To guarantee optimal treatment, i.e., total tumour destruction while minimizing damage to healthy tissue [1], it is important to know the extension of the ablation zone. There is, however, little to no data concerning the size of the ablation zone for RFA of bone tumours, particularly for tumours other and larger than osteoid osteoma (*i.e.*, > 2 cm). Given the interest of our research group to expand the use of RFA from osteoid osteoma to other tumours such as ACTs, accurate and reliable planning are needed to guarantee safe and effective tumour ablations. In a previous initial study by our team in patients with an ACT in which the resulting ablation diameters after RFA treatment were measured, it was observed that the ablation zones grew larger than expected, particularly in contrast to those after RFA in other tissues, such as the liver and kidney [11]. Similar findings were observed by Neeman et al. [13], who performed RFA of a chordoma and suggested the larger than expected ablation volume may be due to the high-water content of the tumour and its relatively poor vascularity, resulting in higher electrical and thermal conductivities than that of liver or kidney tissue.

To further understand the effects of the bone and tumour tissue on the resulting ablation zone, a previous and yet to be published study by our research group used computer models with the finite element method (FEM) to simulate RFA of ACT. The implementation used a simplified two-dimensional (2D) geometry of the patient and a fractional factorial analysis to determine optimal parameters to replicate clinical cases with the computer model. These models had limitations, as they did not take into account the full three-dimensional (3D) characteristics of the anatomic location of interest. To further test the validity of these assumptions and in an attempt to develop an accurate patient-specific planning system for clinical use in RFA of ACTs, this study aimed to develop 3D models of the patient's anatomy and test the computational model's accuracy in replicating the ablation zones seen in clinical practice.

Methods

This study consisted of the following steps:

1) collection, segmentation, and manual registration of preprocedural and intraprocedural images of cases of ACT that were treated with RFA;
2) collection of the relevant clinical parameters of the intervention, such as size of the active RFA electrode (either 2 or 3 cm long) and the amount of time the energy was applied;
3) generation of standard triangle language (STL) files from the segmented images which were then transformed into 3D meshes;
4) application of a FEM utilizing the 3D patient-specific models from patient data;
5) measurement of the ablation diameters on post-RFA magnetic resonance (MR) images and the computer models.

Image segmentation and registration

Cases from a previous study [11] of patients that had undergone computed tomography (CT)-guided RFA of ACT were used to create the patient-specific meshes. Only patients that agreed and signed a written form at the time of the intervention about the potential use of their anonymized data for scientific research were included in the study. Only cases in which it was possible to determine the final position of the RFA electrode from the intra-procedural CT images and in which it was possible to properly segment the tumour and surrounding bone were chosen. The pre-RFA MR images (were used to segment the tumour, because tumour boundaries are usually not clearly visible on CT. The MR images were acquired using a 1.5 T MRI scanner (Siemens, Erlangen, Germany) with a surface coil. Fat-supressed Short Tau Inversion Recovery (STIR) T2-weighted sequences (TR/TE/TI: 8270/160/19 ms, 4 mm slice thickness) and T1-weighted images (TR/TE: 500/19 ms, 4 mm slice thickness) were acquired before and after the administration of an intravenous gadolinium-based contrast agent (0.1 mmol gadoterate meglumine (Dotarem®; Guerbet) per kg of body weight). As part of the routine MRI protocol, the images were acquired in two planes (transversal and either coronal or sagittal). The intraprocedural CT images (Somaton Definition AS, Siemens Medical Systems, Erlangen, Germany; 100 kVp, 49 mAs, 0.8 mm pitch) were used to segment the bones and the electrode.

All segmentations were done with Materialise Mimics (https://www.materialise.com) by the first author and later assessed by a musculoskeletal radiologist to confirm their accuracy. The segmentations were exported to STL format and Gmsh [14] (https://gmsh.info), a 3D finite element mesh generator, was used to generate the 3D meshes using the STL files. Because of the artifacts caused by the electrode on the CT data, the segmented electrode was only used to find the location of the electrode and then it was replaced by a modelled electrode, generated on Gmsh, replicating its dimensions. Gmsh was also used to create a mesh for the muscle

tissue, which was assumed as a large cube surrounding cortical bone. The surface of trabecular bone was determined by applying an offset of -2.5 mm on the surface of the segmented cortical bone.

Using MeshLab [15] (https://www.meshlab.net), meshes of multiple characteristic lengths were created and a mesh convergence analysis was done for each of the models, with the electrode having the smallest triangles (0.1–0.25 mm) and the muscles having much larger triangles. With Autodesk Meshmixer (http://www.meshmixer.com), manual refinement and reduction of triangles was performed, reducing the triangles in sections of bone far away from the electrode and increasing them close to the tumour and electrode. All models were defeatured, removing fine details to reduce the tetrahedron needed and thus also reduce the computational requirements.

Clinical parameters

The radiologist who performed the RFA registered the amount of time with the electrode at the desired target temperature of 90 °C and also indicated the amount of time with the applicator at a temperature higher than 60 °C. The length of the active electrode used during each intervention was also registered, which was either 2 or 3 cm.

A musculoskeletal radiologist with ten years of experience measured the ablation diameters in three orthogonal directions on the post-RFA MR images (same sequences used before RFA) that were acquired three months after the intervention. The results from the simulations were measured by the first author, with five years of experience in image processing, and who ran the computer simulations. The results were measured in three orthogonal directions as to match the measurements by the radiologist, and both results were compared. Note that the first author was blinded to the radiologist's measurements, and vice versa. The measurements were labelled as "longest", "shortest", and "other" ablation diameters, with the longest diameter being the diameter along the electrode axis and the other two orthogonal to it.

Finite element model

To determine the thermal damage over time of RFA of ACT with a non-cooled temperature-controlled ablation protocol with a control temperature of 90 °C, finite element models were created, in line with a previous, yet to be published, study from our research group. The implementation was done in FEniCS, a solver for finite element problems [16].

Equations governing radiofrequency ablation

In RFA, an alternating current of approximately 500 kHz is applied with an electrode into a target tissue. The current induces heating in the tissues surrounding the electrode, causing thermal damage to cells exposed to high temperatures. To simulate RFA, a coupled electric-thermal

problem has then to be solved, where tissue heating is due to Joule heating. Additionally, since the thermal damage is also dependent on the time exposed to a given temperature, a cell death model has to be utilized to relate temperature, time, and the robustness of the tissues to thermal damage.

For the electrical problem, a quasi-static approach can be taken, as the tissues can be seen as totally resistive to the current in the RF range [17]. The heat source, Q_{RF}, is given by:

$$Q_{RF} = \sigma_i(T)|\mathbf{E}|^2 \tag{1}$$

where σ_i is the temperature dependent electrical conductivity (S/m) of each tissue and $\mathbf{E}$ is the electric field intensity in (V/m), which is then defined by the Laplace equation, where V is the root mean squared value of the applied voltage V:

$$\nabla \cdot \sigma_i(T)\nabla V = 0 \tag{2}$$

The RFA procedure used for these patients was a temperature-controlled procedure, in which the voltage is automatically regulated by the RFA machine to maintain a predefined target control temperature, set by the interventional radiologist. To mimic that, a proportional-integral controller can be used, defining the root mean square (RMS) voltage (V) applied at the electrode boundary, V_{RMS}, as:

$$V_{RMS.} = K_p\big(T_{target} - T(t)\big) + K_i \int_0^\tau \big(T_{target} - T(t)\big)\ dt \tag{3}$$

For the controller, the initial voltage is set to zero, and then modulated as a function of the difference between the target temperature T_{target} and the temperature at the electrode's tip $T(t)$ at the time t, the error proportionally constant K_p, and the integral proportionality constant K_i. These constants are model dependent, but values of $K_{p'} = 1.15$ V/K and $K_i = 0.06$ V/K/s have been found to be a good approximation for ex-vivo bone RFA [18].

The temperature dependent properties of the electrical conductivity can be modelled with a piece-wise function [19]. First, there is a linear increase of 1.5%/°C until the point of tissue vaporization, where then a sudden drop in the electrical conductivity occurs, defined as:

$$\sigma_i(T) = \begin{cases} \sigma_i + \Delta\sigma_i(T - 37\ ^\circ C), & T \leq 100\ ^\circ C \quad (4) \\ \sigma_{100^\circ C} + \big(\sigma_{vap} - \sigma_{100^\circ C}\big)\dfrac{(T - 100\ ^\circ C)}{5}, & 100^\circ C < T \leq 105\ ^\circ C \\ \sigma_{vap}, & T > 105\ ^\circ C \end{cases}$$

where $\Delta\sigma_i$ corresponds to the 1.5% linear increase in the electrical conductivity per °C from the baseline electrical conductivity, σ_i, at 37 °C. σ_{vap} is the electrical conductivity of vaporized tissue, with a value of $\sigma_{vap} = 10x10^{-3}$ (S/m) [19].

The thermal problem is governed by Penne's bioheat equation [20], which is a modified version of the heat equation. If tissues get close to the boiling point, tissue vaporization occurs, which has important effects on both the electrical and thermal problems. Additionally, to account for the phase change into vapor, the enthalpy method [21] is utilized:

$$\frac{\partial h}{\partial t} = \nabla \cdot (k_i(T)\nabla T) + Q_{RF} - Q_p \tag{5}$$

where h is the enthalpy, which is a piece-wise function that relates the density and specific heat to temperature and accounts for phase change at high temperatures, k_i is the temperature dependent thermal conductivity (W/m·K), T is the temperature, Q_{RF} the heat source (W/m^3), and Q_p is the blood perfusion heat loss (W/m^3), defined as:

$$Q_p = \omega_i(\Omega)\rho_b c_b[T - T_b] \tag{6}$$

where ω_i is a tissue-dependent perfusion coefficient (s^{-1}) that depends on the cell viability Ω, from the cell death model, and indicates whether a cell is alive (with blood perfusion) or death (without blood perfusion). ρ_b is the density of blood (kg/m^3), c_b the specific heat of blood (J/kg·K), and T_b the temperature of blood (K).

To account for the temperature dependency of the heat capacity, a linear increase is first considered, followed by a sudden change in heat capacity at boiling temperatures, modelled using the enthalpy method [21] [19]:

$$h = \begin{cases} \rho_i c_i(T - 37°C), & 37\,°C \leq\ T \leq 99\,°C \\ h(99) + h_{fg}C_i \frac{(T-99°C)}{(100°C-99°C)}, & 99°C < T\ \leq\ 100\,°C \\ h(100) + \rho_{vap}c_{vap}(T - 100°C), & T > 100\,°C \end{cases} \tag{7}$$

where $\rho_i c_i$ are the baseline values of density ($\frac{kg}{m^3}$) and specific heat ($\frac{J}{kgK}$) of each tissue, h_{fg} is the latent heat of vaporization (2.25x10^6 $\frac{J}{kg}$), C_i is the water fraction of each tissue, and ρ_{vap}(370 $\frac{kg}{m^3}$) and c_{vap} (2156 $\frac{J}{kgK}$) are the density and specific heat of vaporized tissue [19].

For the temperature dependence of the thermal conductivity, k_i , of each tissue, a linear increase (Δk_i) of 0.33% per degree Celsius was considered until the point of vaporization, at which a maximum value was set [22] [23], as defined by:

$$k_i(T) = \begin{cases} k_i + \Delta k_i(T - 37\,°C), & T \leq 100\,°C \\ k_i + \Delta k_i(100\,°C - 37\,°C), & T > 100\,°C \end{cases} \tag{8}$$

Finally, for the cell viability Ω, relating the robustness of each tissue to thermal damage, the temperature, and exposure time, the Arrhenius damage model [24] was utilized:

$$\Omega(t) = \int_0^t A e^{-\frac{\Delta E}{RT(\tau)}}\, d\tau, \tag{9}$$

where A, a frequency factor, and ΔE, the activation energy for irreversible damage reaction, are cell-line dependent parameters, and R is the universal gas constant. Because most of the thermal damage occurs in bone, osteocytes were chosen for the cell-line parameters, with values of $A = 8.99 \: x \: 10^{133} s^{-1}$ and $\Delta E = 838$ kJ/mol. [25]. Additionally, to assess the thermal damage and measure the extension of the ablation zone, a value of $\Omega = 4.6$, corresponding to a 99% probability of cell death, was chosen as threshold, which was also the threshold to stop blood perfusion in equation (**6**).

Boundary conditions

A Dirichlet boundary condition [26] corresponding to the body temperature (37 °C) and one of zero voltage corresponding to the grounding pad were set at the outer boundaries of muscle tissue for the thermal problem and electrical problems, respectively. At the electrode surface, a Dirichlet boundary condition equal to the applied RMS voltage was also set, which varies on time as defined by the proportional-integral controller. At the bottom side of the electrode, however, a Neumann boundary condition of zero was set for both the thermal and electrical problems, as that side is, in practice, part of a larger insulated piece with no heat or electrical flux. The insulated section of the electrode, which comes from the outside of the patient to the target site, was not modelled to simplify the 3D meshes. A cross section of one of the resulting meshes and the different tissues is shown in Fig. 1.
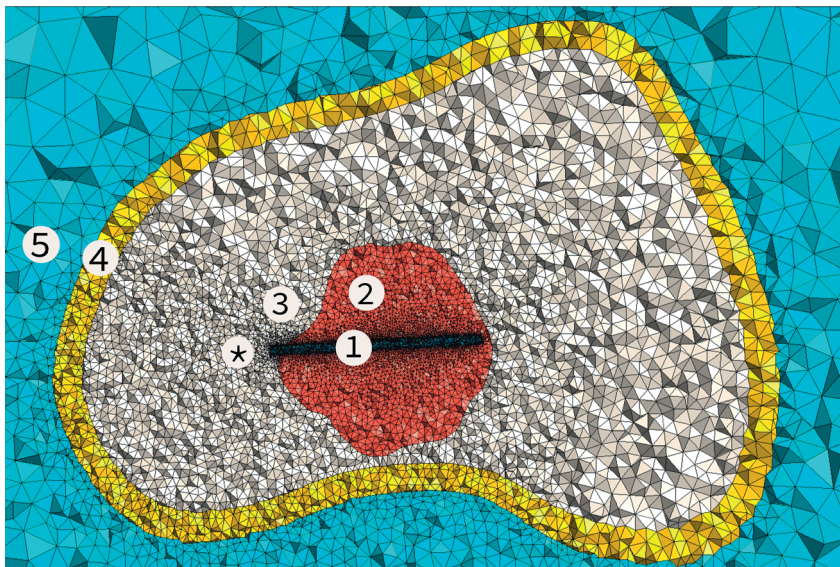
Fig. 1. *Cross sectional view of one of the cases. The numbers indicate: 1) the electrode, 2) tumor, 3) trabecular bone, 4) cortical bone, 5) muscle. Boundary conditions were applied on the surface of the electrode and the outer surface of the muscle layer. * Indicates the bottom surface of the electrode, were thermal and electrical no-flux boundary conditions were applied.*

Tissue properties

In a previous and yet to be published by our research group, optimal values tissues' properties were found by taking the average values of electrical conductivity, blood perfusion, density, specific heat, and thermal conductivity of each tissue. For the tumour and its immediate surrounding tissue, trabecular bone, a special consideration was taken, where their values were varied within the maximum and minimum ranges reported in order to find the best fitting values. Additionally, for tumour tissue (ACT), the values from healthy cartilage were taken, except for the electrical conductivity, were twice the value of the electrical conductivity of healthy cartilage was needed in order to replicate the clinical cases, which was assumed based on the fact that multiple tumorous tissues have electrical conductivities higher than twice that of their healthy counterparts [27][28][29]. With all other properties kept at their average reported values, multiple combinations of the values for tumour and trabecular bone were tested. Using a fractional factorial model to avoid a full factorial analysis, the Taguchi method, with an array with ten variables and three levels (the five tissue properties of tumour and trabecular bone with their minimum, average, and maximum values), was utilized. A simplified 2D axisymmetric FEM model was utilized for this, replicating a simplified version of an actual clinical case, until the resulting ablated zone from the simulations was within acceptable range from the clinical results. The resulting optimized parameters replicated the ablated zone in the direction along the electrode, but slightly over-estimated the results on the direction perpendicular to it. These resulting parameters were tested in another 2D axisymmetric model of a different patient with similar results. The resulting values are shown in Table 1.

Table 1 Tissue and material properties

Material / tissue	Electrical conductivity (S/m)	Blood perfusion coefficient (x10^{-3}s^{-1})	Density (kg/m3)	Specific heat (J/kg · K)	Thermal conductivity (W/m/K)
Active electrode [a]	1.00E+08	0	6450[a]	840	18
Tumor	0.4 [b]	0	1150	3664	0.487
Trabecular bone	0.05	0.167	1080	2060	0.36
Cortical bone	0.022	0.167	1908	1313	0.32
Muscle	0.446	.6167	1090	3421	0.49

All values were obtained from [30], except where indicated. [a] values as described in [31], which are of a nickel-titanium electrode, [b] assumptions for the electrical conductivity of the tumour, which are twice the value of normal healthy cartilage, also obtained from [30].

Ablation time

The radiologist who performed the RFA procedure reported the ablation time in two ways: time ≥ 60 °C and time at 90 °C. The most important duration is the time at 90 °C, which is the desired target temperature for the procedure. Since the interventional radiologist may have difficulties reaching the target temperature, and because 60 °C is seen as an important threshold for tissue damage, both of these durations were reported to highlight the time needed

to reach the target temperature and the time since thermal damage was certain to be happening. To replicate the cases, the simulated proportional-integral controller was set to 60 °C, and once reached, the target temperature was linearly increased depending on the time difference between both reported durations and the remaining 30 °C needed to reach 90 °C, after which it was finally set to 90 °C for the time indicated by the interventional radiologist as time at 90 °C.

Results

From the fifteen patient cases available, seven cases were found where the final position of the electrode was visible and the imaging data allowed for good segmentation and registration of the MR and CT images. Eight cases were excluded because the final position of the electrode was missing or because of a limited field of view or resolution that did not allow for a good image segmentation or registration. Fig. 2 shows the pre- and intra-operative images of one of the cases, indicating the tumour and electrode, whereas Fig. 3 shows the resulting image segmentation of the same case.

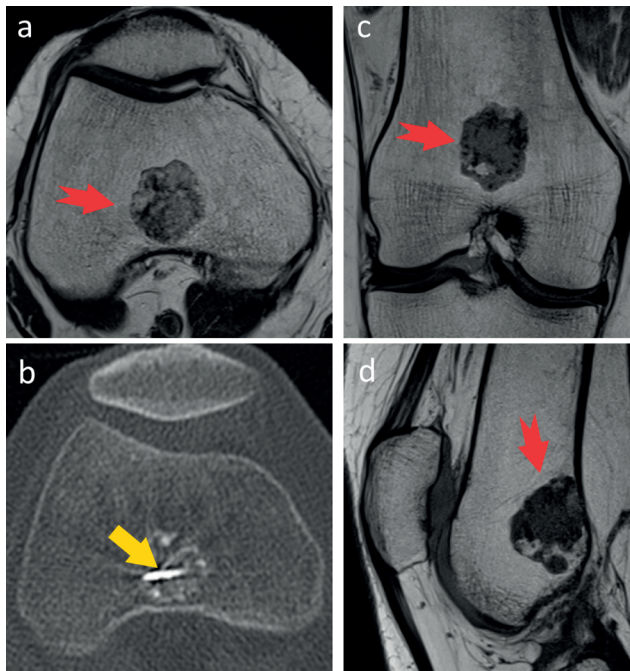**Fig. 2.** *Panels **a**, **b**, and **d** show preoperative magnetic resonance images in different planes to evaluate an atypical cartilaginous tumour located in the metaphysis of the distal femur, with the tumour being indicated by the red notched arrow. **c** shows an intraprocedural computed tomography image demonstrating the final location of the tip of the radiofrequency ablation electrode.*
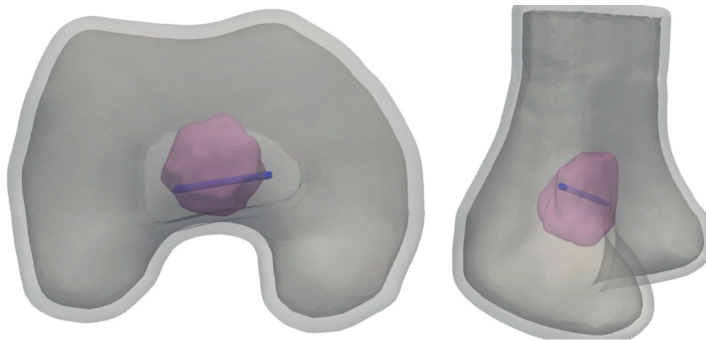
Chapter 5

Fig. 3. *Example of the resulting three-dimensional models from the image segmentations. The electrode is shown in blue, the tumour in pink, and the bones in different shades of grey. The model corresponds to the case shown in Fig. 1.*

The ablation diameter on the post-RFA images seemed to stop at the boundary with cortical bone. However, this was not observed in the computer simulations, where the ablation radius extended beyond cortical bone, as seen in Fig. 4 a,c. The reported ablation radius from the simulations was the full diameter beyond cortical bone, and this was the source of the largest discrepancies between the simulations and the radiological measurements, except for case number two, where there was an unexpectedly large ablation diameter along the electrode.
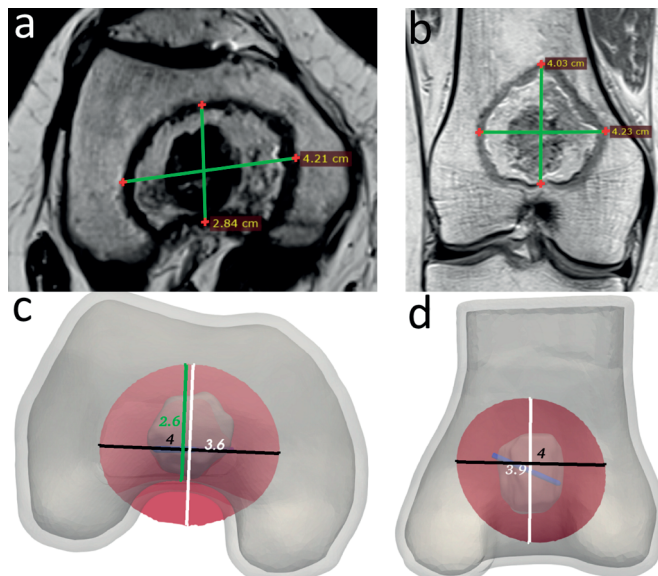
Fig. 4. a, ***b*** *Resulting ablation diameters on the magnetic resonance imaging (MRI) study performed three months after the radiofrequency ablation (same case of Figs. 2 and 3).* ***c***, ***d*** *Resulting ablation diameters from the simulations. The ablation zones are represented as a transversal cut at the height of the electrode, inside the three-dimensional geometry, to match the direction of the MRI measurements. In* ***c***, *the green line is the measurement of the ablation diameter as if it were to be taken until cortical bone, and is shown here as an example of the main difference between the results from the simulations and the radiological measurements.*

A total median error of -1 mm was achieved with interquartile ranges from -3 mm to 3 mm. The ablation diameters for the radiological images and computer models are shown in Table 2. The error, calculated as the radiological measurements minus the results from the computer models, is presented in Table 3, and shown as boxplots in Fig. 5. The computer simulations overestimated the shortest ablation diameter in most of the cases and underestimated it in the other two directions.

Table 2 Cases, length of the electrode used, timings, and the resulting ablation diameters from the radiological measurements and the simulations

Case	Electrode length (cm)	Time (min) > 60° C	Time (min) at 90° C	Ablation shortest (mm)	Ablation other (mm)	Ablation longest (mm)	Simulation shortest (mm)	Simulation other (mm)	Simulation longest (mm)
1	2	12	10	26	40	42	36	39	41
2	3	10	8	41	52	63	42	42	54
3	3	10	6	28	39	48	36	36	48
4	2	10	9	40	42	43	39	40	43
5	2	9	9	43	48	51	42	42	45
6	3	10	8	37	34	46	45	38	41
7	2	10	9	24	30	30	27	29	37

Table 3 Absolute (in mm) and relative (as percentage) errors, including the median and interquartile ranges (IQR) per measured direction, and the total error taking every measurement into account

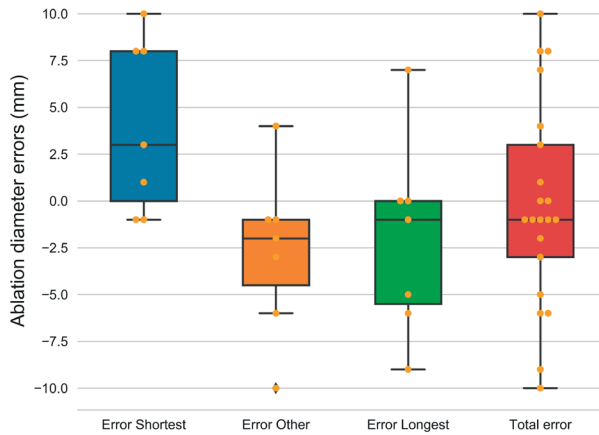| Case	Error shortest (mm) / percentage		Error other (mm) / percentage		Error longest (mm) / percentage		
1	10	138%	-1	98%	-1	98%	
2	1	102%	-10	81%	-9	86%	
3	8	129%	-3	92%	0	100%	
4	-1	98%	-2	95%	0	100%	
5	-1	98%	-6	88%	-6	88%	
6	8	122%	4	112%	-5	89%	
7	3	113%	-1	97%	7	123%	
Error interquartile ranges (IQR)							Total Error
IQR1 (mm)	0		-4.5		-5.5		-3
Median (mm)	3		-2		-1		-1
IQR3 (mm)	8		-1		0		3

Chapter 5

Fig. 5. *Boxplots of the errors of the resulting diameters for the three directions measured and the "total error" taking into account every measurement. All values are in mm.*

The effect of the more complex 3D anatomy was particularly noticeable in the early stages of the ablation procedure but less so towards the end. After the procedure had reached steady state, as shown in Figure 6a, heat concentrated close to the cortex causing damage more quickly in that direction. However, as time passed, the thermal damage became more evenly distributed, as shown in Fig. 6b.
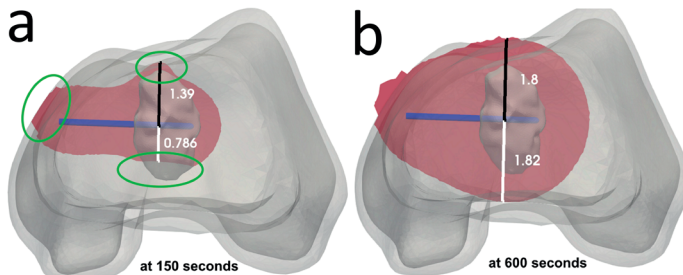
Fig. 6. *Progression of the ablation zone of case three with an atypical cartilaginous tumour in the distal femoral metaphysis at two selected times. Both ablation zones are represented as a transversal cut at the height of the electrode, inside the three-dimensional geometry. Panel **a** shows the ablation zone after 150 s, when the ablation zone is still rapidly growing. Panel **b** shows the ablation zone at the end of the procedure, after steady state has been reached. The measurements were taken from the centre of the electrode and perpendicular to it. All measurements are in cm.*

Discussion

This study demonstrated that patient-specific simulations of RFA of bone tumours could potentially be used to predict the resulting ablation zone. Although the number of patients

was relatively limited in our series, with a median error of < 3 mm in all directions measured, the tissue properties utilized in the simulations seem to be accurate enough to predict the outcomes within a reasonable range, and could potentially be used for patient planning.

The simulations tended to produce uniform ablation zones, with the largest ablation diameter in the direction of the longitudinal axis of the electrode, and with an ablation diameter that was roughly uniform in length in all perpendicular directions measured. In contrast, patient data showed more variations, which could also be due to anisotropies in bone that were not taken into account in our models. On the clinical post-RFA MRI scans, ablation zones did not seem to extend beyond bone in most cases, but our simulations did not show this effect. In fact, when the tumour was next to cortical bone, heat seemed to concentrate in that area. This effect was, however, not noticeable in the steady state of the system after several minutes had passed, where the ablation zone was more evenly distributed.

Given the slow rate at which bone heals in contrast to muscle and that the post-RFA MR images were taken approximately three months after the procedure, it is possible that the damage to muscle may not have been visible anymore. Lee et al. performed RFA in the distal healthy femurs of seven dogs, showing that MR images could be reliably used to measure the extent of the ablation zone and that the resulting ablation zones clearly extended beyond cortical bone, as shown on contrast-enhanced fat-suppressed T1-weighted images taken four to seven days after the procedure [32]. Thus, it is possible that the apparent overestimation in our simulations, with the ablation zones extending beyond the cortex, could be much more accurate than it seems. This difference was particularly remarkable in cases 1, 3, and 8, which were tumours close to a cortical wall, and which had errors of 10, 8, and 8 mm, respectively, in the "shortest direction", whereas the errors were small when the simulated ablation zone did not extend significantly beyond the cortical wall.

Another issue of our study was the relatively low resolution of the MR images. The original idea was to compare the volumes of the segmentation on post-RFA MR images to those of the simulations, but this proved to be very imprecise due to the large MR slice thickness (5 mm), making the segmentation of the ablation zone very difficult and imprecise at the boundaries, particularly because of the diffuse ring that defines it. These errors compound when taking all directions into account as in the 3D segmentations, which could result in large differences in volume. Because of this, we opted to report and compare the diameters rather than the volumes. Moreover, the ablation diameters are what radiologists usually report and clinicians use for follow-up purposes.

Another source of uncertainty came from the reported durations of the procedure, as in case number five, which stated identical durations at temperature ≥ 60 °C and at 90 °C, and thus

it was not clear what the time was to reach from 60° C to 90° C. The durations where not reported in detail, and some assumptions had to be done. Additionally, the electrode could have been moved during the intervention, and the final CT scan taken may not represent the actual final position of the electrode. Given how much both the procedural time and the position of the electrode affect the ablation zone, this may have affected the predicted size of the ablation zone. In case number two, for example, where the resulting ablation zone was considerably larger even when compared to cases with almost identical parameters (like case number 6), it seems possible that the large error in the unusually large ablation zone may be due to a repositioning of the electrode that was not registered, and thus also resulting in a large error when compared to our simulations.

There are currently no guidelines to predict the resulting ablation zone in RFA of ACT in the long bones, which are needed for accurate and safe patient planning. Our results seem to indicate that, if planned prospectively, with an accurate position of the electrode and exact duration of the procedure, computer simulations could predict the ablation diameters within a reasonable accuracy and be thus utilized for patient planning, as shown in our results, where a total median error of -1 mm was achieved. The tissue properties of the tumours have not been studied yet, but this study demonstrated that they could be reverse-engineered within reasonable accuracy for planning, and they could be made more reliable with more patient data to fit the loss function. This could allow interventional radiologists to accurately define the time, electrode length, and position required to treat ACT with RFA and make adjustments as needed to guarantee total tumour destruction while sparing as much healthy tissue as possible.

References

[1] Friedman M, Mikityansky I, Kam A et al (2004) Radiofrequency ablation of cancer. Cardiovasc Intervent Radiol 27:427-434. doi: 10.1007/s00270-004-0062-0

[2] Tins B, Cassar-Pullicino V, McCall I, et al (2006) Radiofrequency ablation of chondroblastoma using a multi-tined expandable electrode system: initial results. Eur Radiol 16:804-810. doi: 10.1007/s00330-005-0022-3

[3] Xie C, Jeys L, James S (2015) Radiofrequency ablation of chondroblastoma: long-term clinical and imaging outcomes. Eur Radiol 25:1127-1134. doi: 10.1007/s00330-014-3506-1

[4] Christie-Large M, Evans N, Davies AM et al (2008) Radiofrequency ablation of chondroblastoma: Procedure technique, clinical and MR imaging follow up of four cases. Skeletal Radiol 37: 1011-1017. doi: 10.1007/s00256-008-0526-4

[5] Petsas T, Megas P, Papathanassiou A (2007) Radiofrequency ablation of two femoral head chondroblastomas. Eur J Radiol 63:63-67. doi: 10.1016/j.ejrad.2007.03.024

[6] Lalam RK, Cribb GL, Tins BJ et al (2014) Image guided radiofrequency thermo-ablation therapy of chondroblastomas: Should it replace surgery? Skeletal Radiol 43:513-522. doi: 10.1007/s00256-014-1820-y

[7] Rehnitz C, Sprengel SD, Lehner B et al (2012) CT-guided radiofrequency ablation of osteoid osteoma and osteoblastoma: Clinical success and long-term follow up in 77 patients. Eur J Radiol 81:3426-3434. doi: 10.1016/j.ejrad.2012.04.037

[8] Wang B, Han SB, Jiang L et al (2017) Percutaneous radiofrequency ablation for spinal osteoid osteoma and osteoblastoma. Eur Spine J 26:1884-1892. doi: 10.1007/s00586-017-5080-0

[9] Arrigoni F, Barile A, Zugaro L et al (2018) CT-guided radiofrequency ablation of spinal osteoblastoma: treatment and long-term follow- up. Int J Hyperthermia 34:321-327 doi: 10.1080/02656736.2017.1334168

[10] Dierselhuis E, Overbosch J, Kwee T et al (2019) Radiofrequency ablation in the treatment of atypical cartilaginous tumours in the long bones: Lessons learned from our experience. Skeletal Radiol 48:881-887. doi: 10.1007/s00256-018-3078-2

[11] Rivas R, Overbosch J, Kwee T et al (2019) Radiofrequency ablation of atypical cartilaginous tumors in long bones: a retrospective study. Int J Hyperthermia 36:1189-1195. doi: 10.1080/02656736.2019.1687943

[12] Ruiz Santiago F, Castellano García MM, Martínez Montes JL et al (2009) Treatment of bone tumours by radiofrequency thermal ablation. Curr Rev Musculoskelet Med 2:43-50. doi: 10.1007/s12178-008-9042-3

[13] Neeman Z, Patti J, Wood B (2004) Percutaneous Radiofrequency Ablation of Chordoma. AJR Am J Roentgenol 179:1330-1332. doi: 10.2214/ajr.183.1.1830245

[14] Geuzaine C, Remacle J (2009) Gmsh: a three-dimensional finite element mesh generator with built-in pre- and post-processing facilities. INT J NUMER METH ENG 79:1309-1331. doi: 10.1002/nme.2579

[15] Cignoni P, Corsini M, Ranzuglia G (2008) MeshLab: an Open-Source 3D Mesh Processing System. In: ERCIM News. https://ercim-news.ercim.eu/en73/rd/meshlab-an-open-source-3d-mesh-processing-system. Accessed 1 August 2021.

[16] Alnaes M, Blechta J, Hake J et al (2015) The FEniCS Project Version 1.5. Archive of Numerical Software. doi: 10.11588/ans.2015.100.20553

[17] Doss J (1982) Calculations of electric fields in conductive media. Med phys 9:566-73. doi: 10.1118/1.595107

[18] Irastorza R, Trujillo M, Villagrán J et al (2014) Radiofrequency Ablation of Osteoma Osteoide: A Finite Element Study. Paper presented at the VI Latin American Congress on Biomedical Engineering CLAIB 2014, Paraná, Argentina 29, 30 & 31 October 2014. doi: 10.1007/978-3-319-13117-7_218

[19] Trujillo M, Berjano E (2013) Review of the mathematical functions used to model the temperature dependence of electrical and thermal conductivities of biological tissue in radiofrequency ablation. Int J Hyperthermia 29:590-597. doi: 10.3109/02656736.2013.807438

[20] Pennes H (1948) Analysis of tissue and arterial blood temperatures in the resting human forearm. Applied physiology 1:93-122. doi: 10.1152/jappl.1998.85.1.5

[21] Abraham J, Sparrow E (2007) A thermal-ablation bioheat model including liquid-to-vapor phase change, pressure- and necrosis-dependent perfusion, and moisture-dependent properties. Int J Heat Mass Transf 50:2537-2544. doi: 10.1016/j.ijheatmasstransfer.2006.11.045

[22] Irastorza R, Trujillo M, Villagrán J et al (2016) Computer modelling of RF ablation in cortical osteoid osteoma: Assessment of the insulating effect of the reactive zone. Int J Hyperthermia 32:221-230. doi: 0.3109/02656736.2015.1135998

[23] Haemmerich D, Wood B (2006) Hepatic radiofrequency ablation at low frequencies. Int J Hyperthermia 22:563-574. doi: 10.1080/02656730601024727

[24] Pearce J (2013) Comparative analysis of mathematical models of cell death and thermal damage processes. Int J Hyperthermia 29:262-280. doi: 10.3109/02656736.2013.786140

[25] Irastorza R, Trujillo M, Berjano E (2017) How coagulation zone size is underestimated in computer modeling of RF ablation by ignoring the cooling phase just after RF power is switched off. Int J Numer Meth Biomed Engng. doi: 10.1002/cnm.2869

[26] Laufer S, Ivorra A, Reuter V et al (2010) Electrical impedance characterization of normal and cancerous human hepatic tissue Physiol Meas 31:995-1009. doi: 10.1088/0967-3334/31/7/009

[27] Fricke H, Morse S (1926) The electric capacity of tumours of the breast. J. Cancer Res 10:340-376. doi: 10.1158/JCR.1926.340

[28] Burdette E, Seals J, Auda S et al (2016) Review of the Dielectric Properties of Animal and Human Tumors Determined from In Vivo Measurements. Crit Rev Biomed Eng 44:293-318. doi: 10.1615/CritRevBiomedEng.2017020236

[29] IT'IS Database for thermal and electromagnetic parameters of biological tissues (2019) https://itis.swiss. Accessed 09 09 2019

[30] Tungjitkusolmun S, Staelin S, Haemmerich D et al (2002) Three-dimensional finite-element analyses for radio-frequency hepatic tumor ablation. IEEE Trans Biomed Eng 49:3-9. doi: 10.1109/10.972834.

[31] Lee J, Choi S, Park H et al (2005) Radiofrequency thermal ablation in canine femur: evaluation of coagulation necrosis reproducibility and MRI-histopathologic correlation. AJR Am J Roentgenol 185:661-667. doi: 10.2214/ajr.185.3.01850661.

Chapter 6

General Discussion

With recent technological advancements, the use of minimally invasive procedures in patients with bone tumors has become more and more common, allowing the treatment of patients with minimal risks, morbidity, and complications in comparison to open surgery. Likewise, computational models for assessment and prediction in medicine are increasingly becoming part of the daily tools of caregivers, becoming essential for applications such radiotherapy planning, where computational models calculate the dosage in an area of interest to assure the quality and consistency of the treatment [1]. By combining computational models and medical imaging techniques it is possible now to build models to plan and predict what the outcome of a procedure may be, easing risks to patients and allowing for optimal treatment. This thesis's purpose was to understand the factors that influence the generation and distribution of heat in patients with bone tumors and to create computer models that could allow us to investigate these factors and to be able to accurately replicate the clinical results. With a working model, it could therefore be possible to accurately predict, modify, and plan the clinical interventions prospectively to guarantee optimal treatment.

In chapter 2, we reported the resulting ablation zones on patients treated for ACTs. Here, the attempt was to try to find factors that affected the size of the ablation zone, such as the anatomical location of the tumor, ablation time, tumor size, among others. For that, an experienced radiologist measured the post-RFA ablation zone diameters of patients that were treated for RFA of ACT. To reduce possible confounding factors, only patients that were treated with a single RFA application were included. However, it was not possible to find strong correlations between the factors analyzed and variations on the resulting ablation zones. A possible reason may be because of the few patients available, and because those patients were treated following almost identical protocols in terms of temperature and time. Nonetheless, it was clear that the ablation zones were larger than what would be expected in other tissues, such as RFA in liver, and that the variations on the protocol by the interventionalists were hard to quantify. It was clear that a more systematic and quantifiable approach was needed if the ablation zones were to be predicted.

In chapter 3, it was found in literature that multiple variations in the protocol exist RFA of bone tumors, particularly of osteoid osteoma, and particularly in terms of the ablation time and control temperature, as interventionalist try to give the best protocol possible. The question of finding the optimal protocol for RFA of bone tumors also emerged in our research group, if a tumor would be smaller or larger than usual (relative to the size of the active electrode), the idea that perhaps a longer or shorter ablation time, or a higher or lower control temperature, may be best for a given tumor had not been clearly studied. These variations in the protocol are often performed following the interventionalist's intuition and experience and not in a systematic quantifiable approach. Therefore, to quantitatively test the effects of variations on temperature and time in the resulting size of the ablation zone, we created computer models of osteoid

osteoma and systematically varied the target temperature. The models were run for a maximum of 15 minutes, which was the maximum ablation time found in literature, and the ablation zone diameters were plotted in line graphs to study and compare their behavior in time and in contrast to the various settings. With this chapter, we showed that the control temperature is far more important defining the size of the ablation zone than the ablation time and that extending the duration of the ablation time may not be enough to produce a larger ablation zone when using lower temperatures (as compared to ablation zones with higher temperatures but shorter durations). Additionally, we showed that the level of sclerosis of the tumor play an important role, especially at steady state.

In chapter 4, a finite element method model of RFA of ACT was proposed. Parameters to replicate the ablation zones from clinical data were tested, and an optimal configuration was found. To simulate the generation and propagation of heat, some thermal and electrical properties of the tissues of interest are needed. These properties are the thermal conductivity, heat capacity, density, electrical conductivity, and the blood perfusion. In the case of ACTs, none of these properties have been studied experimentally. Therefore, to study and replicate the clinical cases using the finite element method, the clinical results were used as the true size of the ablation zone to be obtained from the simulations. The properties' values were explored and optimized to minimize the difference between the ablation zones from the clinical results and from the simulations.

Given the vast amount of computationally expensive simulations needed to explore all the possible combinations of parameters to minimize the error to the clinical cases it was decided to bound the property's values based on the biological characteristics of the ACTs. Thus, the properties of healthy cartilage were used as baseline, and, since tumors tissues are known to have very high electrical conductivities, the bounds of the electrical conductivity were within what was observed for other tumorous tissues (around twice the value of healthy normal tissue). Additionally, to reduce the computational requirements and as a first step towards modelling of ACT, 2D-axysimmetric models were utilized. To avoid a full factorial analysis of each parameter, the Taguchi method was utilized, greatly reducing the number of experiments needed. In this chapter we were able to propose a model with parameters that allowed to replicate RFA of ACT using the finite element method.

In Chapter 5, the previously developed finite element models of RFA of ACT were expanded to test our assumptions using real patient anatomy. This was achieved by using image segmentation and registration techniques on CT and MR data from actual clinical cases and obtaining the actual shape and location of bones, tumor, and the final position of the electrode at the time of the procedure. These models were thus 3D models that allowed us to test the application in the complex 3D structures of the patient's anatomy. The results had a median error

of – 1 mm in the diameters of the measured ablation zones, indicating that the models could reliably simulate and predict the ablation zones and thus be used for planning the interventions. There were however important differences, as the models predicted the ablation zones to extend beyond cortical bone whereas the post-procedural images showed that the ablation zone was confined to bone only, which could be explained because the post-procedural images were taken 3 months after the intervention took place and muscle heals much faster than bone. If this were true, most of the outliers would be accounted for, and the simulations would prove to be very accurate, and thus useful for prospective planning. This tool could allow to test assumptions beforehand to find the optimal configurations such as the ablation time, position of the electrode, or target temperature, to guarantee optimal treatment.

With this thesis, a systematic approach to studying the effects of time and temperature in OO and ACT was taken, allowing for a better understanding of the interplay between two of the main parameters used in RFA. The use of the finite element method, a common and reliable method to simulate RFA [2], allowed to control for multiple of the possible confounding factors that could affect the size of the ablation zone, such as the size of the tumor, its location, the position of the electrode, accuracy of the ablation zone measurements, etc.

We showed that the tissues after the tumor are also crucial in defining the size of the ablation zone. Here, we highlight that one of the factors that makes the size of the ablation zone larger than in tissues such as liver, is the low electrical conductivity of bone surrounding the tumors. Here we emphasized the importance of this effect in the treatment of bone tumors, where soft tissue tumors with high electrical conductivity will be surrounded by bone with a much lower electrical conductivity. In the case of tumors like ACT, because of the reasons stated before, the effect may be much greater than in the case of, for example, liver tumors surrounded by liver tissue. These findings stress the importance of validating and basing assumptions on the actual tissues of interest, and highlight the difficulties of translating findings from one anatomical site to another.

Another interesting finding is that the so-called oven effect [3], which greatly affects the heat distribution of heat and that has been studied mostly in liver ablations, also plays an interesting and important role in the case of RFA of ACT and OO. When a low-perfused tissue surrounds a higher-perfused tissue, the low blood perfusion hampers heat dissipation from the area it surrounds, allowing higher temperatures for longer times in the area of interest and therefore allowing larger ablation zones. In the case of RFA in bone, it was found that during the first few 2-3 minutes, the lower thermal conductivity and blood perfusion of cortical bone concentrated heat at the tumor-cortical bone interface. However, after some time, heat became evenly distributed. As seen in chapter 1, where we studied RFA of OO, the model with a long cortical bone structure was able to reach high temperatures deeper in the direction of cortical

Chapter 6

bone due to the lack of heat sinks in the direction of cortical bone. When the ablation zone reached muscle tissue its growth was hindered due to its higher thermal conductivity and increased blood flow, acting as a heat sink. Thus, RFA of a bone tumor in a long bone may yield larger ablation zones in the direction of bone. This is an important consideration, because bone is often seen as an insulating structure, able to protect structures at risk, but given enough time, it may concentrate heat and it may cause thermal damage in unexpected ways. Similar to what happens with a cup of coffee, at first it protects from heat, but if the heat is strong enough and enough time has passed, it will be very hot to touch and it will concentrate that heat for a long time.

Furthermore, most of the simulations of RFA have been using simplified models like 2D-axisymetric models or simplified 3D models [2] with just a few using real patient anatomy [3] [4]. The simplified models have been useful to explore parameters and idealized scenarios, similar to what was explored in the first chapters of this thesis, while the ones using real patient anatomy have been developed with the intention to serve as planning systems for future interventions, as in the case of the last chapter of this thesis. The models seen in literature focused on liver, kidney, lung, or heart ablation, and now with this thesis we have developed a patient-specific model that, after more validations, could be used for patient planning of bone ablations.

Some of the main limitations of this thesis are the few data to validate the models, and that they were validated retrospectively. For the same reason, it was not possible to make any strong statistical inferences from the clinical data. Additionally, although the models are meant to be used for patient planning, they were validated retrospectively. Another limitation is that setting and running the models for the simulations can be very time consuming, because of difficulties segmenting and registering the patient data, and because of the long time required to run the simulations, making it difficult to incorporate the models into regular clinical practice. Finally, tumors and bones may have different characteristics among patients: some tumors are fleshier and bloodier whereas others are denser and even have calcifications, which could affect the results.

As a future perspective, the use of technologies such as augmented and mixed reality could be of great use to RFA guidance. By using CT and MR data, models of the patients could be created and by creating a virtual RFA applicator, we could overlap these images on a patient, and a virtual resulting ablation zone could be overlapped to guarantee that the ablation zone covers the tumor. These models would be the same as the ones used for the simulations and little extra effort would be needed to use them once the initial application is developed. Systems like this have already been developed for liver interventions [6], where they are most needed, but also where the application is harder to make work right due to the deformity of soft tissues and the

movement of the internal organs. These problems are, however, not present in the rigid bone structures, and could improve the speed and accuracy of the interventions.

Additionally, GPU-based RFA simulations [7] could work as a faster alternative to the finite element method. The use of GPUs could greatly reduce the time needed to simulate the interventions, allowing to plan and test multiple approaches in a faster and more practical way. In an ideal system, we could thus deploy an application with augmented reality, register the final position of the electrode once it has been inserted, and use the GPUs to quickly simulate the resulting ablation zone.

To conclude, RFA of bone tumors can be simulated and used for planning. RFA of ACT is effective and the size of the ablation zone is usually larger than the ablation zones seen in tissue such as liver. The effects of ablation time and control temperature were studied and how they affect the resulting ablation zone, with the target temperature perhaps as the most defining factor for the total size of the ablation zone and time for how evenly it is distributed. Although the physical properties of ACT have not been studied experimentally, these were obtained by minimizing the error from a set of possible values to target ablation zone size obtained from clinical studies. With these properties, RFA results in ACT could be calculated with sufficient accuracy and could be used for patient planning. The results from this thesis could help interventionalists to make more informed decisions regarding the interplay between target temperature and ablation time and make more informed decisions when choosing a configuration to treat a tumor. The results from this thesis are the first steps towards patient-specific planning of RFA of bone tumors and be part of the clinical pipeline once the results are better validated and the simulations optimized for better computational performance.

Chapter 6

Bibliography

[1]   F. De Martino, S. Clemente, C. Graeff, G. Palma and L. Cella, "Dose Calculation Algorithms for External Radiation Therapy: An Overview for Practitioners," Appl. Sci., vol. 11, no. 15, 2021.

[2]   E. Berjano, "Theoretical modeling for radiofrequency ablation: state-of-the-art and challenges for the future," Biomed Eng Online, vol. 5, no. 24, 2006.

[3]   Z. Liu, M. Ahmed, Y. Weinstein, M. Yi, R. Mahajan and S. Goldberg, "Characterization of the RF ablation-induced 'oven effect': the importance of background tissue thermal conductivity on tissue heating," Int J Hyperthermia, vol. 22, no. 4, pp. 327-42, 2006.

[4]   G. Zorbas and T. Samaras, "Simulation of radiofrequency ablation in real human anatomy," Int J Hypertherm, vol. 30, no. 8, pp. 570-578, 2014.

[5]   P. Voglreiter, P. Mariappan, M. Pollari, R. Flanagan, R. Blanco Sequeiros, R. Horst Portugaller, J. Fütterer, D. Schmalstieg, M. Kolesnik and M. Moche, "RFA Guardian: Comprehensive Simulation of Radiofrequency Ablation Treatment of Liver Tumors," Sci Rep, vol. 8, no. 787, 2018.

[6]   L. De Paolis and F. Ricciardi, "Augmented visualisation in the treatment of the liver tumours with radiofrequency ablation," Comput Methods Biomech Biomed Eng Imaging Vis, vol. 6, no. 4, pp. 396-404, 2018.

[7]   P. Mariappan, P. Weir, R. Flanagan, P. Voglreiter, T. Alhonnoro, M. Pollari, M. Moche, H. Busse, J. Futterer, H. Portugaller, R. Sequeiros and M. Kolesnik, "GPU-based RFA simulation for minimally invasive cancer treatment of liver tumours," Int J Comput Assist Radiol Surg., vol. 12, no. 1, pp. 59-68, 2017.

Chapter 7
Summary & Samenvatting

Summary

Surgical resection has been the standard treatment of choice for most solid tumors, yet it can be painful and debilitating, with high associated risks, particularly in patients that already have coexisting comorbidities.

Radiofrequency ablation (RFA) is a minimally invasive technique that has become increasingly popular for the treatment of solid tumors, and which is used for palliative and curative care. In RFA, a small electrode is placed into the patient, which then induces heat in the target area, increasing the temperature of the surrounding tissues with the objective to induce coagulation necrosis in the whole tumor. It is commonly used for the treatment of liver, kidney, and lung tumors, and for the small benign bone tumors called osteoid osteoma. Minimally invasive procedures such as RFA can be a great alternative for patients that are not surgical candidates and in cases where a more aggressive form of treatment does not seem to outweigh the benefits for the patient. RFA has high success rates and low complication rates, requiring little to no patient hospitalization. Because of this, it has great potential to become the standard of care for tumors such as ACT.

However, there is little experience on the treatment of bone tumors with RFA, making it hard to predict the outcomes of the technique for large bone tumors such as ACTs, one of the most common type of tumor encountered in orthopaedic oncology. Clinical experience is often based on the treatment of small (<2 cm) and heavily calcified tumors such as osteoid osteomas, or on the ablation of other tissues such as the liver. Thus, doctors have to rely on rough estimations, which may result in unnecessary damage to healthy structures or in tumors that are not destroyed completely.

To solve this problem, computational methods simulating RFA in bone tumors could help doctors plan their procedures in a safe and effective way. The objective of this thesis is to understand better how is heat generated and propagated in RFA of bone tumors. The findings from this thesis could increase the interventional radiologist's understanding of RFA of bone tumors, allowing them to make better informed decisions. Additionally, by using clinical data and computational models, patient-specific planning could be done on a per-case basis, which could potentially increase the safety and effectiveness of the treatment.

In **chapter 2**, a retrospective study to determine the size of the ablation zone on patients treated with radiofrequency ablation of ACTs was performed. To reduce variability, only patients that had undergone a single-session single-application CT-guided temperature-controlled RFA, and which had received a follow-up MRI scan 3 months after the procedure, were included. The ablation zones were measured on the post-operative MRI images, and this chapter demon-

strated that ablation zones in bone could be larger than what would be expected from other tissues, such as the ex-vivo liver recommendations given by the RFA manufactures. The results highlight the need for more data or models that could help interventional radiologist's plan the procedures, as the current information is not enough to accurately plan the procedures.

In **Chapter 3**, an initial computational model built upon existing literature models for radio-frequency ablation of osteoid osteomas was created to study the effects of control temperature, ablation time, and the different tissues surrounding the tumor. The model used the finite element method to simulate the generation and propagation of heat, and a cell death model to study the damage caused to the tissues over time. Three different anatomical configurations were considered and multiple control temperatures were chosen to study their effects on the ablation zone. Here it was demonstrated that the ablation zone's size has a clear dependency not only in the properties of the tumors but also on the background tissues surrounding them. In particular, the sharp difference on electrical conductivity between soft tissue (tumor) and bony tissue seemed to have large influence on the results.

In **Chapter 4**, computational models for ACTs were created and tested in 2D as an initial proof of principle with the aim to replicate selected clinical cases. The main purpose of this chapter was to find the right tissue parameters to fit the model to the measured clinical outcomes. However, the models have multiple parameters with multiple possible values, and doing a full factorial analysis is not a viable option. Key values were selected and a fractional factorial analysis was used to evaluate the effects of the parameters on the outcome with a much lower number of experiments and the most appropriate set of properties was selected to fit the models to the measured outcomes. Once the optimal parameters were found, the model was able to accurately replicate with the measured results seen in the post-operative images.

Chapter 5 used the previously obtained optimized parameters and tested their accuracy on a larger dataset and using patient-specific 3D models. The models showed that the previously obtained assumptions can predict the ablation diameters with acceptable accuracy and could thus potentially be utilized for patient planning. It also highlighted the importance of studying the heat generation and propagation in 3D, particularly in cases of complex 3D anatomical structures with large differences in tissue properties. The models presented in this chapter could allow interventional radiologist to plan procedures with much more accuracy, selecting the right electrode length, its position, and the amount of time needed to guarantee total tumor destruction while sparing as much healthy tissues as possible.

Chapter 6, presents a more extensive discussion of the major findings of this thesis. The results are put into context and recommendation for the future are also given. A systematic approach to study the effects of the various tissues, their interplay, and how they are affected by the

different ablation times and control temperatures utilized, could lead to a better understanding of RFA and lead to better informed decisions by interventional radiologists. The thesis also showed how crucial the electrical conductivity was for the predicting the ablation zone, not only the one from the target tissue but also the one from the surrounding tissues, which is contrasted even more in the case of bone tumors than in other anatomical areas with more homogeneity on their tissue properties. Blood perfusion, which is a crucial factor for ablations in other anatomical areas, does not seem to play such an important factor in the case of bone tumors, as the tumors and surrounding bony structures possess little vascularity and there are no large blood vessels acting as heat sinks. Although the actual tissue properties of the cartilaginous tumors studied here are not known, it is possible to estimate their values by fitting the models to the clinical outcomes. The models generated by the simulations could be incorporated into planning and guidance tools, by generating 3D images of the simulations and super-imposing them onto DICOM images or other tools such as virtual reality glasses, and be thus fully integrated into the clinical workflow for safe and effective tumor planning.

Chapter 7

Samenvatting

Chirurgische resectie is de standaardbehandeling voor de meeste solide tumoren, maar het kan pijnlijk en slopend zijn, met hoge bijbehorende risico's, vooral bij patiënten die al comorbiditeiten hebben.

Radiofrequente ablatie (RFA) is een minimaal invasieve techniek die steeds populairder is geworden voor de behandeling van solide tumoren en die wordt gebruikt voor palliatieve en curatieve zorg. Bij RFA wordt een kleine elektrode in de patiënt geplaatst, die vervolgens warmte in het doelgebied induceert, waardoor de temperatuur van de omliggende weefsels wordt verhoogd met als doel coagulatienecrose in de hele tumor te induceren. Het wordt vaak gebruikt voor de behandeling van lever-, nier- en longtumoren en voor de kleine goedaardige bottumoren die osteoïd osteomen worden genoemd. Minimaal invasieve procedures zoals RFA kunnen een geweldig alternatief zijn voor patiënten waarbij chirurgie geen optie is en in gevallen waarin een agressievere vorm van behandeling niet opweegt tegen de voordelen voor de patiënt. RFA heeft hoge slagingspercentages en lage complicaties, waardoor er weinig tot geen ziekenhuisopname nodig is. Hierdoor heeft het een groot potentieel om de standaardbehandeling te worden voor tumoren zoals ACT.

Er is echter weinig ervaring met de behandeling van bottumoren met RFA, waardoor het moeilijk is om de resultaten van de techniek te voorspellen voor grote bottumoren zoals ACT's, een van de meest voorkomende soorten tumoren die in de orthopedische oncologie worden aangetroffen. Klinische ervaring is vaak gebaseerd op de behandeling van kleine (<2 cm) en zwaar verkalkte tumoren zoals osteoïd osteomen of op de ablatie van andere weefsels zoals de lever. Artsen zijn dus afhankelijk van ruwe schattingen, wat kan leiden tot onnodige schade aan gezonde structuren of tot tumoren die niet volledig worden vernietigd.

Om dit probleem op te lossen zouden rekenkundige methoden die RFA van bottumoren simuleren artsen kunnen helpen bij het plannen van hun procedures op een veilige en effectieve manier. Het doel van dit proefschrift is om beter te begrijpen hoe warmte wordt gegenereerd en gepropageerd in RFA van bottumoren. De bevindingen van dit proefschrift zouden het begrip van de interventieradioloog van RFA voor bottumoren kunnen vergroten, waardoor ze beter geïnformeerde beslissingen kunnen nemen. Bovendien zou door het gebruik van klinische gegevens en computermodellen patiënt specifieke planning kunnen worden gemaakt, wat de veiligheid en effectiviteit van de behandeling mogelijk zou kunnen vergroten.

In **hoofdstuk 2** werd een retrospectieve studie uitgevoerd om de grootte van de ablatiezone te bepalen bij patiënten die werden behandeld met radiofrequente ablatie van ACTs. Om de variabiliteit te verminderen, werden alleen patiënten geïncludeerd die een single-sessie single-

application CT-geleide temperatuur-gecontroleerde RFA hadden ondergaan en die 3 maanden na de procedure een follow-up MRI-scan hadden gekregen. De ablatiezones werden gemeten op de postoperatieve MRI-beelden en dit hoofdstuk toonde aan dat de ablatiezones in bot groter zouden kunnen zijn dan wat zou worden verwacht van andere weefsels, zoals de ex-vivo leveraanbevelingen gegeven door de RFA-fabrikanten. De resultaten benadrukken de behoefte aan meer gegevens of modellen die interventieradiologen kunnen helpen bij het plannen van de procedures, aangezien de huidige informatie niet voldoende is om de procedures nauwkeurig te plannen.

In **Hoofdstuk 3** werd een initieel computermodel, gebaseerd op bestaande literatuurmodellen voor radiofrequente ablatie van osteoïde osteomen, gecreëerd om de effecten van controle-temperatuur, ablatietijd en de verschillende weefsels rond de tumor te bestuderen. Het model gebruikte de eindige-elementenmethode om de opwekking en verspreiding van warmte te simuleren en een model om de schade aan de weefsels in de loop van de tijd te bestuderen. Er werden drie verschillende anatomische configuraties overwogen en er werden meerdere controletemperaturen gekozen om hun effecten op de ablatiezone te bestuderen. Hier werd aangetoond dat de grootte van de ablatiezone een duidelijke afhankelijkheid heeft, niet alleen van de eigenschappen van de tumoren, maar ook van de achtergrondweefsels eromheen. Vooral het scherpe verschil in elektrische geleidbaarheid tussen zacht weefsel (tumor) en botweefsel leek grote invloed te hebben op de resultaten.

In **Hoofdstuk 4** werden rekenkundige modellen voor ACTs gecreëerd en getest in 2D als pilot met als doel geselecteerde klinische gevallen te repliceren. Het belangrijkste doel van dit hoofdstuk was om de juiste weefselparameters te vinden om het model aan te passen aan de gemeten klinische resultaten. De modellen hebben echter meerdere parameters met meerdere mogelijke waarden, en het uitvoeren van een volledige factoriële analyse is geen haalbare optie. Er werden sleutelwaarden geselecteerd en een fractionele factoriële analyse werd gebruikt om de effecten van de parameters op de uitkomst te evalueren met een veel lager aantal experimenten en de meest geschikte set eigenschappen werd geselecteerd om de modellen aan te passen aan de gemeten resultaten. Nadat de optimale parameters waren gevonden, kon het model nauwkeurig worden gerepliceerd met de gemeten resultaten die postoperatief werden waargenomen.

Hoofdstuk 5 gebruikte de eerder verkregen geoptimaliseerde parameters en testte hun nauwkeurigheid op een grotere dataset en met behulp van patiënt-specifieke 3D-modellen. De modellen toonden aan dat de eerder verkregen veronderstellingen de ablatiediameters met acceptabele nauwkeurigheid kunnen voorspellen en dus mogelijk kunnen worden gebruikt voor de planning van de patiënt. Het benadrukte ook het belang van het bestuderen van de warmteontwikkeling en -voortplanting in 3D, met name in het geval van complexe 3D-anatomische structuren met grote verschillen in weefseleigenschappen. De modellen die in dit hoofdstuk

worden gepresenteerd, zouden de interventieradioloog in staat kunnen stellen procedures veel nauwkeuriger te plannen, te helpen bij het selecteren van de juiste elektrodelengte, de positie en de hoeveelheid tijd die nodig is om totale tumorvernietiging te garanderen terwijl zoveel mogelijk gezond weefsel wordt gespaard.

Hoofdstuk 6 presenteert een meer uitgebreide bespreking van de belangrijkste bevindingen van dit proefschrift. De resultaten worden in context geplaatst en er worden ook aanbevelingen voor de toekomst gegeven. Een systematische benadering om de effecten van de verschillende weefsels, hun wisselwerking en hoe ze worden beïnvloed door de verschillende gebruikte ablatie tijden en temperaturen te bestuderen, zou kunnen leiden tot een beter begrip van RFA en leiden tot beter geïnformeerde beslissingen door interventieradiologen. Het proefschrift toonde ook aan hoe cruciaal sommige parameters zijn die de ablatiezone beïnvloeden, zoals de elektrische geleidbaarheid van zowel het doelweefsel als het omringende weefsel, dat bij bottumoren nog sterker contrasteert dan in andere anatomische gebieden met meer homogeniteit op hun weefseleigenschappen. De modellen die door de simulaties worden gegenereerd, kunnen worden opgenomen in plannings- en begeleidingstools, door 3D-beelden van de simulaties te genereren en deze op DICOM-beelden of andere tools zoals virtual reality-brillen te superponeren, en zo volledig te worden geïntegreerd in de klinische workflow voor een veilige en effectieve tumorplanning.

Chapter 8
Acknowledgments

I would like to thank all friends, family, and colleagues that helped me, challenged me, and encouraged me along this sometimes difficult but always exciting challenge. In particular, I would like to dedicate some special words to the ones closer to me along this journey.

First, my first promotor, Dr. Ir. Peter van Ooijen. You met me during my master's studies and trusted me as a student and researcher to continue and do PhD with you. I always loved the freedom and trust you gave me, always allowing me to explore any ideas and projects I may have while trying to keep me in check and have a good action plan. Along the way I faced many challenges, I am very grateful for all the intellectual and emotional support.

My second promotor, Prof. Paul Jutte. I always admired your interest for exploring new techniques and modalities in your clinical practice, which allowed me to explore and trying a bunch of different projects and ideas which made doing research very fun but also grounded to actual clinical problems. Thank you for this opportunity.

My third promotor, Dr. Thomas Kwee. We didn't start working together until a bit later in my PhD and we didn't have as many chances to bond, yet you were always very kind and open. I am always surprised by how quick, detailed and helpful your feedback is. Thank you for all the support.

Dr. Ludo Cornelissen, you arrived when I was feeling the most lost with my project and really helped me get out of my head and crystalize my ideas. You were a great friend and mentor, always with a wide smile and a clear mind.

Thanks to Jelle and Charlote, who always welcomed me in the CT room and always were open to discussions to help me understand better the clinical workflow and needs.

Daan, my brother from another mother, and the main person to blame if I ever have liver problems. Thank you so much for all the fun and your great friendship.

A Carlos, compañero de eternas discusiones, ya sea que hablemos de penas o glorias, siempre has estado ahí para mí. Gracias por esta amistad tan grande. Gracias también a Esmee, que no sé cómo aguanta nuestras platicas.

To Ruben, yours was the first thesis project I proposed and supervised. It was very exciting and challenging, but above all, it was a pleasure to work with you. Thank you for your help and all these years of friendship.

Chapter 8

Thank you to the all my colleagues from DASH, G2, Bloemsingel, and Radiotherapy and Radiology. Yeshu, Bingjan, Sunyi, Yiapan, Xueping, Herbert, Alessia, Ivan, Rik, Mirjam, Daiwei, Stella, Runlei, Congying, Moniek, Marly, Gert-jan, Aniek, Daan, Randy, Xiaonan, Qiao, Yihui, Griigory, Nikos, Erfan, Jiali, Mineke. It was great working with you, and beyond that, it was great being your friends. From my random hugs (which luckily Xueping always enthusiastically reciprocated) to helping each other move out or have a nice hot-pot session, our friendship was way beyond the lab and I am happy to have worked with you and call you my friends.

To the 3D Lab, Joep, Nick, Anne, Bram, Haye, Peter, Lissane, Hylke, Klijs, Jelbrich, Max. We spent endless times discussing endless different projects, helping each other, and I learned a lot from all of you. And of course, having some drinks and snacks at the buurvrouw or Dot is something that we should do again!

Thank you to all my friends and family in The Netherlands and in Mexico, and all around the world, who have made this journey into a wonderful adventure. Margot, Laurens, Emilio, Geerte, Fernand, Marloes. Sandy, Justus, Viviana, Pedro. Chuy, Nets, Cesar, Melo, Paul, Carlos, Diego, Ulises, Ata. Adro, Serna, Akoryou, Zombie, Cless, Chrono, Abel. David, Ivan, Luz, Lumina. Silvia, Peter, Irina, Adrian, Jaap, Makram, Sreejita, Milou, Larise, Sebastian.

Y por su puesto a mis padres, Ricardo Rivas Urias y Silvia Loya Apodaca, que siempre me han apoyado en todas mis decisiones y no hubiera podido lograr nada de esto sin ustedes. A cada paso que doy, sé que siempre puedo contar con ustedes. Gracias por ser el viento bajo mis alas. Y gracias también a mi hermanita Marian, que hasta con la portada de la tesis me ayudó. Los amo.

Chapter 9
Author Affiliations
(Alphabetical order)

Ludo Cornelissen, PhD
University of Groningen, University Medical Center Groningen, Department of Radiotherapy, Groningen, The Netherlands

Rudi A J O Dierckx, MD PhD
University of Groningen, University Medical Center Groningen, Department of Nuclear Medicine and Molecular Imaging, Groningen, The Netherlands

Ruben Hijlkema, MSc
University of Groningen, Faculty of Mathematics and Natural Sciences, University of Groningen, Groningen, The Netherlands

Paul C Jutte, MD PhD
University of Groningen, University Medical Center Groningen, Department of Orthopedics, Groningen, The Netherlands

Thomas C Kwee, MD PhD
University of Groningen, University Medical Center Groningen, Department of Radiology, Groningen, The Netherlands

Peter M A van Ooijen, PhD
University of Groningen, University Medical Center Groningen, Department of Radiotherapy, Groningen, The Netherlands

Jelle Overbosch, MD
University of Groningen, University Medical Center Groningen, Department of Radiology, Groningen, The Netherlands

Ricardo Rivas Loya, MSc
University of Groningen, University Medical Center Groningen, Department of Radiotherapy, Groningen, The Netherlands

Chapter 9

Chapter 10
List of publications

Publications in peer reviewed journals

2022

Computer 3D modeling of radiofrequency ablation of atypical cartilaginous tumours in long bones using finite element methods and real patient anatomy

Rivas Loya, R., Jutte, P. C., Kwee, T. C. & van Ooijen, P. M. A., 28-Apr-2022, In: European Radiology Experimental. 6, 1, 11 p., 21.

2021

Effects of control temperature, ablation time, and background tissue in radiofrequency ablation of osteoid osteoma: A computer modeling study

Rivas, R., Hijlkema, R. B., Cornelissen, L. J., Kwee, T. C., Jutte, P. C. & van Ooijen, P. M. A., Sep-2021, In: International journal for numerical methods in biomedical engineering. 37, 9, p. e3512 14 p., e3512.

2019

Radiofrequency ablation of atypical cartilaginous tumors in long bones: a retrospective study

Rivas, R., Overbosch, J., Kwee, T., Kraeima, J., Dierckx, R. A. J. O., Jutte, P. C. & van Ooijen, P. M., 1-Jan-2019, In: International journal of hyperthermia. 36, 1, p. 1189-1195 7 p.

Chapter 11

Curriculum vitae

Ricardo Rivas Loya was born in Chihuahua, Mexico, on June 26th, 1991. He studied Electrical Engineering at the Instituto Tecnológico de Chihuahua (Chihuahua Institute of Technology) and graduated with honors in 2013. He then moved to the Netherlands in 2014 to study a master's degree in Biomedical Engineering, graduating with his thesis "3D models of the lower legs' bone and vascularity from standard and dynamic CTA". Ricardo did his master's thesis at the 3D Lab in Groningen, where he met who would become his main PhD thesis supervisor, Dr. Peter van Ooijen.

With a growing interest in Medical Imaging and Computational Models, he worked under the supervision of Dr. Peter van Ooijen, Prof. Paul Jutte, and Dr. Thomas Kwee at the University Medical Center Groningen, where he explored ways to better understand and predict the outcomes of radiofrequency ablation of bone tumors by using the finite element method.

After his PhD, Ricardo found a position in Philips Medical Systems, in Best, The Netherlands, as Clinical Scientist in the Systems team for CT.

In his free time, Ricardo enjoys listening to and playing music, reading, and doing any kind of sports like bouldering and football.

Chapter 11

Curriculum vitae (Dutch version)

Ricardo Rivas Loya is geboren in Chihuahua, Mexico, op 26 juni 1991. Hij studeerde elektrotechniek aan het Instituto Tecnológico de Chihuahua (Chihuahua Institute of Technology) en studeerde cum laude af in 2013. Daarna verhuisde hij in 2014 naar Nederland om een Master's degree in Biomedical Engineering te doen. Hij studeerde af met zijn proefschrift "3D-modellen van het bot en de vasculariteit van de onderbenen van standaard en dynamische CTA". Ricardo deed zijn masterscriptie aan de 3D Lab in Groningen, waar hij dr. Peter van Ooijen ontmoette die zijn belangrijkste scriptiebegeleider zou worden.

Met een groeiende interesse in Medical Imaging en Computational Models werkte hij onder supervisie van Dr. Peter van Ooijen, Prof. Paul Jutte en Dr. Thomas Kwee aan het Universitair Medisch Centrum Groningen, waar hij manieren verkende om de uitkomsten van radiofrequente ablatie van bottumoren met behulp van de eindige elementenmethode te voorspellen.

Na zijn promotie vond Ricardo een functie bij Philips Medical Systems, in Best, Nederland, als klinisch wetenschapper in het Systems-team voor CT.

In zijn vrije tijd luistert en speelt Ricardo graag muziek, leest hij en doet hij graag sporten zoals boulderen en voetbal.